MECHANICS-BASED INVESTIGATION INTO THE STRUCTURAL INTEGRITY AND OPTIMIZATION OF CORE-SHELL NANOSTRUCTURED ELECTRODE MATERIALS FOR LITHIUM ION BATTERIES

LI WEIQUN

Ph.D

The Hong Kong Polytechnic University

2017

The Hong Kong Polytechnic University

Department of Mechanical Engineering

Mechanics-based Investigation into the Structural Integrity and Optimization of Core-shell Nanostructured Electrode Materials for Lithium Ion Batteries

LI Weiqun

A thesis submitted in partial fulfilment of the requirements for the degree of Doctor of Philosophy

August 2016

CERTIFICATE OF ORIGINALITY

I hereby declare that this thesis is my own work and that, to the best of my knowledge and belief, it reproduces no material previously published or written, nor material that has been accepted for the award of any other degree or diploma, except where due acknowledgement has been made in the text.

_________________________ (Signed)

_________LI WEIQUN_______ (Name of student)

Lovingly dedicated to my parents and grandma

Abstract

Lithium ion battery is an efficient energy storage and conversion device in our daily life and industry production. Several problems still limit its wider application, such as the low reversible capacity, short cycle life, slow charging rate, safety issues, etc. In order to solve these problems, the high-capacity anode materials, such as tin dioxide (SnO_2, 781 mA h g^{-1}) and silicon (Si, 4200 mA h g^{-1}), have been studied. However, SnO_2 and Si anode materials suffer from large volume change during electrochemical cycling, leading to fracture and pulverization of the anode materials and degradation and failure of the lithium ion batteries. Therefore, carbon coating technique has been used to constrain the volume change and alleviate the fracture. The structural integrity is guaranteed at the expense of overall capacity due to the lower theoretical capacity of carbon (372 mA h g^{-1}). This thesis is focused on the structural integrity and the capacity maximization of the core-shell nanostructured anode materials with either carbon or Si as the coating materials. Chapters 1-3 discussed the research background, literature reviews and research methods related to materials and mechanics for lithium ion batteries. From chapter 4 to 7, four kinds of core-shell nanostructured electrode materials were studied by experimental and/or theoretical approaches. Finally, conclusions, discussions and future works were presented in Chapter 8.

In Chapter 4, the carbon-coated SnO_2 nanowire anode material was studied by using theoretical methods. The fracture of the carbon shell was found to be

thickness-dependent during lithiation. If the thickness is lower than a critical value of ~9 nm, the carbon shell is prone to being cracked. A theoretical model, based on the theory of diffusion, was established to calculate the concentration of lithium ions in the nanowire during lithiation. By analogously treating the lithiation-induced expansion as thermal expansion, the evolution of stress and deformation upon lithiation was analyzed by using finite element simulation. An optimal thickness (~9 nm) of carbon shell was obtained so that the structural integrity and maximum capacity can be achieved for the carbon-coated SnO_2 nanowire electrode materials.

In order to further improve the capacity of the anode material, the carbon-coated Si nanoparticle electrode was studied in Chapter 5. The carbon shell was found to expedite the fracture of the synthesized carbon-coated Si nanoparticles during lithiation. The fracture occurrence was summarized to be dependent on the geometrical dimensions, including the thickness of carbon shell and the diameter of Si core. The finite element simulation results showed that the carbon shell is firstly cracked due to the lithiation-induced expansion of Si core. Such crack propagates into the lithiated Si core upon further lithiation due to the elevated energy release rate near the tip of crack caused by the material's inhomogeneity along the direction of crack extension. An optimal design guideline was thereby proposed to prevent the fracture and maximize the capacity for the carbon-coated Si nanoparticle electrode materials.

To further improve the stability and capacity of the Si-based anode materials, the yolk-shell carbon-coated Si nanoparticles, which contain a void space between the yolk and shell, were studied through *in situ* lithiation and theoretical modeling, as discussed in Chapter 6. The geometrical dimension-dependent fracture of the nanoparticles was revealed from the experimental studies. A mechanics-based theoretical model was proposed to calculate the stress states in the carbon shell upon full lithiation. A design guideline was provided to maintain the structural integrity and maximize the capacity by optimizing the geometrical dimensions of the yolk-shell carbon-coated Si nanoparticles.

Apart from voiding the fracture, interfacial stability between electrodes and cooper (Cu) current collector is also important for improving the performance of the Si-based electrode materials. In Chapter 7, the Si-coated Cu nanowires were synthesized though hydrothermal method and magnetron sputtering technique. The lithium nanostructures formed on the surface of Si shell during delithiation. The bulk lithium nanostructures reacted with the delithiated Si shell to form Li_xSi, inducing the fracture of the Si shell. However, the Si shell adhered well with the Cu core, indicating a stable cycling performance. These results showed the potential application of the Si-coated Cu nanowire structured anode materials for lithium ion batteries.

Through the comprehensive studies of the core-shell nanostructured electrode materials, the lithiation/delithiation and fracture mechanisms of the high-capacity core-shell nanostructured electrode materials were analyzed. The experimental and theoretical approaches should be beneficial for the study of other electrode materials. The optimal design guidelines proposed in this thesis

should be of great value for the design of the core-shell structured electrode materials with supreme structural integrity and high capacity for lithium ion batteries.

Publications

[1] W. Li[†], Q. Wang[†], K. Cao, J. Tang, H. Wang, L. Zhou, H. Yao, Mechanics-based optimization of yolk-shell carbon-coated silicon nanoparticle as electrode materials for high-capacity lithium ion battery, *Composites Communications* 1 (2016) 1-5. ([†]Co-first authors)

[2] W. Li, K. Cao, H. Wang, J. Liu, L. Zhou, H. Yao, Carbon coating may expedite the fracture of carbon-coated silicon core-shell nanoparticles during lithiation, *Nanoscale* 8 (2016) 5254–5259.

[3] Q. Li[†], W. Li[†], Q. Feng, P. Wang, M. Mao, J. Liu, L. Zhou, H. Wang, H. Yao, Thickness-dependent fracture of amorphous carbon coating on SnO_2 nanowire electrodes, *Carbon* 80 (2014) 793-798. ([†]Co-first authors)

[4] W. Li, X. Liu, Y. Lu, and H. Yao, Microscopic pillars and tubes fabricated by using fish dentine as a molding template. *International Journal of Molecular Sciences* 15 (2014) 14909-14920.

Conference presentations

[1] W. Li, H. Wang, L. Zhou, H. Yao, Mechanics-based investigation into the structural integrity of core-shell nanostructured electrodes for lithium ion batteries. Best Poster Award and oral presentation at the *5th International*

Symposium on Energy Challenges & Mechanics (ISECM) – working on small scales, 10-14 July 2016, Inverness, Scotland, United Kingdom.

[2] W. Li, Q. Wang, K. Cao, H. Wang, L. Zhou, H. Yao, Mechanics-based investigation into the stability of Si@C and Si@void@C nanoparticle electrodes during lithiation. Oral presentation at the *International Symposium on Advanced Materials and Structures (ISAMS)*, 2-4 January 2016, Hong Kong.

[3] W. Li, K. Cao, Z.-L. Xu, H. Wang, J. Liu, J.-K. Kim, L. Zhou, H. Yao, Carbon coating facilitates the fracture of Si@C core-shell nanoparticles during lithiation. Poster presentation at the *Gordon Research Conference (GRC) on Nano-Mechanical Interfaces*, 19-24 July 2015, Hong Kong.

[4] W. Li, L. Zhou, H. Yao, Thickness-dependent fracture of amorphous carbon coating on SnO_2 nanowire electrodes. Best Student Presentation Award at the *19th Annual Conference of HKSTAM in conjunction with the 11th Jiangsu-HK Forum on Mechanics and Its Application*, 28 March 2015, Hong Kong.

[5] W. Li, X. Liu, Y. Lu, H. Yao, Microscopic pillars and tubes fabricated by using fish dentine as a molding template. Poster Prize at the *5th Unilever-RSC International Symposium on Functional Materials Science*, 15 September 2014, Hong Kong.

[6] Q. Li, W. Li, Q. Feng, P. Wang, M. Mao, J. Liu, L. Zhou, H. Wang, H. Yao, Thickness-dependent fracture of amorphous carbon coating on SnO_2 nanowire electrode. Oral presentation at the *2nd International Congress on Materials and Renewable Energy (MRE 2014) in conjunction with Nanomaterials Symposia*, 8-10 August 2014, Hong Kong.

[7] W. Li, H. Yao, L. Zhou, Bio-inspired fabrication of microscopic pillars and tubes by using dentin of black carp teeth as template. Poster presentation at *Gordon Research Conference (GRC) on Nano-Mechanical Interfaces*, 4-9 August 2013, Hong Hong.

Acknowledgements

It is always hard to start this part since words cannot fully express my appreciation to all the people who guided and helped me during my study for pursuing the PhD degree. The deepest respect and gratitude go to my chief supervisor, Dr. Haimin Yao, who provided me the opportunity to study as a research student in his group at PolyU. In addition to the knowledge in mechanics and material science and the problem-solving capability, he imparted me the research methods and working principles that will be a lighthouse indicating the future direction of my work and life. His enthusiasm, creativity and diligence motivated me in our every research project. I also appreciate the chances he provided me to wrap up our research results and present them in the international conferences, which dramatically improved my logic thinking and presentation skills. Besides, his positive life attitude and wise philosophy of life benefited me through all these years.

I would like to express my most sincere appreciation to my co-supervisor, Prof. Limin Zhou, who always inspired me with full of fantastic ideas and instructed me about the experimental approaches with his patient guidance and rich experience. His invaluable suggestions and enlightenment benefited me a lot and encouraged me to overcome the issues in our research. It is his rigorous and generous attitude that will be a precious fortune for my future work and life.

It was an unforgettable and invaluable experience to collaborate with Prof. Hongtao Wang and Prof. Jiabin Liu at Zhejiang University. I learned a lot from them, including but not limited to the experimental techniques, the rigorous working habit and the inspiring mind. It was also nice to work with Dr. Qianqian Li and Mr. Ke Cao, who are experienced researchers and provided me with uncountable help in our *in situ* characterizations of the electrode materials.

I would like to thank my colleagues, Mr. Qian Wang and Dr. Jingjing Tang. We worked together to accomplish the researches on the yolk-shell carbon-coated silicon nanoparticle electrode materials. I also got constructive advices from them on materials synthesis and characterization. I appreciate the helpful discussion with Dr. Zheng-Long Xu and Prof. Jang-Kyo Kim at the Hong Kong University of Science and Technology on the lithiation-induced fracture of the carbon-coated silicon nanoparticle electrode materials. Special thanks go to Dr. Xiaowei Liu and Dr. Yang Lu at City University of Hong Kong, without whom I cannot finish the research on the pickup and characterization of the bio-inspired microfiber and -tubes.

It is always nice to be working with my colleagues in the Bio-inspired Mechanics and Materials Group, including Dr. Chong He, Dr. Chenguang Zeng, Dr. Zhaoqian Xie, Mr. Jimin Fu, Dr. Long Li, Mr. Kei Saito, Mr. Qifang Yin, Mr. Zhenbin Guo, Prof. Shuiliang Chen, Mr. Yan Zhou, Mr. Zhaoqiang Song, Ms. Zixin Ma, Ms. Yanwei Xue, Mr. Hua Zhang, Mr. Juntan Yang and Ms. Yang Gao. I also enjoyed the discussions with Dr. Yuming Chen, Dr. Xiaoyan Li and Ms. Jing Hu and thank for their help whenever problem occurred with my experiments. I appreciate every brainstorm and leisure time with these intelligent and funny friends and every single help and enlightenment from them.

It was an unforgettable memory of playing and hanging out with them, which enriched my study and life at PolyU.

A lot of appreciation goes to the technical staff, such as Dr. Hardy Lui, Dr. Wei Lu, Dr. Tai Lun Wong, Dr. Vincent Tse and Ms. Joyce Lau from UMF of PolyU and Dr. Curtis Ng and Mr. Benny Leung from Department of Mechanical Engineering, and the administrative staff such as Ms. Lily Tam, Ms. Joanne Cheng, Ms. Celia Wong and Mrs. Michelle Lai. I would also express my appreciation to the colleagues in the Department of Mechanical Engineering who helped me throughout my whole study period.

Last but not least, I would like to appreciate the supports and encouragements from my family. Without their love, understanding and help I would never finish this thesis.

Table of Contents

List of Figures

List of Table

Chapter 1. Introduction

With the rapid development of electronic devices and electrical vehicles, there has been an enormous demand of long battery life and high capacity for the energy storage and conversion devices in the energy field. Lithium ion battery has attracted much more attention in the last decade than ever. However, several limitations still impede the wider application of lithium ion battery, such as the low energy storage capacity, low energy conversion efficiency, slow charging rate, safety issues, etc. Therefore, it will be a great breakthrough to solve these problems and develop lithium ion batteries with high capacity and stable cycle life.

1.1. Basics of lithium ion battery

Generally, a lithium ion battery is consisted by anode, cathode, electrolyte, current collector, separator, binder, conductive additives and so on. Fig. 1.1 shows a lithium ion battery (full-cell) with two electrodes, liquid electrolyte and separator. When the lithium ions diffuse from anode to cathode through electrolyte and neutralize with the electrons passing through the external circuit, the lithiation/discharging process is accomplished. The chemical energy is converted to the electrical energy and the external devices will be charged. Here, a reduction reaction ($\mathrm{A}^{+} + e^{-} \rightarrow \mathrm{A}$) occurs at the cathode while an oxidation reaction ($\mathrm{B} \rightarrow \mathrm{B}^{+} + e^{-}$) occurs at the anode due to the departure of electrons from the anode. When the delithiation/charging process occurs, the chemical energy is stored in the battery. The current collector is a component which receives electrons from the electrodes and transports electrons to the external circuit, and vice versa. The separator is used to prevent short circuit between two electrodes and the binder is mainly applied to increase the adhesion among electrode materials and between electrode materials and current collector. The conductive additives are used to increase the electronic conductivity.

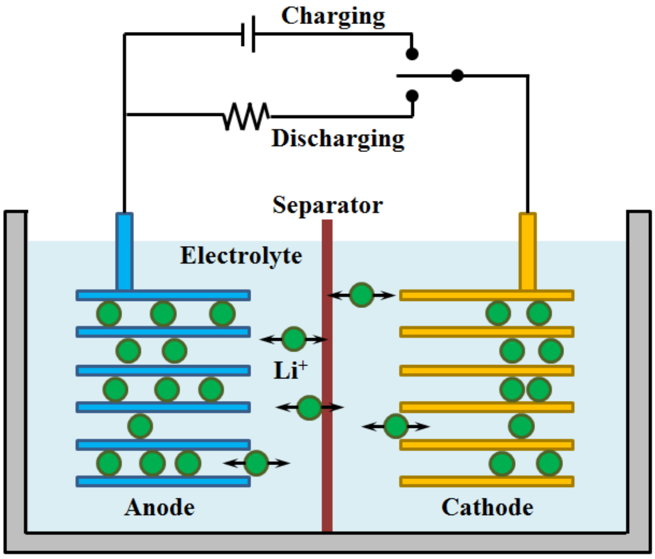

Figure 1.1. Schematic of lithiation/discharging and delithiation/charging process in a lithium ion battery.

There are two types of lithium ion batteries: full-cell and half-cell. A full-cell is consisted by all the above components while a half-cell adopts a reference electrode in order to simplify the measurement and analysis during electrochemical reaction and study the properties of single anode or cathode material. The batteries discussed in this thesis are normally half-cells unless the type is pointed out in the related text. The electromotive force is the electrical potential energy of a unit charge inside the electrical field. The voltage is the driving force in the electrical field, which is equal to the difference of electrical potential between two points in the circuit. Generally, the voltage is influenced by several factors, including temperature and pressure. During discharge process, the voltage is lower than the open circuit voltage since the cell is not in the balance state of thermal dynamic. On the contrary, the voltage is higher than the open circuit voltage during charge process due to internal resistance, over-charge, low ionic conductivity, impurities in the electrode materials, concentration polarization, etc. The capacity of the battery, which is the number of total charge after full discharge at given condition and time, is given by

$$C_{\mathrm{T}} = xF$$

where F is the Faraday constant and x is the mole number of electrons during discharge process. Due to the incomplete reaction of the reactants, the real capacity C_{P} is lower than C_{T}. The relationship between real capacity and current is

$$h = C_{\mathrm{P}} / i$$

where h is the time required for full charging/discharging and i is the current. The charge/discharge rate C_{rate} can be determined as the reciprocal of h. That is to say, when C_{rate} is increased, the time required for full charging/discharging is decreased. The capacity includes the mass capacity and volume capacity which have the units of mA h g^{-1} and mA h cm^{-3}, respectively.

In addition to capacity, the cycle life of lithium ion battery is another key factor which determines the performance of battery. It means the charging and discharging cycle number until the battery is failed. The cycle life is dependent on the structural integrity of the battery materials upon repeated charging and discharging. An irreversible capacity loss after first cycle can be observed due to the formation of a solid electrolyte interface on the surface of electrode materials. A high-performance lithium ion battery should have long stable cycle life as well as high capacity.

1.2. Anode materials

Lithium metal was firstly used as anode material for lithium ion battery due to its high capacity (3860 mA h g^{-1}) during cycling. However, dendrite structure forms on the surface of lithium metal and leads to the short circuit of the battery. In addition, if lithium anode material contacts with water, a large amount of heat will be released. The high temperature results in the thermal decomposition of the active materials, electrolyte and solid electrolyte interface, induces the collapse of the whole structure and probably leads to the inflammation and explosion of the battery.

In order to solve these safety issues, carbon-based anode materials, including graphite, amorphous carbon, carbon nanofiber/nanotube and so on, were developed to substitute the lithium metal. During lithiation of the anode materials, the lithium ions are inserted into the carbon-based anode material through a reduction reaction:

$$\mathrm{C}_6 + x\mathrm{Li}^+ + xe^- \rightarrow \mathrm{Li}_x\mathrm{C}_6 \ (0 \le x \le 1)$$

The structure of the carbon-based anode material changes slightly with only ~12% volume expansion since the lithium ions are inserted into the interlayer space of the carbon, indicating a stable and safe structure during cycling. Carbon-based anode also has high electronic conductivity due to the free π electrons moving freely in each interlayer. However, the low capacity (372 mA h g^{-1}) is the drawback which limits the further application of carbon-based anode materials.

In order to satisfy the increasing demand of long battery life as well as high capacity, other high-capacity anode materials, such as silicon (Si) (4200 mA h g^{-1}), tin (Sn) (992 mA h g^{-1}) and their alloy and composite materials, have been widely studied. In comparison to the insertion and extraction of lithium ions in the carbon-based anode materials, the lithiation and delithiation in these anode materials are the alloying and dealloying processes by the following reaction:

$$\mathrm{M} + x\mathrm{Li}^{+} + xe^{-} \leftrightarrow \mathrm{Li}_{x}\mathrm{M}\ (\rightarrow \text{lithiation}, \leftarrow \text{delithiation})$$

During the above reaction process in the anode materials, the voltage is decreased and a huge volume change occurs. The influence of decrease in voltage can be avoided if the working voltage is enough high. However, the huge volume change is a significant problem for keeping the stability and durability of lithium ion battery. For Si anode, one Si atom reacts with 4.4 lithium ions, leading to ~400% volume expansion during lithiation. Under this circumstance, the ionic bonds in the Li-Si alloy can be easily destroyed. Generally, for inorganic materials composed of ionic bonds, the threshold strain under which no fracture occurs is around 5%. Therefore, such huge volume change may induce the fracture and pulverization of the anode materials, as shown in Fig. 1.2a. In addition, the solid electrolyte interface forming on the surface of the anode materials will be fractured and new solid electrolyte interface will form and consume the electrode materials and electrolyte during cycling, as shown in Fig. 1.2b. Combination of the fracture of anode materials and the repeated formation and fracture of solid electrolyte interface leads to pulverization of the bulk electrode materials, the loss of electronic conductivity, the low capacity retention and the failure of the whole battery, as shown in Fig. 1.2c.

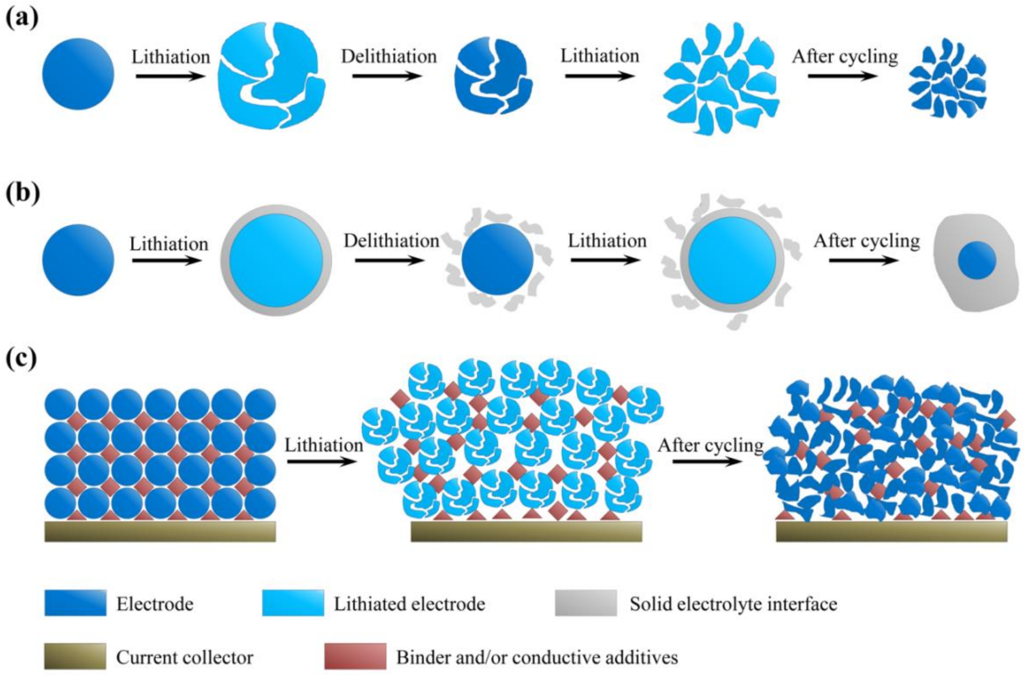

Figure 1.2. Schematics of (a) fracture and pulverization of the electrode material due to the volume change during cycling, (b) consumption of the electrode material by the repeated fracture and formation of solid electrolyte interface during cycling and (c) fracture and pulverization of the electrode materials during cycling.

Several methods have been utilized to mitigate the volume change problem. For example, nanoscale design of the anode materials has been shown to be an effective approach since it releases the stress and prevents the fracture in the bulk materials. Another method is to synthesize the alloy and composite materials based on Si or Sn. The volume change will be deceased due to fewer amounts of lithium ions being inserted into the anode materials. Coating materials with better electronic conductivity have also been applied to constrain the volume change of the anode materials which can effectively prevent the fracture and help achieve a longer cycle life. Modification and revision of the battery components, such as electrolyte, binders, conductive additives and current collectors, show the capability to improve the electrochemical performance of the lithium ion battery.

1.3. The goal and outline of this thesis

The goal of this thesis is to study the lithiation/delithiation and fracture mechanisms of core-shell nanostructured high-capacity anode materials and propose the optimal design guidelines to achieve high capacity and long stable cycle life for the high-performance lithium ion batteries. In Chapter 2, we firstly reviewed recent studies on the high-capacity anode materials, especially the SnO_2 and Si anode materials, including the nanoscale design approaches, the lithiation/delithiation mechanism, the core-shell nanostructured design, other approaches to improve the electrochemical performance and some mechanics-based measurement and analysis. Then in Chapter 3, the synthesis and characterization methods and *in situ* lithiation/delithiation approaches of the high-capacity anode materials were discussed, followed by fundamental reviews of diffusion equations, fracture mechanics and finite element method. Subsequently, the thickness-dependent fracture of the amorphous carbon shell in the carbon-coated SnO_2 nanowire electrode was studied in Chapter 4. An optimal thickness was determined to minimize the amount of carbon and avoid the fracture of the shell by theoretical modeling and finite element simulation. In Chapter 5, the fracture mechanism of the synthesized carbon-coated Si nanoparticle electrode materials was studied through *in situ* lithiation and finite element simulation. It was found that the carbon shell probably expedites the fracture of Si nanoparticle during lithiation. Such fracture can be prevented and the capacity can be maximized through optimizing the geometrical structures of the electrode materials. Then in Chapter 6, the lithiation-induced fracture of the yolk-shell carbon-coated Si nanoparticle electrode materials was studied through the observation of *in situ* lithiation. By optimizing the geometrical structures of the electrode materials through theoretical modeling, the fracture can be avoided and the highest capacity can be achieved. In the following Chapter 7, the Si-coated copper core-shell nanowire electrode materials were synthesized to study the structural integrity of the Si electrode materials on the modified copper current collector during electrochemical cycling. The lithium nanostructures formed during the delithiation process which may induce the volume expansion and lead to the fracture of the Si shell. Finally, the results of this thesis were summarized and discussed, followed by the outlook to the future work in Chapter 8.

Chapter 2. Research background and literature review

Since the known cathode materials provide limited specific capacities, a large amount of studies have been focused on developing and optimizing high-capacity anode materials, such as tin dioxide (SnO_2) and silicon (Si) materials. Nevertheless, these anode materials form alloy with lithium ions and suffer from large volume change during cycling, leading to the fracture of anode and capacity fading of battery. Over the years, researchers have adopted different approaches to solve the volume change problem in order to commercialize these high-capacity anode materials.

2.1. SnO_2 anode materials

2.1.1. Electrochemical performance

The SnO_2 anode materials have a theoretical capacity of 781 mA h g^{-1}, which is around twice of the capacity of carbon anode materials. During lithiation process, the lithium ions are reacting with the SnO_2 anode material by the alloying and dealloying electrochemical processes as [1]

$$4\mathrm{Li}^{+} + \mathrm{SnO}_2 + 4\mathrm{e}^{-} \rightarrow 2\mathrm{Li}_2\mathrm{O} + \mathrm{Sn} \tag{2.1}$$

$$\mathrm{Sn} + x\mathrm{Li}^{+} + x\mathrm{e}^{-} \leftrightarrow \mathrm{Li}_x\mathrm{Sn}\ \left(0 \le x \le 4.4\right) \tag{2.2}$$

In Reaction (2.1), the irreversible chemical transformation occurs with the reduction of SnO_2 into Sn. The large irreversible capacity loss during first lithiation results from this chemical reaction. Reaction (2.2) represents the reversible chemical reaction between Sn and lithium ions, leading to the reversible capacity during the electrochemical cycling. Up to 4.4 lithium ions can be alloyed with each Sn atom, corresponding to a high theoretical capacity of 781 mA h g^{-1}. A reaction potential of ~0.6 V vs. Li/Li$^+$ is required for the reaction between lithium ions and Sn, which is moderately higher than that of carbon-based materials (~0.2 V vs. Li/Li$^+$) [2]. Such a low potential can on the one hand avoid the safety issues of the deposition of active metallic lithium on the anodes and on the other hand ensure the conjunction with widely used cathode materials, such as $LiCoO_2$ and $LiFePO_4$, to construct a secondary lithium ion battery with an overall cell potential of more than 3V.

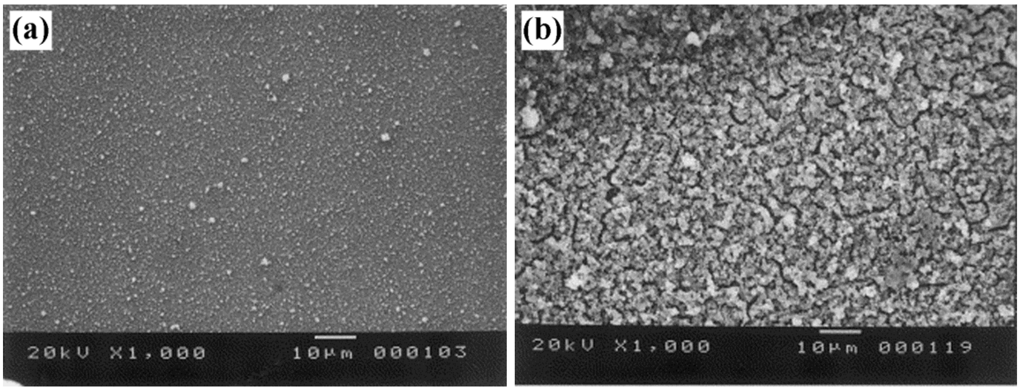

Figure 2.1. SEM images showing the morphology of the thin film SnO_2 anode material prepared by electrostatic spray deposition method (a) before and (b) after cycling (20 cycles) (adapted from [3]).

However, the biggest problem for SnO_2 anode material is the large volume change (~280%) during cycling. Such a large volume change induces a high internal stress in the anode materials, leading to the fracture, pulverization and disintegration of the anode materials and loss of electric contact with the current collector after cycling, as shown in Fig. 2.1 [3]. These problems result in the fast capacity fading and unstable cycle life of the SnO_2 anode materials, hindering its wide application in lithium ion battery [3-5]. The capacities of the thin film SnO_2 anode materials decay quickly within 50 cycles, as shown in Fig. 2.2 [5]. The SnO_2 anode materials were synthesized by three different approaches (marked by A, B and C) and the cut-off voltage is 0.2 – 1.3 V vs. Li/Li^+.

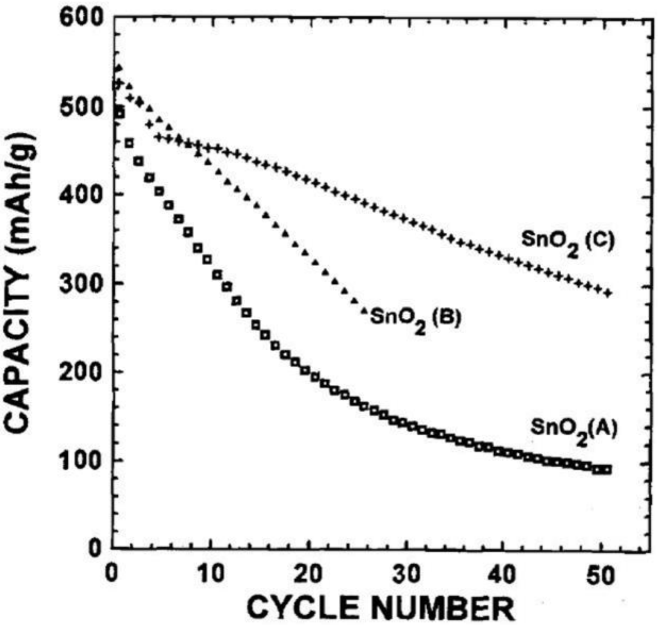

Figure 2.2. Electrochemical cycling performance of the thin film SnO_2 anode materials (adapted from [5]).

2.1.2. Nanoscale design

Downsizing the anode materials to nanoscale is an effective way to improve the electrochemical performance of the SnO_2 anode materials [6-9]. The nanostructures include 0-dimensional (0-D) nanoparticles [10-14], 1-dimensional (1-D) nanowires [15-17] and nanotubes [18-20], 2-dimensional (2-D) nanosheets [21,22] and 3-dimensional (3-D) hollow [23-25] and porous nanostructures [26,27], as shown in Fig. 2.3.

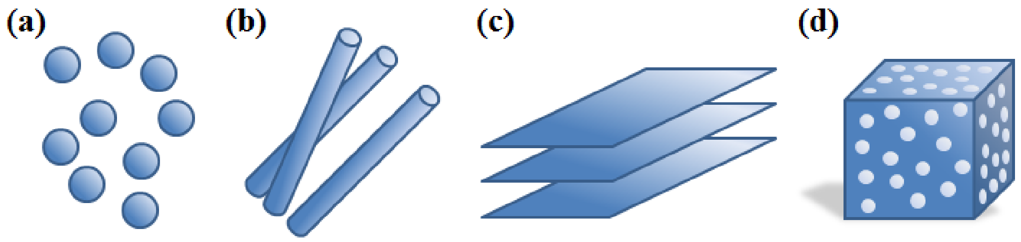

Figure 2.3. Schematics of the nanoscale structures of (a) 0-D nanoparticles, (b) 1-D nanowires and nanotubes, (c) 2-D nanosheets and (d) 3-D hollow and porous nanostructures.

The 0-D SnO_2 nanoparticles were synthesized through different approaches and decreasing the sizes to several nanometers was shown to achieve the best electrochemical performance [11,12]. The micro-structured SnO_2 anode materials assembled by the SnO_2 nanoparticles, such as the hollow microspheres [13] and the mesoporous microspheres [14], showed much better electrochemical performances than the thin film anodes. However, the nanoparticle electrodes tend to aggregate during cycling and become vulnerable to pulverization and fracture [18]. On the contrary, the 1-D nanostructure has curved surface and is less mobile than the 0-D nanostructure, indicating less chance of aggregation during cycling. For the SnO_2 nanowire electrode materials, the large surface-to-volume ratio and high aspect ratio increase the electronic and ionic conductivity due to the 1-D nanowire character and provide more reaction cites along the nanowire than the bulk materials during cycling, leading to better cycling performance [16]. The SnO_2 nanotube structure has one more advantage: it can accommodate the volume change by its internal space, which thereby results in lower stresses [18]. The extremely thin 2-D nanosheet structure shortens the pathway of electrons and lithium ions and accommodates the large volume change due to its high flexibility [21]. The 2-D SnO_2

nanosheets were utilized to fabricate 3-D hierarchical structures to avoid dense aggregation, increase interconnections among nanosheets, accommodate the large volume change and facilitate the insertion and extraction of lithium ions [27]. The 3-D nanostructures, such as the hollow structures [23,25,28] and the nanoboxes [24], are able to withstand the volume change by the void space, increase capacity especially at high rate cycling by the large surface area and improve the diffusion of lithium ions through the thin walls.

These kinds of nanoscale design increase the surface/volume ratio and the contact interface between electrode and electrolyte, leading to fast electronic and ionic transportation. Besides, the nanomaterials are more resistant to compressive and tensile stress and strain than the bulk materials, resulting in stable structure during electrochemical cycling. The nanomaterials are also believed to ameliorate the irreversible electrochemical reactions in the anode materials [29].

2.1.3. Lithiation and delithiation mechanism

To further improve the electrochemical performances of the nanoscale SnO_2 anode materials, it is required to understand the reaction process and the failure mechanism of the SnO_2 nanostructures during lithiation and delithiation. Several issues cause the failure of the anode materials: the fracture or pulverization due to the extremely large volume change, the repeated fracture and formation of the solid electrolyte interface, the separation of anode materials from the current collector and so on. In order to investigate the mechanism behind the above issues, i*n situ* lithiation and delithiation techniques have been used to reveal the phenomena of lithium ion insertion and extraction and the fracture and failure mechanisms of the nanostructured anode materials [30-32].

In situ TEM has been widely used in real-time measurements of the materials' structure and properties [33-40]. This technique provides exact morphology evolution, high spatial atomic scale resolution and real-time composition and structure analysis. Until recently, the *in situ* TEM was utilized to study the electrochemical process in the lithium ion battery [41-44]. The nano-battery setup inside the TEM generally includes two types: the sealed cell [45,46] and the open cell [41-44]. The sealed cell adopts an electron-transparent layer to separate the volatile electrolyte from high vacuum. The electrolytes with high vapor pressure, such as ethylene carbonate, diethyl carbonate and dimethyl carbonate, which are normally used in real lithium ion batteries, can be used inside the TEM [30]. The electrode materials can be directly observed when immersed in the electrolyte. However, it takes much workload to assemble the complex setup and much care should be taken to avoid the leakage of the electrolyte. It is difficult to control and manipulate the electrode materials and conduct the composition and structure analysis. Also, since the electrons need to penetrate through the transparent layer, the image quality is usually poor. Therefore, the open cell was developed in which the electrolytes are vacuum-compatible. Two kinds of electrolytes were used: the liquid electrolyte with extremely low vapor pressure [41-43] and the solid lithium-containing electrolyte [44]. The open cell offers much higher resolution and positioning control due to the direct observation, unlike those in the sealed cell. Since only the electrode materials are lithiated and delithiated, the effects from other battery components can be eliminated. Fig. 2.4a shows the schematic of an open cell setup for the *in situ* lithiation and delithiation, in which the electrolyte can be liquid or solid. The liquid electrolyte, due to the high surface tension force and fluidity, is more suitable for the 1-D anode materials with high aspect ratio. But it suffers from fast degradation when subject to electron beam exposure if the electron dosage is higher than ~10^{-3} A cm^{-2}, leading to loss of lithium ion transportation capability. The solid electrolyte, usually the Li_2O layer on the surface of lithium metal, is a lithium ion conductive but electron insulated material [47]. Unlike the immersing of partial or entire electrode materials in liquid electrolyte, the electrode contacts with the solid electrolyte, making it visible with size down to a few nanometers. The electron beam dose cannot be high otherwise the Li_2O solid electrolyte is easy to be decomposed.

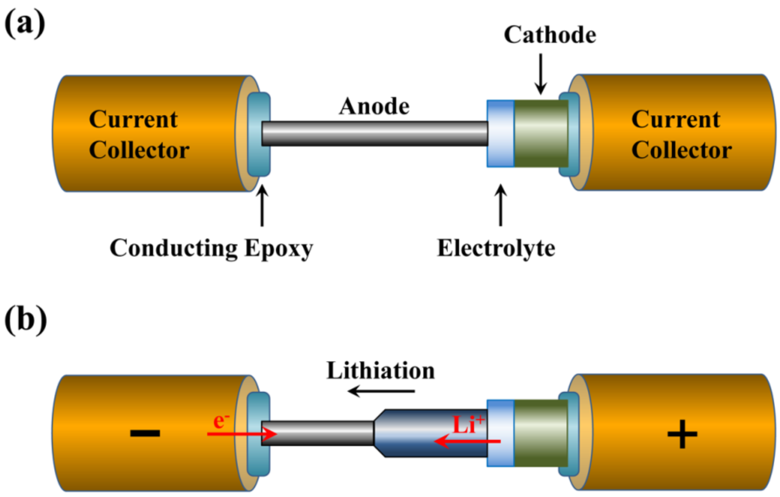

Figure 2.4. (a) Schematic of the nanoscale open-cell setup for *in situ* lithiation/delithiation. (b) The nanowire anode is partially lithiated after a voltage is applied.

As shown by the schematic setup in Fig. 2.4a, the electrode materials, such as the nanowires or the nanoparticles, are adhered on one current collector by conductive epoxy and the reference electrode materials are adhered on the other current collector. A solid or ionic liquid electrolyte is used to provide the pathway for diffusion of lithium ions and prevent the penetration of the electrons. After the electrode materials contact with the electrolyte and a voltage is applied, the electrode materials will be lithiated, as shown in Fig. 2.4b.

Huang et al conducted the *in situ* lithiation in a single crystalline SnO_2 nanowire electrode [41]. The nano half-cell was consisted by a SnO_2 nanowire anode, an ionic liquid electrolyte and a $LiCoO_2$ cathode. After applying a voltage of -3.5 V, the nanowire was elongated by 60% and expanded in the radial direction by 45% during lithiation, corresponding to a total volume expansion of ~240%. Another interesting phenomenon was the moving reaction front, which is a dislocation cloud separating the pristine crystalline SnO_2 and the reactants of amorphous Li_xSn and tetragonal Sn nanoparticles dispersed in amorphous matrix, as shown in Fig. 2.5. The pristine crystalline phase and lithiated amorphous phase were separated by the reaction front of the dislocations, accompanied by the volume expansion of lithiated part. A large in-plane misfit stress was induced as the reaction front propagated. Such a large volume expansion, the phase transformation and plasticity, and the large stress accumulation during lithiation can be the major reasons for the cracking and fracture of the SnO_2 anode materials, leading to their poor electrochemical performance. This study provided an approach to observe the nanoscale lithiation process and important mechanics-based insight for the design of lithium ion batteries.

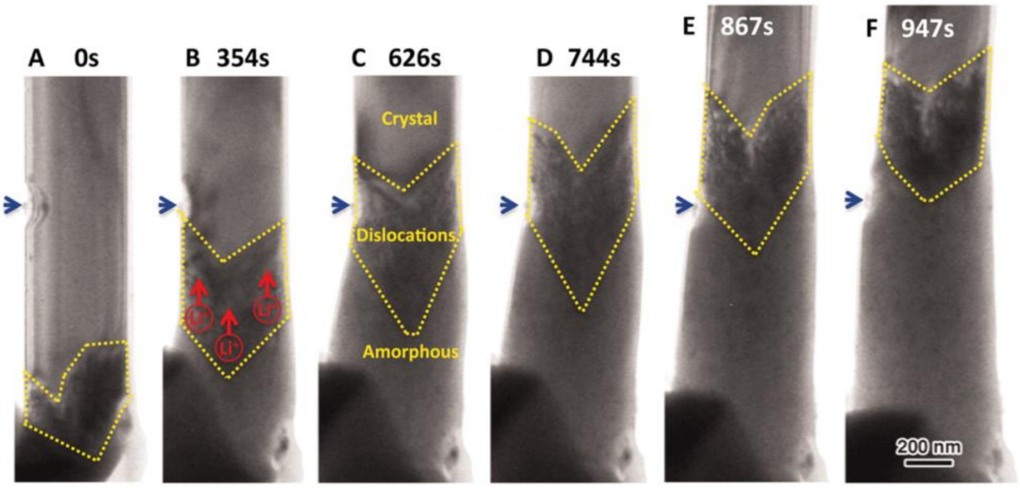

Figure 2.5. The moving reaction front during i*n situ* lithiation of a single SnO_2 nanowire anode material (adapted from [41]).

Further studies provided more details about the structure and phase evolution of the SnO_2 nanowire during *in situ* lithiation. The nanowire was fully soaked in the ionic liquid electrolyte and after initial charge, the single crystalline structure of the SnO_2 nanowire became amorphous through a solid-state amorphization process, followed by the nucleation and growth of the Li_xSn particles [42]. With the coarsening of the Li_xSn particles, Sn was consumed, leading to the formation of Li_yO amorphous phase. Later studies also found in atomic scale that the lithium ions prefer to diffuse along the [001] direction in the $\{200\}$ planes, accompanied by the generation of lithiated stripes and mixed dislocations in front of the reaction front which facilitated the insertion of lithium ions into the crystalline SnO_2 nanowire [43,44]. At the later stages of lithiation, both Sn and Li_xSn nanoparticles were observed to form in the matrix of Li_2O.

2.2. Silicon anode materials

2.2.1. Electrochemical performance

Back to the 1970s, Li-Si alloys was found to form through the charge-discharge cycles of a high-temperature cell tested in the range of 650 – 750 K [48]. Further studies revealed that $Li_{12}Si_7$, $Li_{14}Si_6$, $Li_{13}Si_4$ and $Li_{22}Si_5$ alloys formed during the alloying process of lithium ions in the silicon anode materials [49]. Up to 4.4 lithium ions can be accommodated by each silicon atom, leading to a theoretical capacity of 4200 mA h g^{-1}. Unlike the multi-step reactions of the SnO_2 anode, the electrochemical alloying/dealloying process of Si anode involves the following reversible reaction as

$$x\mathrm{Li}^{+} + \mathrm{Si} + x\mathrm{e}^{-} \leftrightarrow \mathrm{Li}_{x}\mathrm{Si}\ (0 \le x \le 4.4) \tag{2.4}$$

The above reaction is accompanied by a volume change of ~400%, leading to pulverization and fracture of the Si anode materials and loss of ionic and electronic conductivity. Due to the arising of the internal resistance and consumption of the useful anode materials and electrolyte, the Si powder anode materials and micro thin film Si anodes showed poor cycling performance [50-52]. Even though obtaining a high initial charge capacity of 3260 mA h g^{-1}, only ~35 % coulombic efficiency is achieved during the first cycle, as shown in Fig. 2.6 for the micro Si powder anodes. The capacity fades to a value lower than 200 mA h g^{-1} within 10 cycles with a cut-off voltage of 0 – 2 V *vs*. Li/Li^{+}.

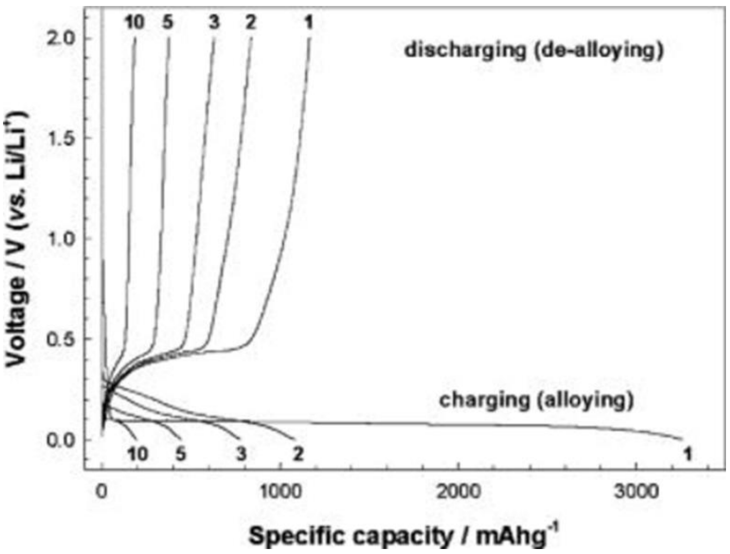

Figure 2.6. Galvanostatic charge-discharge voltage profiles for the Si powder anode materials within 10 cycles (adapted from [50]).

It can be seen that the long potential plateau of ~0.1 V represents the formation of the Li-Si alloy during lithiation process, accompanied by a large volume expansion. The delithiation process mainly occurs above 0.4 V, accompanied by the large volume contraction and loss of electronic contact between the anode materials and the current collector during discharge process. The potential reaches at the discharging cut-off limit (2 V) earlier due to the abrupt increase of internal resistance, leading to the incomplete dealloying reaction and a much lower discharge capacity. The working potential of silicon anode ranges between 0 and 0.4 V, which is applicable for the lithium ion batteries.

2.2.2. Nanoscale design

In order to improve the electrochemical performance of the Si anode materials, different nanostructural design approaches have been studied [53-58]. The 0-dimensional (0-D) Si nanoparticles were synthesized by laser-induced silane gas reaction, as shown by the SEM images in Fig. 2.7a [59]. The Si nanoparticles were mixed with carbon black and polyvinylidene fluoride as anode materials with a weight ratio of 4:4:2. Fig. 2.7b shows the morphology of the aggregated Si nanoparticles after first cycle and Fig. 2.7c shows the cycling performance of the cell by using the above anode materials with a cut-off voltage of 0 – 0.8 V *vs*. Li/Li^+. In comparison with Fig. 2.6, both the reversible capacity and the cycle life of the Si anode materials have been improved due to the decreased sizes of the Si particles. The electrochemical performance of the Si nanoparticles was further improved by preparing the electrode materials using the method of aqueous processing in an acidic medium [60]. The Si nanoparticles prepared in buffered pH 3 solution show better performance than those prepared in deionized water or aqueous H_2SO_4 pH 3 solution. Such Si nanoparticle anode materials achieve a long cycle life of more than 700 cycles and a high reversible capacity of 960 mA h g^{-1} with respect to the electrode (or 1200 mA h g^{-1} with respect to Si), as shown in Fig. 2.7d. The mechanical strength is improved and the electronic contact becomes better by the enhanced covalent bonding between the Si nanoparticles and the carboxymethyl cellulose (CMC) binder due to the buffered pH 3 solution. It was also found that a critical size of ~10 nm for the Si nanoparticles exists so that the best electrochemical performance can be achieved [61], as shown by the blue symbols in Fig. 2.7e. The ~10 nm nanoparticle anode shows much better performance than the ~5 nm (red symbols) or ~20 nm (black symbols) Si nanoparticle anode materials. The performance is also better than the previous reported results of the nestlike Si particles anodes [62] and the commercial Si powder anodes [63]. Better performance can be obtained by carbon coating technique, indicated by the orange symbols in Fig. 2.7e. It has also been reported that the Si nanoparticles can be synthesized by using the rice husks as Si source and the anode achieves a long cycle life of more than 300 cycles with a high reversible capacity of 2790 mA h g^{-1} [64].

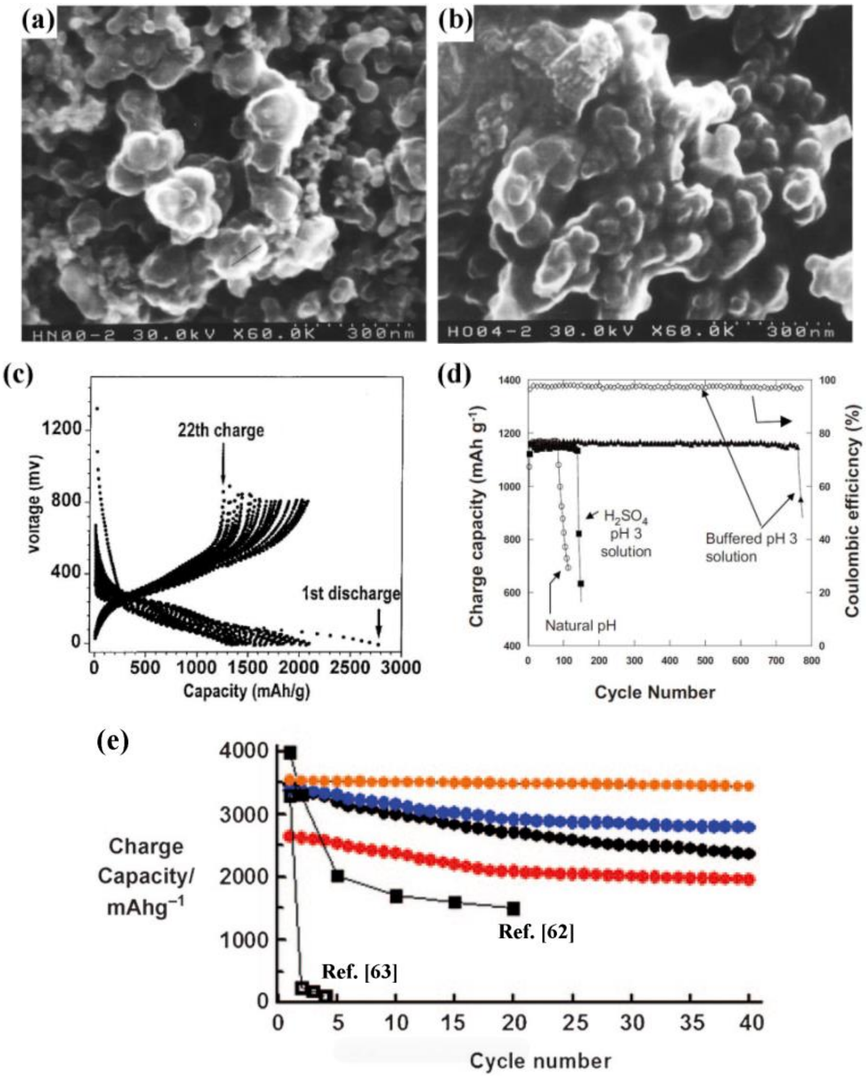

Figure 2.7. SEM images showing the morphology of the Si nanoparticles (a) before and (b) after first cycle. (c) Galvanostatic charge-discharge voltage profiles for the Si nanoparticle anode materials for 22 cycles (adapted from [59]). Electrochemical cycling performance of the Si nanoparticle anode materials (d) prepared by aqueous processing in an acidic medium (adapted from [60]) and (e) with different sizes of 5 nm (red), 10 nm (blue) and 20 nm (black) and the carbon-coated 10 nm Si nanoparticle anodes (orange) (adapted from [61]).

The 1-dimensional (1-D) Si nanowire anode materials were synthesized through different approaches, such as the vapor-liquid-solid synthesis process [65] and the metal-induced chemical etching process [66]. Due to the large aspect ratio of the 1-D Si nanowires as shown in Fig. 2.8a, the anode materials have short lithium insertion pathways and good electrical contact with the current collector. The synthesized Si nanowires were directly grown on the stainless steel current collector, as shown by the inserted image of the cross sectional view in Fig. 2.8a. In this way, binders and conducting additives are not required. The arrangements of the Si nanowires provide good mechanical strength and enough space to accommodate the volume change during cycling. After cycling, the sidewalls of the Si nanowires become rough as shown in Fig. 2.8b, the diameter of the Si nanowires is increased by ~58% but the Si nanowires still remain contact with the current collector. In comparison with Si nanocrystal and graphite anode materials, the Si nanowire anode materials achieve much higher reversible capacity at the rate of C/20, indicating improved electrochemical performance, as shown in Fig. 2.8c. The high capacity loss during the first cycle can be eliminated by prelithiation technique on the Si nanowire anode materials [67].

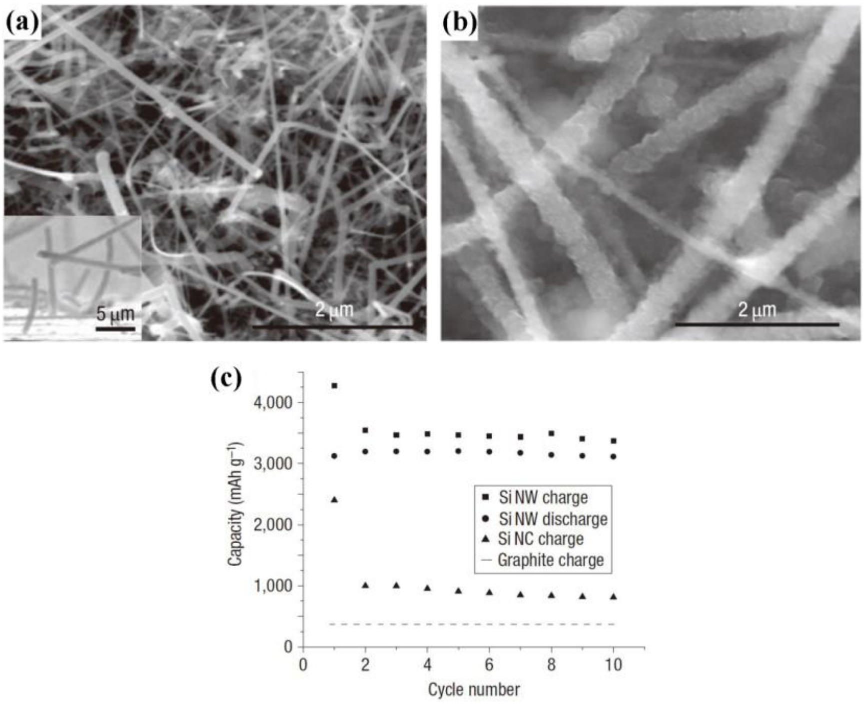

Figure 2.8. SEM images showing the morphology of the Si nanowire anode materials (a) before and (b) after cycling. Inserted is cross-sectional view. (c) Electrochemical cycling performance of the Si nanowire anode, the Si nanocrystal anode and the graphite anode materials (adapted from [65]).

The 1-D Si nanotube anode materials were synthesized to improve the electrochemical performance through reductive decomposition of silicon precursor in alumina template and etching process [68], chemical vapor deposition of Si on sacrificed hydrothermally grown nanorod template [69] and surface sol-gel reaction on electrospun organic nanowires [70]. The high specific surface area and the large aspect ratio, as shown in Figs. 2.9a and b, facilitate the transportation of lithium ions and the internal space of the nanotube accommodates the large volume change during cycling. Fig. 2.9c shows that the Si nanotube anode materials still remain integrity after 200 cycles. The electrochemical performance, tested by a pouch-type lithium ion cell with $LiCoO_2$ as the cathode material and the Si nanotube as anode materials at the rate of 3 A g^{-1}, indicates high reversible capacity and coulombic efficiency, as shown in Fig. 2.9d. The good electrochemical performance of the Si nanotube anode materials demonstrates their potential application for lithium ion battery.

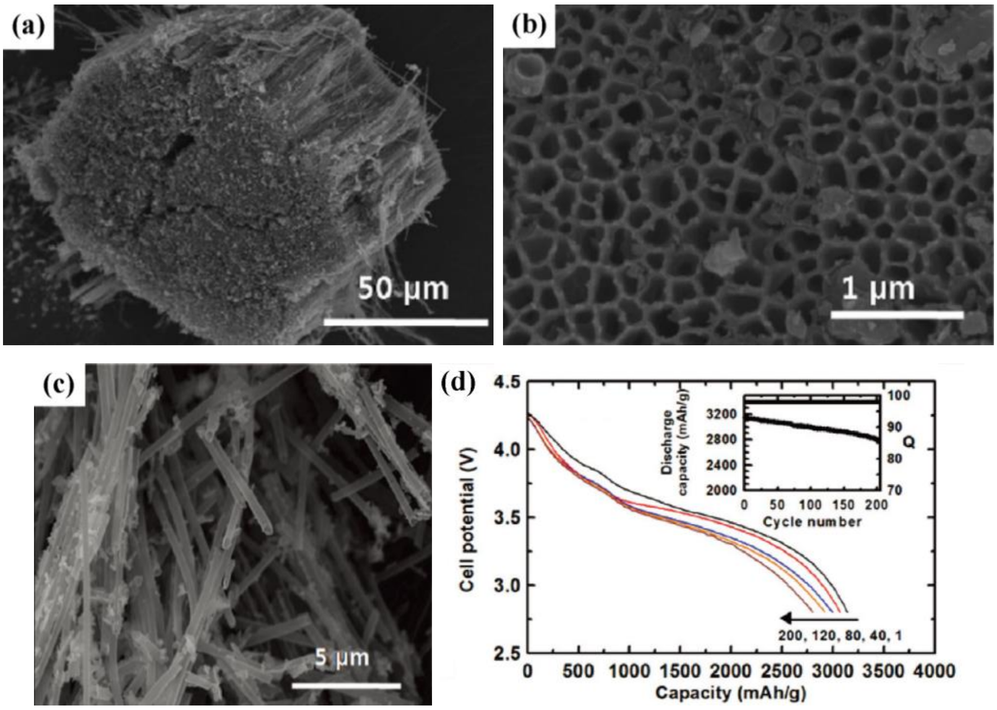

Figure 2.9. SEM images showing the morphology of the Si nanotube anode materials (a-b) before and (c) after 200 electrochemical cycles. (d) Electrochemical cycling performance of the Si nanotube anode materials (adapted from [68]).

The 2-D Si nano thin film anode materials, synthesized through different vacuum deposition approaches, showed good electrochemical performance [71-74]. According to the Griffith-Irwin relation, the fracture strength increases when the thickness of the thin film decreases [75]. The Si nano thin film anode material has higher fracture resistance than thicker film when subject to the volume change during lithiation and delithiation. Figs. 2.10a and b show the morphology of the Si nano thin film anode materials [71]. The Si nano thin film anode obtains better cycling performance than the Si nanocrystal, the bulk Si and the graphite anodes at the rate of C/4, as shown in Fig. 2.10c [71]. Further studies [72,73] showed that the vacuum deposited Si nano thin film on the roughened Ni current collector achieved long cycle life of over 3000 cycles with a high reversible capacity of over 2000 mA h g^{-1}. The improved cycling performance is attributed to the anti-pulverization characters of the nano thin film structures and the increased interfacial strength between the anode materials and the roughened current collector. The current collector was also developed to combine with soft substrate to release the stresses in the Si thin film anode [74]. When subject to volume change during cycling, the soft substrate will deform and balance the buckling-induced bending and electrochemically lithiation/delithiation-induced in-plane stress in the Si thin film anode.

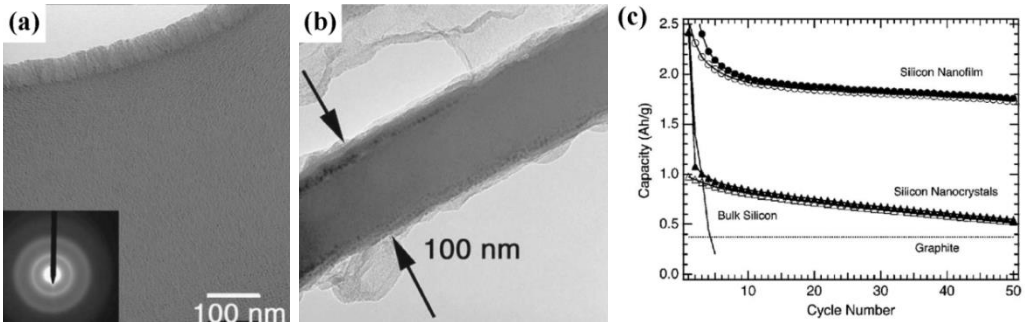

Figure 2.10. TEM images showing the (a) planar view and (b) cross-sectional view of the evaporated Si nano thin film. Inserted is the electron diffraction pattern showing the amorphous structure of the Si thin film. (c) Electrochemical cycling performance of the Si nano thin film, the Si nanocrystal, the bulk Si (adapted from [59]) and the graphite anode materials. The dark and light symbols show the discharge and charge capacities, respectively (adapted from [71]).

The 3-D Si porous structured anode materials were synthesized through various approaches [76-88]. The 3-D Si macroporous anode was synthesized through a magnesiothermic reduction approach by using mesoporous silica powder as Si source [76]. The mean pore size, as shown in Figs. 2.11a and b, is around 200 nm. The electrochemical performance in Fig. 2.11c reveals that the macroporous structure obtains a cycle life of over 100 cycles and a reversible capacity of over 1600 mA h g^{-1} with a cut-off voltage of 0.005 – 1.0 V *vs.* Li/Li^+ at the rate of 0.2C. The improved cycling performance is attributed to the sufficient void space which can accommodate the volume change during lithiation and delithiation. The cycling performance was further improved to achieve more than 1000 cycles with a reversible capacity of ~750 mA h g^{-1} [85]. The volume expansion was controlled to below 30% at full lithiation and no pulverization was observed based on *in situ* TEM characterizations. Besides the micro-sized porous structure, the 3-D Si nanoporous spheres were prepared by a hydrolysis process with surface-protected magnesiothermic reduction, as shown in Figs. 2.11d and e [88]. The anode material obtains a high reversible capacity of ~1500 mA h g^{-1} at a current density of C/2 after 500 cycles, as shown in Fig. 2.11f. In addition to the large void space, the good cycling performance is due to the homogenous stress-strain distribution inside the nanoporous Si sphere during electrochemical cycling.

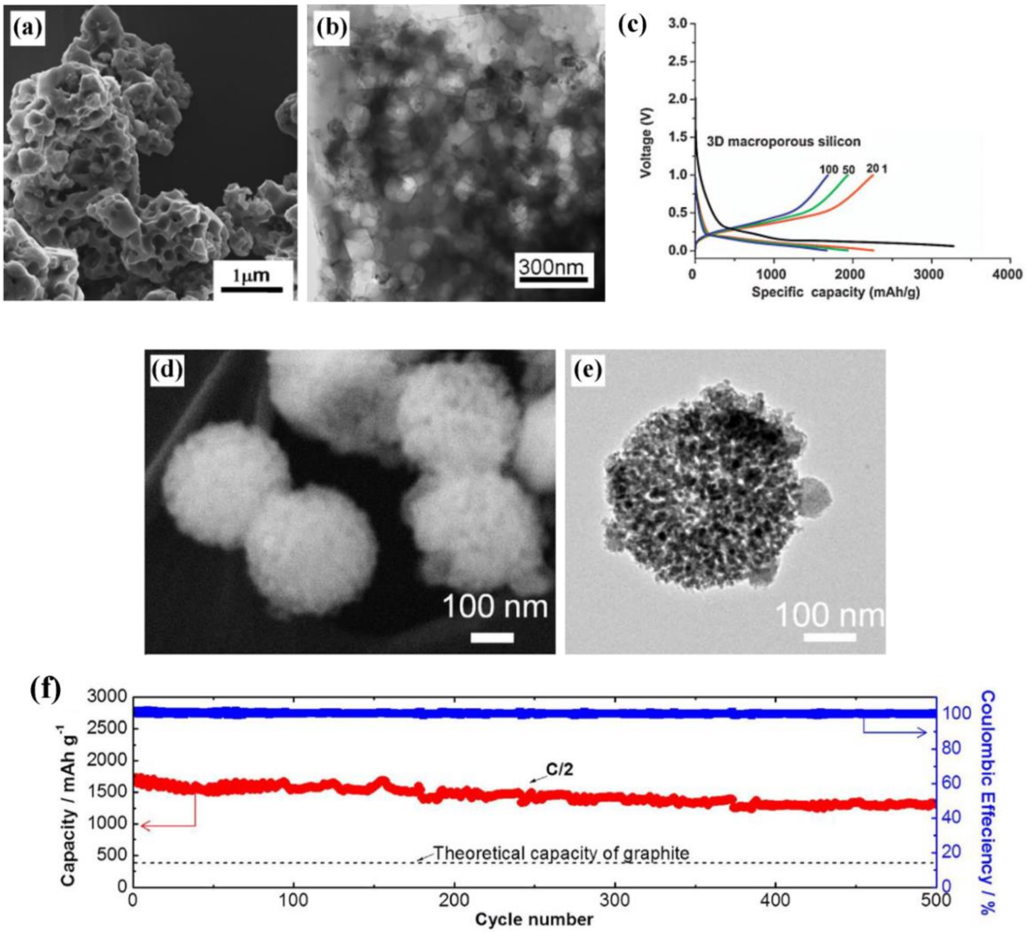

Figure 2.11. (a) SEM and (b) TEM images showing the morphology of the 3-D Si macroporous anode material. (c) Voltage profile showing the electrochemical performance of the Si macroporous anode material (adapted from [76]). (d) SEM and (e) TEM images showing the morphology of the 3-D Si nanoporous anode material. (f) Electrochemical cycling performance of the Si nanoporous anode material (adapted from [88]).

The electrochemical performance of the Si anode materials has been improved a lot by the nanoscale design approaches. Due to the different synthesis and testing approaches, as well as the various electrolytes, cathode materials and battery structures, it is difficult to judge which nanostructure is the best one. In order to further improve the performance, on the one hand new structures are required to be designed and on the other hand further optimization on the existing structures should be studied.

2.2.3. Lithiation and delithiation mechanism

In order to find out the failure mechanism of the nanostructured Si anode materials and provide guidance to improve the electrochemical performance of these materials, *in situ* lithiation and delithiation characterizations have been conducted. The crystalline Si nanowire shows anisotropic swelling during lithiation [47,89-91]. Fig. 2.12a shows the pristine crystalline Si nanowire with a twin boundary parallel to the axis, as shown in Fig. 2.12b. The crystalline directions are confirmed by the electron diffraction pattern in Fig. 2.12c. The lithiation process can be seen from Figs. 2.12d-f, in which the reaction front, marked by the red arrow, propagates from the end of the lithium metal to the other end with a diametric expansion of only 17% when observed from the $[1\bar{1}0]$ direction. A larger expansion can be seen by tilting the nanowire to the viewing direction of $[11\bar{1}]$ and a crack can be observed in the center of the lithiated Si nanowire, as shown in Fig. 2.12h. By examining the volume expansion of all the nanowires, the radial expansion (~170%) along $\langle 110\rangle$ direction is much higher than that (~20%) along $\langle 111\rangle$ direction. Crack develops in the central axis of the nanowire after the residual Si core is completely consumed, leading to a splitting of the nanowire, as shown in Fig. 2.12h. This lithiation-induced fracture of the crystalline Si nanowire is induced by its anisotropic volume expansion, indicating that the nanowires grown along the $\langle 110\rangle$ axis can best suppress the fracture since the volume expansion will be mainly along the longitudinal direction of the nanowire. Such anisotropic volume change can be used for optimal design of the nano pillar array Si anode materials. For example, the volume change of the $\langle 110\rangle$-oriented Si nanopillar is along the out-of-plane axis direction, leading to better adhesion with the current collector. Besides, the volume expansion of the $\langle 111 \rangle$-oriented Si pillar is along the in-plane six $\langle 110 \rangle$ directions, leading to widening rather than elongation of the nanopillars. Due to the isotropic lithiation process, the amorphous Si nanowire should be more resistant to crack than the crystalline one.

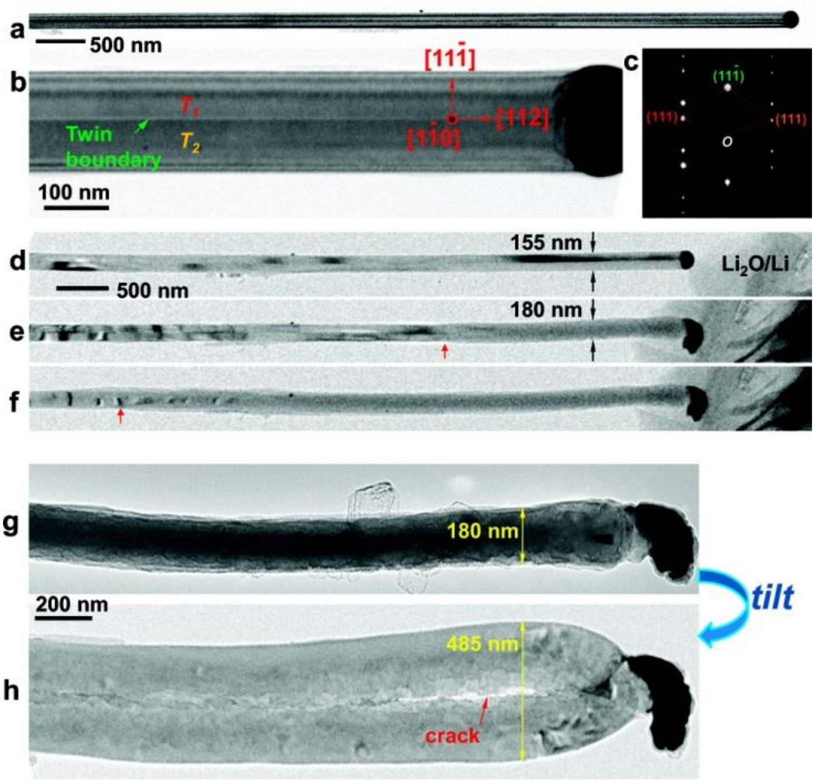

Figure 2.12. TEM images showing the (a) morphology and (b) crystallographic directions of the pristine Si nanowire which are confirmed by the electron diffraction pattern in (c). (d-f) Snapshots of the lithiation process of the Si nanowire. Volume expansion of the Si nanowire viewed from (g) $[1\bar{1}0]$ and (h) $[11\bar{1}]$ directions (adapted from [47]).

Further studies of the Si nanowire and the amorphous Si layer-coated carbon nanotube showed that the Si firstly transforms to an amorphous Li_xSi phase and spontaneously crystallizes to a Li-Si compound by a congruent phase transition process when the stoichiometric number x of a-Li_xSi reaches 3.75 [92-98]. A structure of crystalline Si core and amorphous Li_xSi shell forms after lithiation since the lithiation occurs from the surface towards the central axis of the Si nanowire [94]. For the amorphous Si-coated carbon nanofiber, due to the fast lithiation along the a-Si/carbon interface, a sandwich-lithiation mechanism was observed during *in situ* lithiation [99]. An electrochemical welding of cross-contact Si nanowires was observed, which is believed to improve the facile diffusion of lithium ions, increase the energy density and obtain a self-healing mechanism for lithium ion battery [100].

Besides Si nanowires, Si nanoparticles have also been widely studied. A size-dependent fracture phenomenon was observed for both crystalline and amorphous Si nanoparticles [101,102]. Figs. 2.13a-e show the lithiation-induced fracture of a crystalline Si nanoparticle, in which crack initiates at the surface and propagates into the center, leading to the fracture of the nanoparticle. It was found that the tensile stress generated in the outer layer of the lithiated Si shell is responsible for the crack initiation. The polycrystalline structure of the lithiated Si is confirmed by the electron diffraction pattern as shown in Fig. 2.13f. The threshold sizes, below which no fracture occurs during lithiation, are ~150 nm and ~870 nm for crystalline and amorphous Si nanoparticles, respectively. The decreased threshold size for crystalline Si nanoparticle may be due to several reasons: the larger volume expansion of crystalline Si upon lithiation than the amorphous one, the stress intensification due to the anisotropic lithiation in crystalline Si and so forth [102]. The reaction front in the Si anode materials is a sharp interface (~1 nm thickness) separating the lithiated Si and pristine part. For crystalline Si, the reaction front moves through a ledge mechanism and slows down during lithiation [103-105].

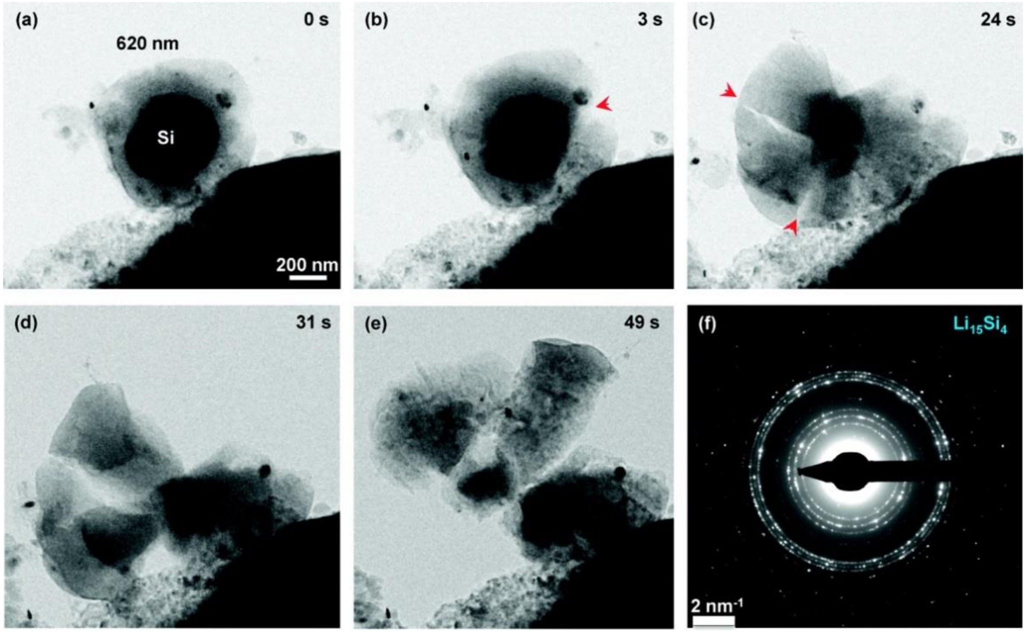

Figure 2.13. (a-e) Snapshots of the lithiation-induced fracture of a crystalline Si nanoparticle and (f) electron diffraction pattern of the lithiated Si at the end of lithiation (adapted from [101]).

2.3. Core-shell structured anode materials

The degradation of the high-capacity electrode nanomaterials is mainly caused by the volume change-induced fracture upon lithiation and delithiation, especially for those with sizes larger than the threshold values, as shown in Fig. 2.13. Another issue exacerbating the consumption of electrode materials and electrolyte is the repeated fracture and formation of the solid electrolyte interface on the surface of the electrode materials during cycling. Consider the bulk electrode materials consisted by the nanomaterials; the disintegration of electrode materials and loss of electronic contact between the bulk materials and the current collector lead to the capacity fading and short cycle life of the lithium ion battery. In order to solve the above issues and improve the cycling performance of the electrode materials, coating materials, such as carbon [106-114], metal [115-118] and oxide [117,119], have been used to constrain the volume change and prevent the fracture of solid electrolyte interface. The solid electrolyte interface survives due to the decreased volume change and the Si electrode will not be consumed as long as the structural integrity of shell can be maintained during cycling, as shown in Fig. 2.14.

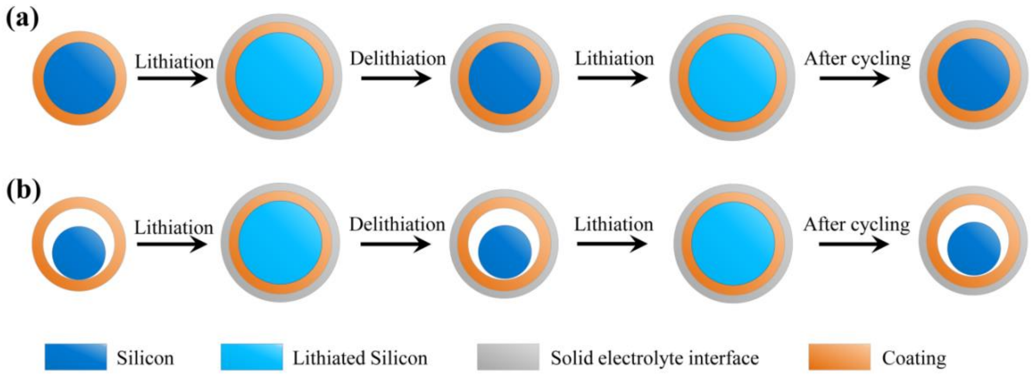

Figure 2.14. Stable cycling of (a) carbon-coated Si nanoparticle/nanowire electrode and (b) yolk-shell carbon-coated Si nanoparticle/nanowire electrode.

The electrochemical performance of the carbon-coated SnO_2 and Si anode materials has been widely studied. Figs. 2.15a-c show the morphology of the carbon-coated Si nanoparticle anode materials prepared by spray-pyrolyzation at 400 C° [108]. It can be seen that the carbon shell is amorphous while the Si core is crystalline. The conductivity of electron and the diffusivity of lithium ion are improved by the shell and the charging rate can be increased by one order of magnitude [94]. Most importantly, the electrochemical performance of the Si anode is improved a lot by carbon shell with certain weight ratio in comparison with the bare Si anode and the carbon-coated Si anodes spray-pyrolyzed at 300 and 500 C°, as shown in Fig. 2.15d.

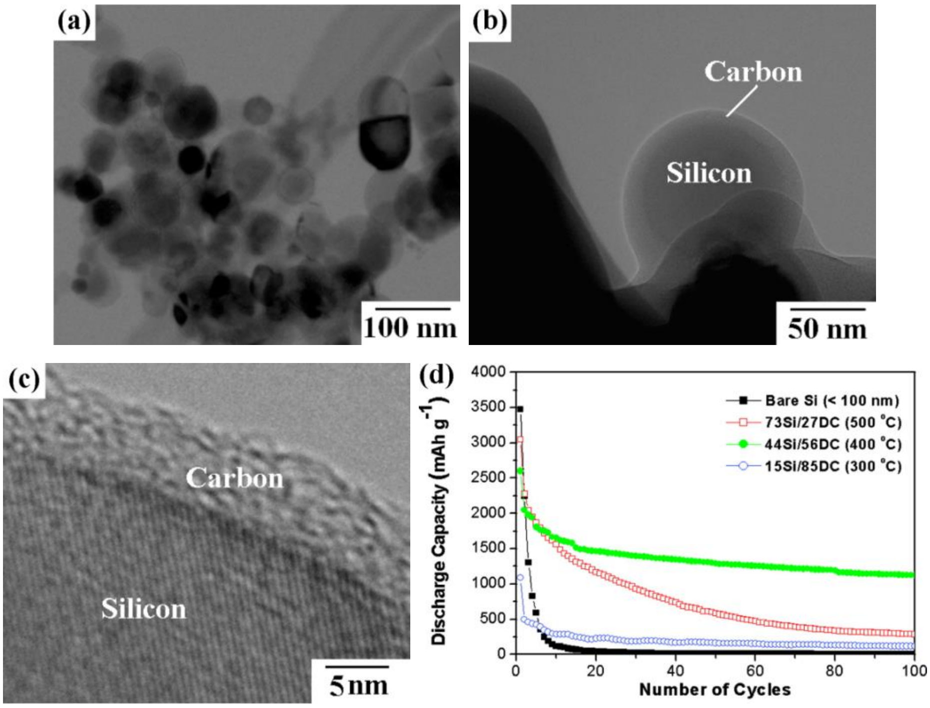

Figure 2.15. (a-c) TEM images showing the morphology of the carbon-coated Si nanoparticle electrode materials spray-pyrolyzed at 400 C°. (d) Electrochemical cycling performance of the bare Si nanoparticle electrode material and the carbon-coated Si nanoparticle electrode materials (adapted from [108]).

Several *in situ* lithiation/delithiation experiments and theoretical studies were carried out to study the effect of carbon shell on the electrode materials during lithiation and delithiation [94,120]. *In situ* lithiation of the crystalline Si nanoparticles which are embedded in the carbon matrix revealed that the carbon matrix may fracture due to the lithiation-induced volume expansion of the Si nanoparticles, as shown in Fig. 2.16 [120]. After lithiation, the carbon matrix is cracked as shown by the arrows in Fig. 2.16c. An analytical solution was carried out to calculate the tensile hoop stress in the carbon shell at different stages of lithiation based on a simplified model consisted of spherical carbon shell and Si core, in which the plastic deformation was not considered. The analytical results showed that the maximum tensile stress becomes higher than the fracture strength of carbon shell, leading to the crack of the carbon shell.

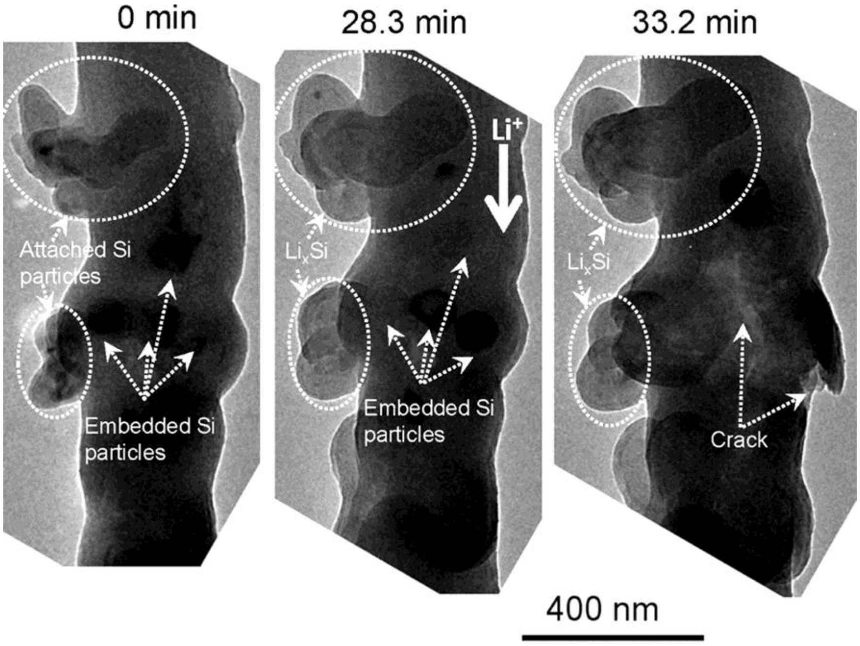

Figure 2.16. Crack occurrence of the carbon nanofiber with embedded Si nanoparticles during lithiation (adapted from [120]).

Other coating material, such as the SiO$_x$ coating, has been used to improve the cycle life of Si nanotube electrode to more than thousands of times with a high capacity since only inward expansion of Si is permitted and the electrolyte has no access to contact with Si to form solid electrolyte interface on the inner surface [119]. Theoretical models were established for both the spherical and cylindrical hollow Si electrode with coating by considering the insertion of lithium ions and the plastic flow [121]. Fracture of the shell may occur during lithiation since the tensile stress develops in the shell, while debonding may occur during delithiation due to the increased tensile radial stress at the interface.

Solutions were proposed to avoid the fracture of the shell and debonding at the core/shell interface by analyzing the stress field in the shell and at the interface. Such solution was also studied by *ab initio* calculations [122]. Through the simulation, it was found that the interfacial strength is decreased by only ~20%, indicating good adhesion at the Si/carbon interface.

In order to further improve the structural integrity of the carbon shell during lithiation, the yolk-shell carbon-coated Si nanoparticle electrode materials were synthesized [123-130]. The novel structure achieves long cycle life of more than 1000 cycles and high reversible capacity of ~1500 mA h g^{-1} with a cut-off voltage of 0.01 – 1.0 V *vs*. Li/Li^+ at the rate of C/10 for the first cycle, C/3 for the following 10 cycles and 1C for later cycles, as shown in Fig. 2.17a [123]. The improved performance owes to the free space between the Si core and the carbon shell to accommodate the volume change of the Si core. Besides, the carbon shell can prevent the formation of solid electrolyte interface on the surface of Si electrode. Fig. 2.17b shows the *in situ* lithiation process of several yolk-shell carbon-coated Si nanoparticles. The volume expansion of the Si core can be accommodated by enough space in the carbon shell and the carbon shell will not be fractured. By further controlling the yolk-shell structure, the capacity and cycle life can be improved.

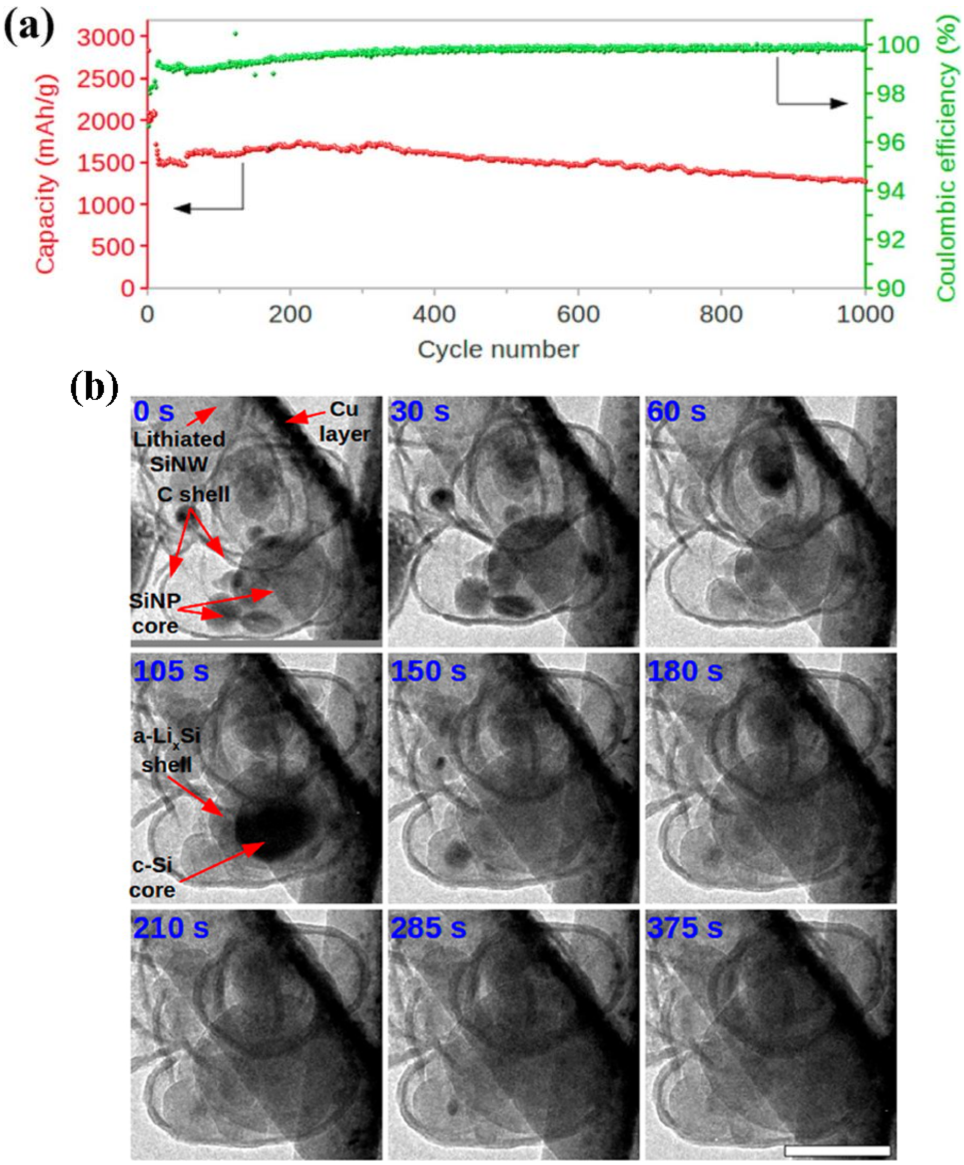

Figure 2.17. (a) Electrochemical cycling performance of the yolk-shell carbon-coated Si nanoparticle electrode material and (b) snapshots of the *in situ* lithiation process of the nanoparticles (adapted from [123]).

2.4. Other approaches to improve the electrochemical performance

In addition to the nanoscale design approaches and the coating techniques, several approaches have been utilized to improve the electrochemical performance of the electrode materials for lithium ion battery. One of the methods was to synthesize the SnO_2-based [4,131-135] or Si-based [136-140] compound or composite materials. In the long-run development of the tin-based oxide anode materials, Idota et al [4] synthesized the amorphous tin-based composite oxide material SnM_xO_y in 1997. The divalent Sn is the active center for lithiation and delithiation and M is typically mixed of glass-forming metallic elements such as boron, phosphorus and aluminum. The SnM_xO_y anode shows more stable electrochemical cycling performance than the pure SnO_2 anode. Yu et al [132] compared the electrochemical performance of four SnO_2-based anode materials: SnO_2, Li_2O-SnO_2, CuO-SnO_2 and Li_2O-CuO-SnO_2. A special multideck-cage porous structure of the materials was synthesized, as shown in Fig. 2.18a. The Li_2O-CuO-SnO_2 anode material shows a much better cycling performance than the other three anodes, as shown in Fig. 2.18b.

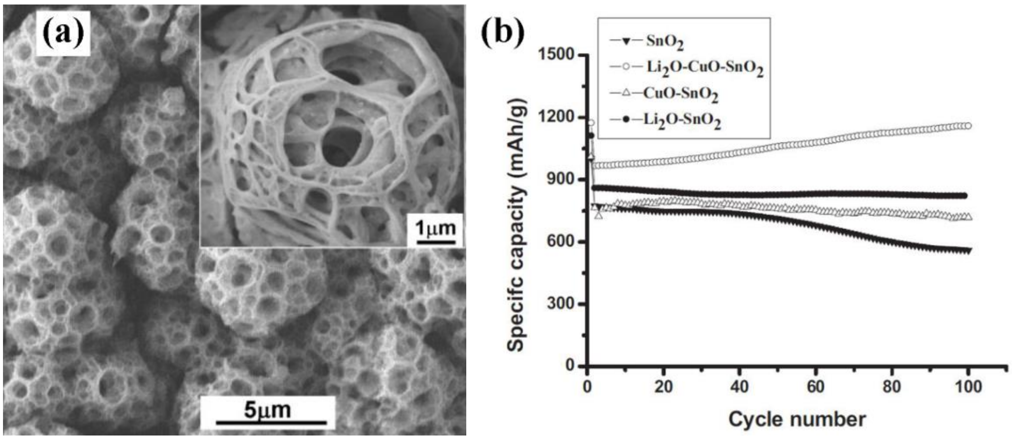

Figure 2.18. (a) SEM image showing the morphology of the as-prepared Li_2O-CuO-SnO_2 composite anode material and (b) electrochemical cycling performance of the SnO_2, Li_2O-SnO_2, CuO-SnO_2 and Li_2O-CuO-SnO_2 anode materials (adapted from [132]).

Apart from the design and improvement of the anode material itself, much work has been devoted to studying the effects of the other parts of lithium ion battery, such as binders [141-146], conductive additives [147,148] and current collectors

[149-154], etc. The binder should be electrochemically stable and negligibly soluble in the organic electrolyte and be able to increase the adhesion strength between electrode material and current collector. Besides, for high-capacity anode materials, such as SnO_2 and Si, the binder should be able to mitigate the large volume change during cycling. The conductive additives, such as the acetylene black or the reduced graphene oxide, can further improve the cycling performance by the enhanced electronic contact and the buffering function. Also, the conductive additives can be a better separation among the Si particles which increases the inter-particle resistance and decreases the possibility of aggregation.

It is also important to improve the adhesion and interfacial strength between the electrode materials and the current collector to overcome the large volume change-induced delamination and disintegration of the electrode materials. Therefore, the current collector has been modified to increase the adhesion and interfacial strength through different ways. The current collector with roughened or porous surface was proved to improve the cycling performance than those with flat surface [149-151]. The current collectors synthesized by cross-stacking continuous carbon nanotube films [152] showed improved mechanical stability and fast electron transfer at the interface between electrode and current collector, leading to better structural integrity and longer cycle life. In addition to the above advantages, the graphene [153] and nickel [154] foam current collectors even waived the use of conventional binders and conductive additives. The Cu nanofiber array current collectors showed improved electrochemical performance in several studies [155-160]. Figs. 2.19a and b show the morphology of the Cu nanofiber array current collector and the single nanofiber with Si shell and Cu core, respectively. Fig. 2.19c shows the improved cycling life to 1950 cycles and a reversible capacity of more than 1000 mA h g^{-1} with a cut-off voltage of 0.01 – 1.6 V *vs*. Li/Li^+ at the rate of 1.5C [160].

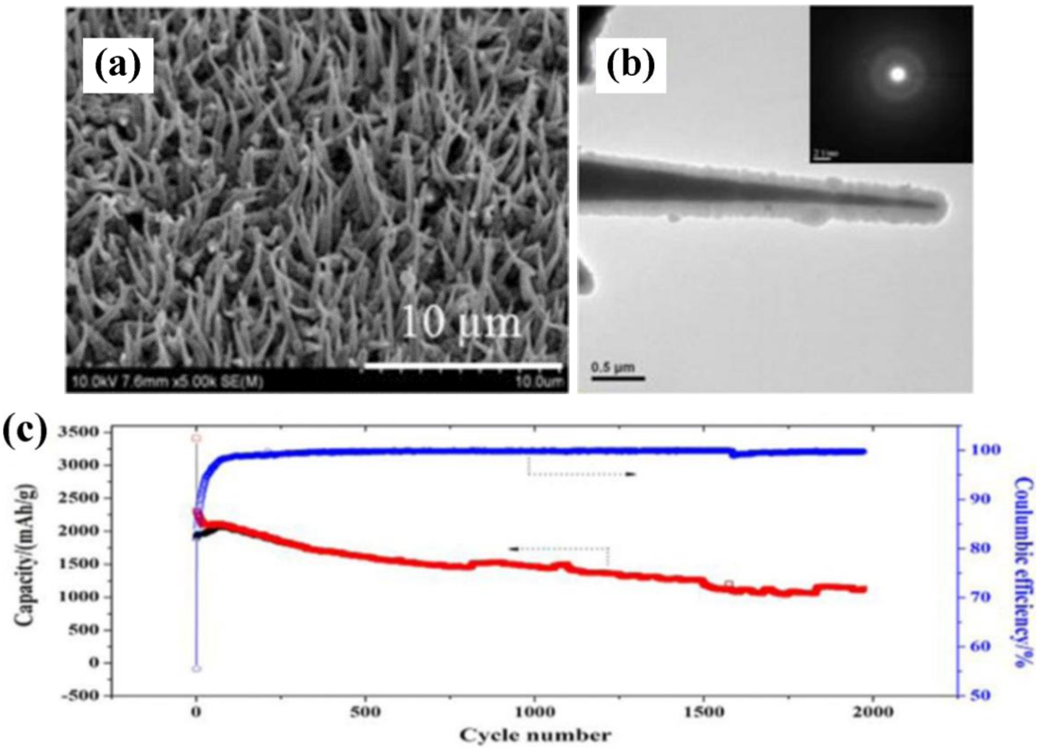

Figure 2.19. (a) SEM image showing the morphology of the Cu nanofiber array current collector. (b) TEM image showing the Si shell and the Cu core. Inserted is the electron diffraction pattern of the nanofiber. (c) Electrochemical cycling performance of the Si-coated Cu nanofiber array anode material (adapted from [160]).

2.5. Mechanics-based measurement and analysis

Many experimental studies on the mechanical properties of the high-capacity anode materials have been conducted. The *ex situ* experiments were conducted to measure the Young’s modulus and hardness of the Si and lithiated Si alloy by using nanoindentation in an anoxic environment [161]. It was found that the values are decreased with the degree of lithiation. This trend is similar to that of the *in situ* tensile tests on the Si and lithiated Si nanowires, as shown in Fig. 2.20 [162]. The *in situ* experimental results, as shown in Fig. 2.20f, give the value of Young's modulus of the lithiated Si which is around 2.4 – 12 GPa. Such modulus drop due to lithiation has also been reported in other studies [163-165]. The *in situ* tensile tests also revealed that the tensile strength is decreased from 3.6 GPa for pristine Si nanowires to 0.72 GPa for lithiated Si alloy, as shown in Fig. 2.20g. Besides, the tensile tests showed a permanent plastic deformation after the fracture of the lithiated Si nanowire.

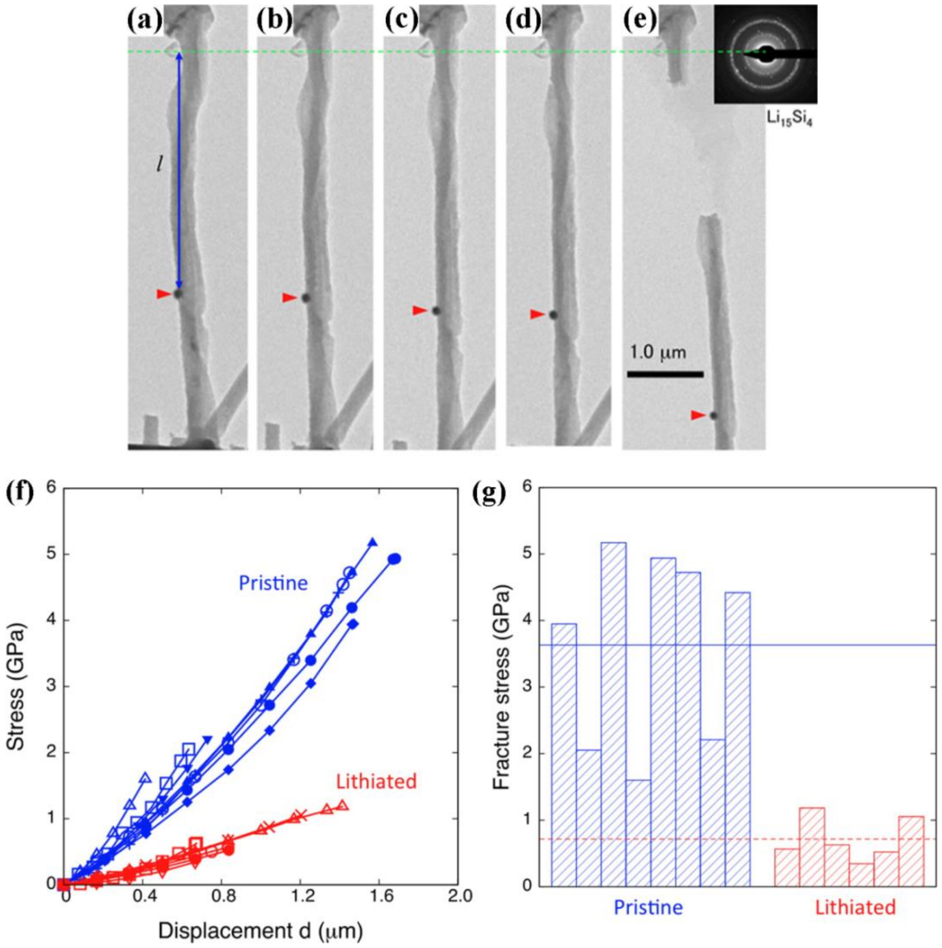

Figure 2.20. (a-e) Snapshots of the *in situ* tensile test of the lithiated Si nanowire. The length of the nanowire is measured by the green dashed line and the red arrowhead. Inserted is the electron diffraction pattern of the lithiated nanowire. (f) Stress-displacement curves of the pristine and lithiated nanowires obtained by *in situ* tensile test, of which the experimental data are denoted by the blue and red lines, respectively. (g) Fracture strength of the pristine and lithiated nanowires. The average values are indicated by the solid and dashed lines for the pristine and lithiated Si nanowires, respectively (adapted from [162]).

Numerical studies showed that Young's modulus, shear modulus and Poisson's ratio are decreased when lithium ion concentration is increased by using first-principle studies and quantum mechanical *ab initio* molecular dynamics calculations [162,166]. Such lithium ion concentration-dependent elastic properties are attributed to the increase of ionic Li-Si bonds which are weaker than the covalent Si-Si bonds. Therefore, the atoms in the lithiated Si alloy can move more freely than those in the crystalline Si so that the lithiated Si alloy can accommodate much higher plastic strain. This was confirmed by further *ab initio* MD simulation in which the lithium atoms diffuse 10 times faster in the amorphous phase than in the crystalline phase while the Si atoms are almost immobile in comparison to lithium atoms in both amorphous and crystalline phases [167]. The Li_xSn alloy shows the similar phenomenon of the lithium ion concentration-dependent elastic properties as Li_xSi alloy by using first-principle studies [168].

Different nanostructures of the Si/SnO_2 anode materials were studied through both experimental and theoretical methods. As mentioned above, the crystalline and amorphous Si nanoparticles have a critical diameter below which no fracture occurs during lithiation [101,102]. A nonlinear diffusion model was adopted to simulate the lithium ion concentration in the two-phase structure with a moving interface boundary. An elastic-perfectly-plastic model was used to describe the lithiation-induced deformation. Both of these two models were utilized into a finite element model to explain the arising of tensile stress in the surface layer of the crystalline Si nanoparticle during lithiation. A crack will be initiated due to the tension and propagate into the particle if the strain energy release rate, which is found to be dependent on particle size for given crack size, becomes higher than the resistance of surface energy, as shown in Fig. 2.21 [101]. Similar critical fracture size of diameter was found to be 240 – 360 nm for crystalline Si nanowires [47,91].

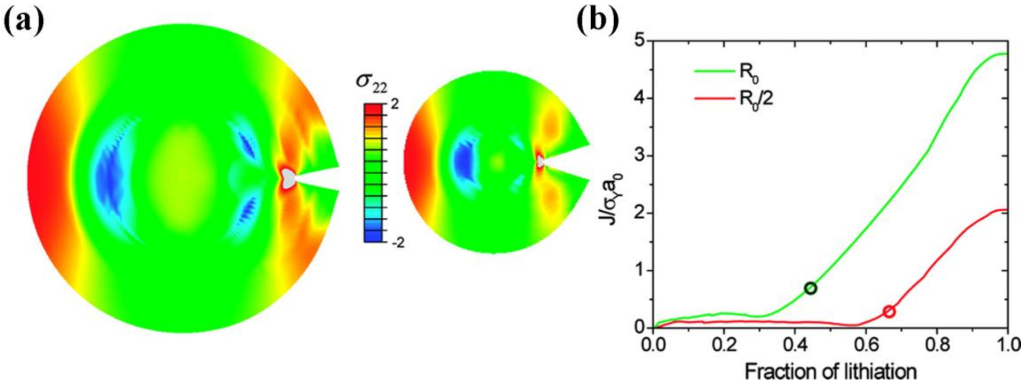

Figure 2.21. (a) The stress states in the simplified models of the nanoparticles which are assumed as wires with different radii of R_0 and $R_0/2$ but have same surface crack length of a_0 and yielding stress of σ_Y upon partial lithiation. (b) The energy release rates calculated by *J* integral as a function of fraction of lithiation, which is defined as the ratio of thickness of lithiated Si shell over the present radius of the wire. The green and red lines indicate the energy release rates of larger and smaller wires, respectively. The green and red circles represent the *J* integral at the lithiation state shown in (a) (adapted from [101]).

An elasto-plastic model coupled with a nonlinear diffusivity equation was used to simulate the diffusion of lithium ions in the crystalline Si nanowire by using the finite element simulation approach. In order to capture the anisotropic expansion, anisotropic lithiation-induced strain and orientation-dependent kinetics of reaction front were adopted. The cross-section becomes a dumbbell shape after lithiation and based on the simulation results, the tensile stress occurs near the surface indent while the compressive stress occurs in the Si core, as shown in Fig. 2.22. Due to diminishment of the compressive stress upon further lithiation, the indent will propagate into the Si core, leading to the crack of the nanowire [47]. The normalized lithium ion concentration *c* is defined as the actual lithium ion concentration normalized by the lithium ion concentration at full lithiation state ($Li_{3.75}Si$).

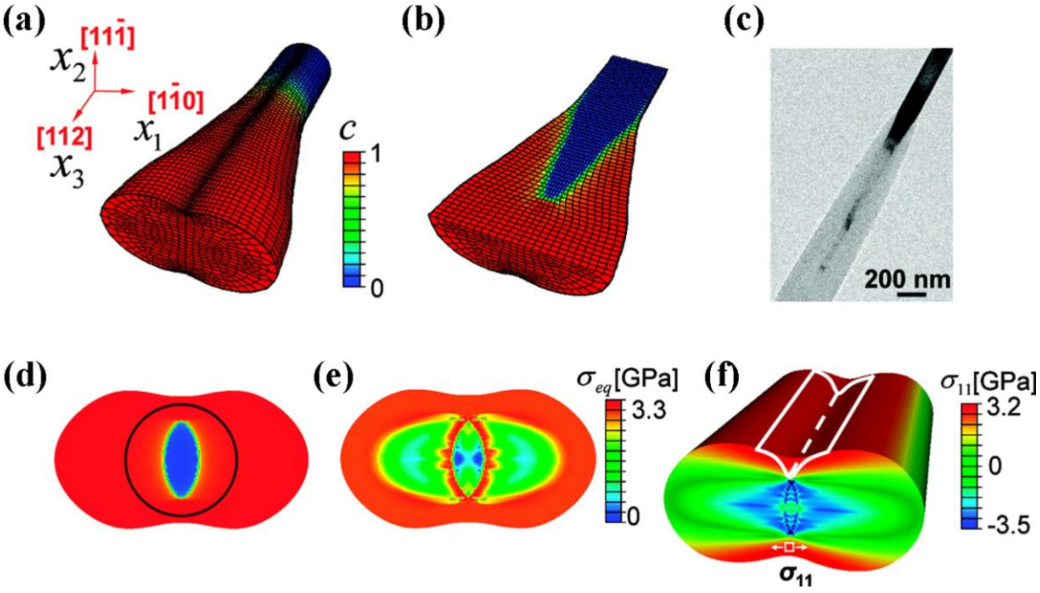

Figure 2.22. (a) 3-D simulation model and (b) $(11\bar{1})$ cross-sectional view of the model showing normalized lithium ion concentration, c, in the partially lithiated $[112]$-oriented Si nanowire, which is consistent with lithiation state as shown in the TEM image (c). (112) cross-sectional view of (d) the lithium ion concentration and (e) the distribution of von Mises stress with $\sigma_{\mathrm{eq}} = (3\sigma_{ij}\sigma_{ij}/2)^{1/2}$. The original cross section of the Si nanowire is marked by the black circle in (d). (f) Stress distribution in the 3-D model, indicating the neck growth with tensile stress near the surface indent and compressive stress in the center at $x_1 = 0$ (adapted from [47]).

Si thin film has also been utilized as the electrode and showed high initial capacity and stable cycle life for 30 times [52,71]. There is a critical size (~7 μm), under which no delamination occurs for the Si thin film electrode [169,170]. Theoretical models based on fracture mechanics and theory of diffusion were established to analyze the stress states and deduce the critical size for nucleation and growth of edge and center interfacial cracks by plain strain and axisymmetric analysis. In addition to the size of the Si thin film, it was found that there exists a critical thickness below which the amorphous Si thin film will not be fractured during lithiation [171]. With the decreasing of the thickness, the islands separated by the cracks become smaller during electrochemical cycling tests. A modified spring-block model was utilized to explain the existence of critical thickness and size. The fracture of the Si thin film was found to occur during delithiation [172]. Finite element simulation, accounting for the pressure gradients, finite strains and plastic flow, was carried out. It was found that cracks first initiate in the high tension zone near the film edge due to the lithiation-induced bending of the thin film during the early stage of lithiation, leading to the sequential formation of the new free surfaces and the fracture of the whole film [173]. The fracture energy of the lithiated Si was calculated by measuring and analyzing the stress states at the moment of crack initiation based on fracture mechanics [174].

In this chapter, the electrochemical performance and improvement methods were reviewed and summarized for different kinds of nanoscale SnO_2 and Si electrode materials. The lithiation/delithiation and failure mechanisms of the electrode materials were studied through *in situ* lithiation/delithiation techniques. The design of core-shell structure was adopted to improve the performance by constraining the volume change, preventing the fracture of solid electrolyte interface and increasing the electronic and ionic conductivities. Other approaches, such as the modification of binders, conductive additives and current collectors, were also discussed. The mechanical properties and fracture mechanisms of several electrode materials were studied by reviewing the related mechanics-based experimental and theoretical works. Based on the above analysis, further studies of the core-shell nanostructured electrode materials will be conducted by both experimental and theoretical approaches in this thesis.

Chapter 3. Research methods

3.1. Experimental

3.1.1. Chemical synthesis

a. *Synthesis of amorphous carbon shell*

The carbon shell was synthesized by hydrothermal method [125]. 100 mg commercial Si nanoparticles were dissolved in a solution consisted of 600 mg sucrose (carbon source), 0.6 mL concentrated hydrochloric acid (37 wt%), 6 mL deionized water and 8 mL absolute ethanol (99.9 wt%) under stirring and ultrasonic processing for 120 mins. The solution was then stirred at 70 ˚C for 3 hours and dried in the vacuum oven at 120 ˚C for 8 hours. The dried sample was manually ground and loaded in an alumina crucible which was later moved into the furnace and heated at 800 ˚C for 2 hours in the atmosphere of nitrogen. After cooling down, the carbon-coated Si nanoparticles were synthesized.

b. *Synthesis of crystalline copper nanowires*

The Cu nanowires were synthesized by hydrothermal method [175]. Concentrated NaOH solution was obtained by dissolving 120 g NaOH in 200 mL deionized water. After cooling down, 10 mL 0.1 M $Cu(NO_3)_2$ solution was dropped into the NaOH solution. The mixture was then moved onto a hot plate in a fume hood and added by 3 mL Ethylenediamine (EDA) and 0.25 mL N_2H_4 (35 wt%). The solution was heated at 80 ˚C for 1 hour. The reactant was centrifugally cleaned for 3 times by 3 wt% N_2H_4 solution to eliminate the impurities and then the Cu nanowires were collected.

c. *Sputtering of amorphous silicon shell*

The Si shell was synthesized by magnetron sputtering technique [155,160,171,176]. The Cu nanowires were centrifugally cleaned for 3 times by absolute ethanol and then dispersed on the glass substrate. The nanowires were dried at 40 ˚C for 40 min and then moved into the magnetron sputtering machine. After setting the program parameters, including the source power (200 W), temperature (100 ˚C), time period (40 mins) and atmosphere (pure Ar), and starting the program, the amorphous silicon shell could be sputtered on the copper nanowires by the silicon target.

3.1.2. Materials characterization

The morphology of the electrode materials was firstly examined by Scanning Electron Microscopy (SEM). The further observation of the morphology and crystalline structure of the electrode materials was conducted by using Transmission Electron Microscopy (TEM). The chemical components were confirmed by the electron diffraction pattern (EDP) and energy-dispersive X-ray spectroscopies (EDX) affixed to the SEM or TEM.

3.1.3. *In situ* lithiation and delithiation

In situ TEM is a useful technique in observing the nano- and micro-structural change during lithiation and delithiation. Generally, the nanobattery setup inside

TEM contains an anode material, liquid or solid electrolyte and lithium source, such as a lithium metal reference electrode or a $LiCoO_2$ cathode, as shown in Fig. 2.4. After a voltage is applied, the lithium ions diffuse from the lithium source to the anode through the electrolyte and the anode material will be lithiated. During delithiation, the lithium ions are extracted from the anode material and combine with the electrons passing through the outer circuit at the cathode. During lithiation and delithiation, the changes of volume, shape, structure and chemical components can be observed.

Generally, the nanobatteries can be divided into two groups by the electrolyte, which are called liquid electrochemical cell and solid electrochemical cell, respectively. One end of the anode material is immersed in the liquid electrolyte of the liquid cell or contacts with the solid electrolyte of the solid cell. The “flooding geometry”, which is always used in the real battery where the electrodes are fully immersed in the electrolyte, can be realized in a nanobattery [43]. In our *in situ* experiments, the solid electrochemical cell was normally used for lithiation and delithiation. The lithium metal was adopted as reference electrode which was attached on the tungsten rod in the glove box and then transferred to the Nanofractory® holder. During the transferring, the surface of the lithium metal was unavoidably oxidized to Li_2O which served as the solid electrolyte. The anode material was attached on the other golden rod by silver paste and fixed on the holder. Then the holder was moved into the TEM. When the vacuum requirement was satisfied, the anode material could be lithiated by applying a voltage and moving the lithium metal to contact with the anode material.

3.2. Theoretical

3.2.1. Diffusion equations

a. *Fick's first law of diffusion*

In an inhomogeneous annealed single-phase object, matter will flow from the region of high concentration to the region of low concentration in order to decrease the concentration gradient. If the annealing time is long enough, the net flow will not stop until the object becomes homogeneous. In a steady state, where the total quantities of the various matters inside the object remain unchanged with time, Fick's first law is used to calculate the diffusion flux J in a two dimensional case by [177]

$$J = -D\left[\frac{\partial c}{\partial x}\right]_t \tag{3.1}$$

where D is the diffusion coefficient. Here, D can be regarded as the ratio of diffusion flux over the concentration gradient with dimension of area per unit time and is independent of the concentration magnitude as confirmed by experiments. Eq. (3.1) is valid in both steady and non-steady states no matter whether the concentration or concentration gradient at the specific position is changing with time or not. If other potential gradients also affect the diffusion flux, such terms should be added into the above diffusion equation, which will be discussed in Section 3.2.1.c.

b. *Fick's second law of diffusion*

If the total quantities of the matter and the concentration at specific positions are changing with time in the object; that is, if the steady state no longer exists, Eq. (3.1) can still be valid but it is not convenient form to be used. Therefore, it is necessary to get the useful diffusion equation by a second differential calculation. Suppose a flux moves from one end of a bar with unit cross section to the other end. For an element with thickness Δx, the ingoing flux J_1 can be expressed by the outgoing flux J_2 as

$$J_1 = J_2 - \Delta x(\partial J / \partial x) \tag{3.2}$$

Since $J_1 \neq J_2$, the concentration is changing with time in the element. According to the conservation of matter, the net increase of matter in the element with volume of $1 \cdot \Delta x$ can be expressed as

$$J_1 - J_2 = \Delta x(\partial c / \partial t) \tag{3.3}$$

Combination of Eqs. (3.2) and (3.3) leads to

$$\frac{\partial c}{\partial t} = -\frac{\partial J}{\partial x} \tag{3.4}$$

Substituting Eq. (3.1) into Eq. (3.4) gives the Fick's second law of diffusion as

$$\frac{\partial c}{\partial t} = \frac{\partial}{\partial x}\left(D\frac{\partial c}{\partial x}\right) \tag{3.5}$$

For steady state with constant *D*, Eq. (3.5) can also be applied when $\frac{\partial c}{\partial t} = 0$.

That is, $D\frac{\partial^2 c}{\partial x^2} = 0$, for Cartesian coordinates. The solution of this equation has a lot of application in physics and engineering, such as heat flow [178] and potential theory [179]. For non-steady state, if *D* is constant in different position, Eq. (3.5) becomes

$$\frac{\partial c}{\partial t} = D\frac{\partial^2 c}{\partial x^2} \tag{3.6}$$

In Cartesian coordinates, by solving Eq. (3.6), we can know the concentration $c(x,t)$ of the matter in the object at any specific time and position. Generally, the solution of Eq. (3.6) is dependent on the comparison of the diffusion distance to the initial geometrical dimension. If the diffusion distance is relatively small, the solution can be termed as error functions. If the homogeneity of the object is approached, the solution can be expressed by the first few terms of the infinite trigonometric series. Transforming Eq. (3.6) into three dimensions with a vector notation leads to a generalized form as

$$\frac{\partial c}{\partial t} = -\nabla J \tag{3.7}$$

c. *Stress-assisted diffusion*

A potential gradient can drive the motion of the atoms from one side to the other in a bar. This potential gradient, in addition to the concentration gradient, determines the total flux of the matter in the object. The Fick’s first law is no longer available since extra matter is introduced into the object by the potential gradient. Suppose a particle is driven by a potential gradient in a potential field of $V(x,y,z)$. The force *F* produced by the potential gradient can be given as

$$F = -\nabla V \tag{3.8}$$

The force F empirically generates a diffusion velocity for the atoms in the object, which is mathematically expressed as

$$v = MF \tag{3.9}$$

where M is the mobility with a unit of velocity per force. It should be noted that in the atomic scale, an atom is not accelerated in the way like a free particle since the moving direction of the atom is always changing. Therefore the force F is considered to provide a steady-state velocity rather than acceleration. Due to the similarity of the driving forces between potential gradient and concentration gradient, the mobility M can be proportional to the diffusion coefficient D, which is

$$M = D / kT \tag{3.10}$$

where k is the Boltzmann's constant and T is the absolute temperature in Kelvin. The diffusion flux induced by the potential gradient can be the product of the number of atoms per unit volume and the velocity of the atoms, as

$$J = cv = -(Dc / kT)\nabla V \tag{3.11}$$

The total flux is the summation of the diffusion flux by the concentration gradient and the potential gradient. Therefore, the flux equation can be the summation of Eqs. (3.1) and (3.11) as

$$J = -D(\nabla c + c\nabla V / kT) \tag{3.12}$$

For constant D, applying Eq. (3.12) into Eq. (3.7) gives

$$\frac{\partial c}{\partial t} = D\nabla\left(\nabla c + \frac{c\nabla V}{kT}\right) \tag{3.13}$$

By solving the above equation, the concentration $c(x, y, z, t)$ can be calculated in the object in the presence of both potential gradient and concentration gradient.

3.2.2. Fracture mechanics

a. *Failure criteria*

Failure criterion can be applied to predict the failure of material upon the occurrence of plastic deformation [180]. For instance, the plastic flow occurs when the uniaxial stress-strain curve deviates from its original linear range for uniaxial stress state. Due to the complex stress states in different cases, several failure criteria are developed to predict the failure of the materials.

The maximum-stress criterion, also known as Rankine criterion, indicates that failure, or plastic flow, occurs when the maximum principal stress upon a complex stress state becomes higher than the flow stress in uniaxial tension. If $\sigma_1 > \sigma_2 > \sigma_3$, we get

$$\sigma_1 > \sigma_0(\text{tension}) \tag{3.14}$$

where σ_0 is the flow stress of the material. That is, if the material is under tension, the maximum principal stress should not be higher than the maximum tensile stress of the material otherwise failure occurs. It should be noted that the hydrostatic stress does not contribute to the plastic flow.

The maximum-shear-stress criterion, also known as Tresca criterion, is applied to predict the failure of the material when the maximum shear stress in a complex stress state is higher than the maximum tensile or compressive shear stress in the uniaxial direction. The maximum shear stress is calculated as

$$\tau_{\max} = \frac{\sigma_1 - \sigma_3}{2} \tag{3.15}$$

This criterion is applicable for the hydrostatic stress since no shear stress is contributed by the hydrostatic stress. Another failure criterion, called maximum-distortion-energy criterion or von Mises criterion, predicts the failure of material according to the critical distortional or shear component of the deformation energy of a deformed body. The criterion is expressed as

$$\frac{\sqrt{2}}{2}\left[(\sigma_1 - \sigma_2)^2 + (\sigma_2 - \sigma_3)^2 + (\sigma_1 - \sigma_3)^2\right]^{1/2} > \sigma_0 \tag{3.16}$$

The material will fail in a complex stress state if the distortional or shear deformation energy is higher than that in uniaxial stress, such as the uniaxial tension or compression. This criterion is called J_2, which is the second invariant of the stress deviator and given by

$$J_2 = \frac{1}{G}\left[(\sigma_1 - \sigma_2)^2 + (\sigma_2 - \sigma_3)^2 + (\sigma_1 - \sigma_3)^2\right] \tag{3.17}$$

where *G* is shear modulus of the material.

b. *Linear elastic fracture mechanics*

The criteria in the above section predict the failure of the materials based on the comparison of the applied stress and the flow properties of the materials. The fracture mechanics approaches depend on three factors: the applied stress, the fracture toughness and the flaw size [181]. Both the stress-intensity approach and the energy criterion can be applied to predict the crack growth based on the linear elastic fracture mechanics (LEFM).

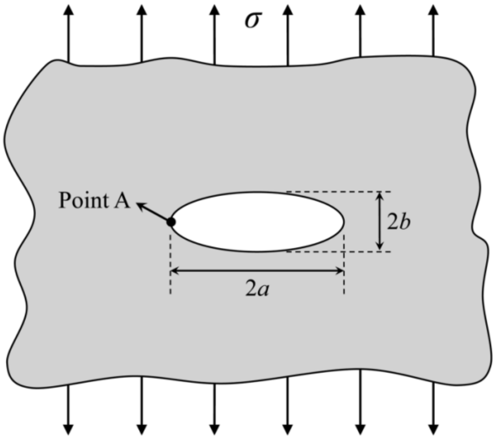

Figure 3.1. An infinite plate with an elliptical through-thickness hole subject to a remote stress.

Consider an infinite plate which is subject to a remote tensile stress σ, as shown in Fig. 3.1. The elliptical hole has length of 2*a* and width of 2*b*. The length and width of the plate are much larger than 2a and 2b, respectively. The stress at the tip (Point A) of the crack is given by

$$\sigma_{\mathrm{A}} = \sigma\left(1 + \frac{2a}{b}\right) \tag{3.18}$$

The ratio of $\sigma_{\mathrm{A}} / \sigma$ is named as the stress concentration factor k_t. If the geometrical dimensions satisfy $a = b$, the hole will be a circle and $k_t = 3.0$, which is a well-known result for circular hole in an infinite plate subject to a remote stress. It can be noted that if $a >> b$, corresponding to an infinite sharp crack, the stress at the crack tip σ_{A} can be infinite large upon which no material can sustain. The crack will definitely grow, leading to the fracture of the material. Such a sharp crack with a high stress is a mathematical abstraction. To better explain the failure of the material, the stress distribution at the crack tip of the linear elastic material can be calculated by the stress-intensity factor K_I. If the material is assumed to be fractured at some combination of stress and strain, such stress and strain condition corresponds to a critical stress-intensity factor K_{Ic}. The stress-intensity factor K_I (mode I) at the tip of the crack can be expressed as

$$K_I = \sigma\sqrt{\pi a} \tag{3.19}$$

Failure of the material occurs at $K_I = K_{Ic}$, where K_I is the driving force for the crack and K_{Ic} is the size-independent toughness of the material. Therefore, by calculating the stress-intensity factor, the failure of the elastic material can be predicted.

In addition, the energy criterion is developed as an approach to predict the crack propagation for elastic material, stating that the crack growth occurs when the energy for creating new crack surface becomes higher than the fracture energy of the material. The fracture energy includes the surface energy, plastic work or any other type of energy dissipation associated with the crack growth. In linear elastic materials, the energy release rate G, which is defined as the energy required for creating new crack surface of unit area, is used to determine whether the crack will grow or not by comparing with the size- and geometry-independent fracture toughness of the materials G_c. For an infinite plate subject to a remote tension, the energy release rate at the crack tip in Fig. 3.1 is

$$G = \frac{\pi\sigma^2 a}{E} \tag{3.20}$$

where E is the Young’s modulus of the material. By comparing Eqs. (3.19) and (3.20), it can be found that the relationship between the stress-intensity factor and the energy release rate in the linear elastic material is

$$G = \frac{K_I^2}{E} \tag{3.21}$$

Eq. (3.21) indicates that for the linear elastic materials, the stress-intensity and energy approaches are essentially equivalent.

c. *Elastic-plastic fracture mechanics*

The above linear elastic fracture mechanics is only applicable to the crack provided the plastic zone is limited within a small area around the tip of crack. When it comes to the elastic-plastic or nonlinear elastic materials, two important fracture mechanics parameters are applied: the crack-tip-opening displacement (CTOD) and the J contour integral. Both of the two parameters describe the crack-tip conditions in the elastic-plastic materials and provide size-dependent results of the fracture toughness.

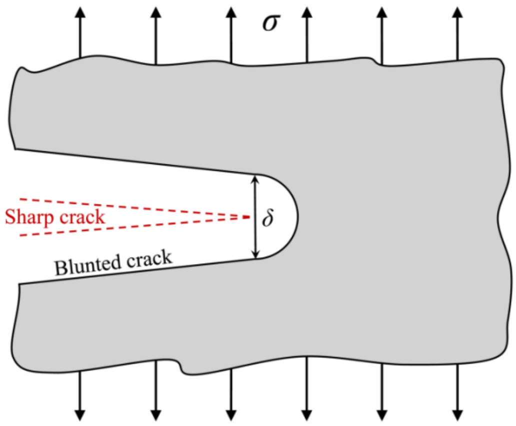

Figure 3.2. Schematic of the crack-tip-opening displacement δ.

The CTOD approach measures the opening of the crack due to the high toughness of the elastic-plastic materials, as shown in Fig. 3.2. The initial sharp crack is blunted with a finite displacement δ around the crack tip by the plastic deformation. For the cases of the small-scale yielding, the crack is assumed to be elongated by the crack-tip plasticity. The CTOD δ is given by [182]

$$\delta = \frac{4}{\pi}\frac{K_I^2}{\sigma_{YS} E} \tag{3.22}$$

where σ_{YS} is the yielding stress of the material and plane stress condition prevails. The CTOD can also be analyzed by the crack-opening displacement in the back region of the strip-yield zone in the strip-yield model, which shows slightly different result from Eq. (3.22) as [183]

$$\delta = \frac{K_I^2}{\sigma_{YS} E} \tag{3.23}$$

The above equation is applied for plane stress condition of non-hardening material. A more general form of the relationship between δ and K_I can be expressed as

$$\delta = \frac{K_I^2}{m\sigma_{YS}E^{'}} \tag{3.24}$$

where m is a dimensionless parameter, with $m \approx 1.0$ and $E^{'} = E$ for plane stress condition and $m \approx 2.0$ and $E^{'} = \frac{E}{1-v^2}$ for plane strain condition.

The loading curves are the same for the nonlinear elastic material and elastic-plastic material. The nonlinear elastic material can recover to its original state along the same path as the loading curve, while the elastic-plastic material unloads through a linear curve with the slope equal to the Young's modulus. The identical loading curves of the materials imply the same material response for both materials so that the material behavior of the elastic-plastic materials can be effectively regarded as the nonlinear elastic materials during the loading process as long as no unloading occurs. That is, the deformation theory of plasticity can be equivalently applied to analyze the cracking problem of nonlinear elasticity during loading.

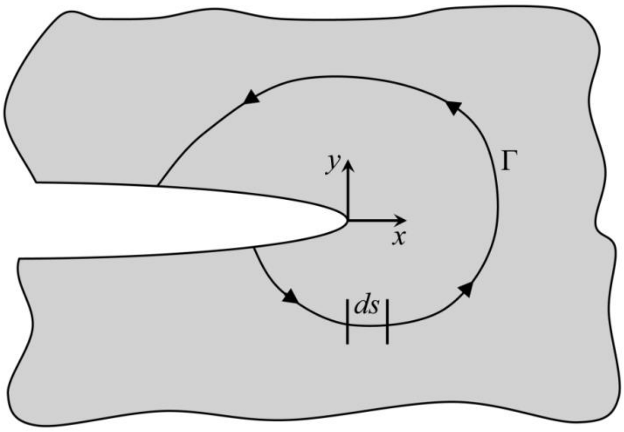

Figure 3.3. An arbitrary integral contour around a crack tip.

Rice [184] applied deformation plasticity (or equivalent nonlinear elasticity) and found a path-independent contour integral to characterize the energy release rate in the nonlinear material, which is called *J* integral. As shown in Fig. 3.3, the *J* integral of an arbitrary counterclockwise path (Γ) around a crack tip is given by

$$J = \int_{\Gamma} \left(w dy - T_i \frac{\partial u_i}{\partial x} ds \right) \tag{3.25}$$

where *w* is strain energy density, T_i represents the components of the traction vector, u_i denotes the displacement vector components and *ds* is the length increment along the path Γ. The strain energy density *w* is denoted as

$$w = \int_0^{\varepsilon_{ij}} \sigma_{ij} d\varepsilon_{ij} \tag{3.26}$$

where σ_{ij} and ε_{ij} are the stress and strain tensors, respectively. The traction represents the stress vector at a specific point on the contour and defines the stress acting on the boundary. The components of the traction vector T_i are given by

$$T_i = \sigma_{ij} n_j \tag{3.27}$$

where n_j are the components of unit vector normal to Γ. In addition to an indicator of an energy parameter, the *J* integral can be used as a stress intensity parameter and applied to characterize the stress and strain conditions at the tip of crack in the nonlinear elastic material [185,186]. A power-law relationship of the plastic stress and strain is adopted and the relationship between stress and strain for uniaxial deformation with both elastic and plastic strains is given by

$$\frac{\varepsilon}{\varepsilon_{\mathrm{YS}}} = \frac{\sigma}{\sigma_{\mathrm{YS}}} + \alpha\left(\frac{\sigma}{\sigma_{\mathrm{YS}}}\right)^n \tag{3.28}$$

where σ_{YS} is the reference stress which is usually equal to the yield stress, $\varepsilon_{\mathrm{YS}}$ is the reference strain taken as σ_{YS}/E, α is the dimensionless constant and n is the strain-hardening exponent. Eq. (3.28) is known as Ramberg-Osgood equation which is normally used for fitting of stress-strain curve. The stress and strain must vary as 1/*r* near the crack tip so that the *J* integral can be path-independent. In addition, the elastic strains within the plastic zone, in comparison to the plastic strains, can be negligible. These two conditions lead to a simple power-law relationship of the stress and strain near the crack tip as

$$\sigma_{ij} = k_1\left(\frac{J}{r}\right)^{\frac{1}{n+1}} \tag{3.29a}$$

$$\varepsilon_{ij} = k_2\left(\frac{J}{r}\right)^{\frac{n}{n+1}} \tag{3.29b}$$

where k_1 and k_2 are the proportionality constants. By applying certain boundary conditions, the actual stress and strain states can be calculated as

$$\sigma_{ij} = \sigma_{\mathrm{YS}} \left(\frac{EJ}{\alpha \sigma_{\mathrm{YS}}^2 I_n r} \right)^{\frac{1}{n+1}} \tilde{\sigma}_{ij}(n, \theta) \tag{3.30a}$$

$$\varepsilon_{ij} = \frac{\alpha \sigma_{\mathrm{YS}}}{E} \left(\frac{EJ}{\alpha \sigma_{\mathrm{YS}}^2 I_n r} \right)^{\frac{1}{n+1}} \tilde{\varepsilon}_{ij}(n, \theta) \tag{3.30b}$$

where I_n is a *n*-dependent integration constant and $\tilde{\sigma}_{ij}$ and $\tilde{\varepsilon}_{ij}$ are the dimensionless functions of n and θ. These parameters are additionally dependent on the stress states, such as plane stress or plane strain. Eqs. (3.30) are called HRR singularity, which is defined by *J* integral. This HRR singularity works just as the stress intensity factor indicates the singularity of the stress states near the tip of crack in the linear elastic material. In order to capture the singularity of the stress and strain near the tip of crack, $n = 1$, corresponding to a $1/\sqrt{r}$ singularity, is adopted for linear elastic material, while a $r^{-1/(n+1)}$ singularity is adopted for elastic-plastic material. For perfect plastic material, $n = 0$, corresponding to a $1/r$ singularity, is used.

3.2.3. Finite element simulation

In some cases, analytical solutions of the stress and strain can be obtained for a body subject to external loads or displacements. For example, in Chapter 6, the stress states can be calculated in the carbon shell of the yolk-shell carbon-coated Si nanoparticle upon full lithiation based on the theory of elasticity and fracture mechanics. The detailed derivation will be discussed in Section 6.2. However, relatively few scientific and engineering problems have closed-form analytical solutions to derive the stress and strain. For most solid mechanics problems especially when it comes to the fields of plasticity and fracture mechanics with a lot of nonlinear factors, computational approaches, such as finite element (FE) simulation [187], finite difference method [188] and boundary integral equations [189], are used to give the numerical solutions. For example, the domain integral approach, which is implemented by FE simulation (also used for most analyses of cracked bodies), can give the value of energy release rate by J integral or crack-tip-opening displacement around the tip of crack. Here, we focus on the finite element method and its application in calculation of J integral.

a. *Basics of finite element method*

In the finite element method, the object of interest is divided into a lot of discrete parts which are called elements. The commonly used element types are the 1-D beams, the 2-D plane stress or plane strain elements and the 3-D tetrahedrons or bricks. Such elements are connected by nodes on which the displacement fields are continual among neighboring elements. The external displacements or loads are applied on these nodes. Fig. 3.4 shows a representative 8-node isoparametric continuum element for two-dimensional problem within local and global coordinate axes.

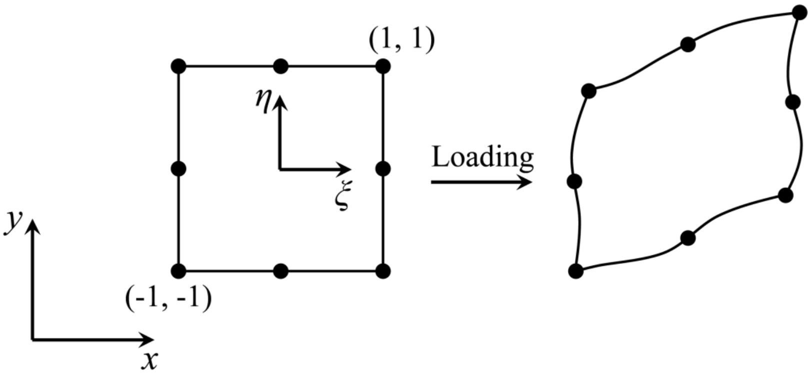

Figure 3.4. Deformation of a 2-D 8-node element upon loading.

The local coordinate system varies from –1 to +1 within the element area, as shown in Fig. 3.4. This coordinate system is also known as the parametric coordinate system. The nodal points are $(-1,-1)$ at the lower left-hand corner and $(1,1)$ at the upper right-hand corner. The global coordinates of a point (ξ,η) inside the element can be expressed as

$$x = \sum_{i=1}^{n} N_i(\xi,\eta)x_i \tag{3.31a}$$

$$y = \sum_{i=1}^{n} N_i(\xi,\eta)y_i \tag{3.31b}$$

where n is the number of nodes in the element, N_i are the shape functions of the node i with local coordinate of (ξ_i,η_i) and global coordinate of (x_i,y_i). The shape functions are polynomials which are used to interpolate the field quantities inside the element. The functions are linear for the elements that contain only 4 nodes at each corner and quadratic for four-sided and eight-node elements. The displacements within the element can be expressed by interpolation as

$$u = \sum_{i=1}^{n} N_i(\xi,\eta) u_i \tag{3.32a}$$

$$v = \sum_{i=1}^{n} N_i(\xi,\eta) v_i \tag{3.32b}$$

where (u_i, v_i) is the displacements of the nodes in the global coordinates. The strain at (x, y) within the element can be determined by

$$\begin{Bmatrix} \varepsilon_x \\ \varepsilon_y \\ \gamma_{xy} \end{Bmatrix} = [\mathrm{B}] \begin{Bmatrix} u_i \\ v_i \end{Bmatrix} \tag{3.33}$$

where

$$[\mathrm{B}] = \begin{bmatrix} \dfrac{\partial N_i}{\partial x} & 0 \\ 0 & \dfrac{\partial N_i}{\partial y} \\ \dfrac{\partial N_i}{\partial y} & \dfrac{\partial N_i}{\partial x} \end{bmatrix} \tag{3.34}$$

and

$$\begin{Bmatrix} \dfrac{\partial N_i}{\partial x} \\ \dfrac{\partial N_i}{\partial y} \end{Bmatrix} = [\mathrm{J}]^{-1} \begin{Bmatrix} \dfrac{\partial N_i}{\partial \xi} \\ \dfrac{\partial N_i}{\partial \eta} \end{Bmatrix} \tag{3.35}$$

where [J] is the Jacobian matrix and given by

$$[\mathrm{J}] = \begin{Bmatrix} \dfrac{\partial x}{\partial \xi} & \dfrac{\partial y}{\partial \xi} \\ \dfrac{\partial x}{\partial \eta} & \dfrac{\partial y}{\partial \eta} \end{Bmatrix} = \begin{Bmatrix} \cdots \dfrac{\partial N_i}{\partial x} \cdots \\ \cdots \dfrac{\partial N_i}{\partial y} \cdots \end{Bmatrix} \begin{Bmatrix} \vdots \; \vdots \\ x_i y_i \\ \vdots \; \vdots \end{Bmatrix} \tag{3.36}$$

The stress matrix can be calculated as

$$\{\sigma\} = [\mathrm{D}]\{\varepsilon\} \tag{3.37}$$

where $[\mathrm{D}]$ is the stress-strain constitutive matrix. Regarding to the problems of incremental plasticity, the stress and strain should be calculated incrementally with an updated $[\mathrm{D}]$ by

$$\{\Delta\sigma\} = [\mathrm{D}(\varepsilon,\sigma)]\{\Delta\varepsilon\} \tag{3.38}$$

The stress and strain states in the body can thus be calculated by the nodal displacements or loads and the constitutive law at certain Gauss points or integration points. The displacements of the nodes can be calculated by adopting the nodal forces and element stiffness. The elemental stiffness matrix is derived from the principle of minimum potential energy [187] as

$$[k] = \int_{-1}^{1}\int_{-1}^{1}[\mathrm{B}]^{T}[\mathrm{D}][\mathrm{B}]\det|\mathrm{J}|\,d\xi d\eta \tag{3.39}$$

where superscript *T* represents the matrix's transpose. The global stiffness matrix $[\kappa]$ is assembled from Eq. (3.39), having the relationship with global force and displacement as

$$[\kappa][\mathrm{u}] = [\mathrm{F}] \tag{3.40}$$

b. *The energy domain integral*

The *J* integral has been widely used to evaluate the energy release rate of a crack for both linear and nonlinear problems. According to Section 3.2.2.c, a generalized *J* integral around the crack tip, accounting for inelastic material behavior and effect of inertia, is given by

$$J = \lim_{\Gamma_0 \to 0} \int_{\Gamma_0} \left[(w + T)\delta_{1i} - \sigma_{ij} \frac{\partial u_j}{\partial x_1} \right] n_i d\Gamma \tag{3.41}$$

where T is the kinetic energy density and w is the stress work which includes various material behaviors. Eq. (3.41) applies only when the contour surrounding the crack tip is extremely small. For quasistatic conditions ($T = 0$), the total strain of an elastic-plastic material under additional thermal loading is given by

$$\varepsilon_{ij}^{total} = \varepsilon_{ij}^{e} + \varepsilon_{ij}^{p} + \alpha\Theta\delta_{ij} = \varepsilon_{ij}^{m} + \varepsilon_{kk}^{t} \tag{3.42}$$

where α is the coefficient of thermal expansion, Θ is the temperature change and ε_{ij}^{e}, ε_{ij}^{p}, ε_{ij}^{m} and ε_{kk}^{t} are the elastic, plastic, mechanical and thermal strains with $\varepsilon_{ij}^{m} = \varepsilon_{ij}^{e} + \varepsilon_{ij}^{p}$. The stress work can be expressed as

$$w = \int_0^{\varepsilon_{kl}^{m}} \sigma_{ij} d\varepsilon_{ij}^{m} \tag{3.43}$$

Due to the singularity of the stress and strain around the crack tip, it is always difficult to get the numerical solution of Eq. (3.43). Therefore, the energy domain integral approach was developed to numerically calculate the *J* integral [190,191]. Fig. 3.5 shows the domain contour integral for a 2-D case with a finite outer contour Γ_1 and a vanishingly small inner contour Γ_0.

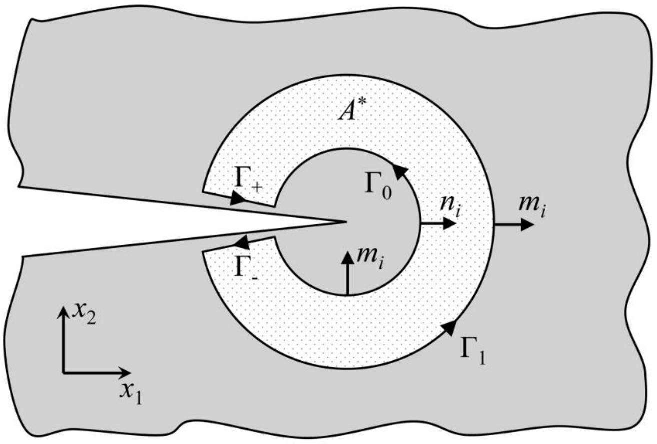

Figure 3.5. A domain contour around the crack tip analyzed by energy domain integral.

Generally, the *J* integral can be calculated along Γ_1 or Γ_0 for linear or nonlinear elastic material but only the inner contour integral renders the right value of *J* under quasistatic conditions. The energy domain integral approach analyzes the *J* integral by calculating an area integral rather than a contour integral for 2-D problems and a volume integral rather than an area integral for 3-D problems. This approach is much more efficient and accurate in numerical calculation for both quasistatic and dynamic fracture problems with elastic, plastic, viscoplastic and thermal deformations. The energy domain integral approach proposes that for quasistatic conditions, the *J* integral can be calculated along a closed contour $\Gamma^* = \Gamma_1 + \Gamma_+ + \Gamma_- - \Gamma_0$ as

$$J = \int_{\Gamma^*} \left(\sigma_{ij} \frac{\partial u_j}{\partial x_1} - w\delta_{1i} \right) q m_i d\Gamma - \int_{\Gamma_+ + \Gamma_-} \sigma_{2j} \frac{\partial u_j}{\partial x_1} q d\Gamma \tag{3.44}$$

where Γ_+ and Γ_- are the integral paths along the upper and lower crack surfaces, respectively, as shown in Fig. 3.5. Here, m_i is the outward normal on Γ^* with $m_i = -n_i$ on Γ_0, $m_1 = 0$ and $m_2 = \pm 1$ on Γ_+ and Γ_-. The smooth function q has arbitrary values with unity on Γ_0 and zero on Γ_1. If there is no traction on crack surface, by applying the divergence theorem, Eq. (3.44) can be expressed as

$$\begin{aligned} J &= \int_{A^*} \frac{\partial}{\partial x_i}\left\{\left[\sigma_{ij}\frac{\partial u_j}{\partial x_1} - w\delta_{1i}\right]q\right\}dA \\ &= \int_{A^*}\left(\sigma_{ij}\frac{\partial u_j}{\partial x_1} - w\delta_{1i}\right)\frac{\partial q}{\partial x_i}dA + \int_{A^*}\left[\frac{\partial}{\partial x_i}\left(\sigma_{ij}\frac{\partial u_j}{\partial x_1}\right) - \frac{\partial w}{\partial x_i}\right]qdA \end{aligned} \tag{3.45}$$

where A^* is the area of contour domain enclosed by Γ^*, as shown in Fig. 3.5. According to the definition of strain energy density ($w = \int_0^{\varepsilon_{ij}} \sigma_{ij} d\varepsilon_{ij}$), we can get

$$\frac{\partial w}{\partial x} = \frac{\partial w}{\partial \varepsilon_{ij}}\frac{\partial \varepsilon_{ij}}{\partial x} = \sigma_{ij}\frac{\partial \varepsilon_{ij}}{\partial x} \tag{3.46}$$

Eq. (3.46) holds only when *w* is presented by an elastic potential with the properties of $\sigma_{ij} = \frac{\partial w}{\partial \varepsilon_{ij}}$. Under small strain condition, by applying the strain-displacement relationship, we can get

$$\frac{\partial w}{\partial x} = \frac{1}{2}\sigma_{ij}\left[\frac{\partial}{\partial x}\left(\frac{\partial u_i}{\partial x_j}\right) + \frac{\partial}{\partial x}\left(\frac{\partial u_j}{\partial x_i}\right)\right] = \sigma_{ij}\frac{\partial}{\partial x_j}\left(\frac{\partial u_i}{\partial x}\right) \tag{3.47}$$

That is,

$$\frac{\partial}{\partial x_i}\left(\sigma_{ij}\frac{\partial u_j}{\partial x_1}\right) - \frac{\partial w}{\partial x_1} = 0 \tag{3.48}$$

Substituting Eq. (3.48) into Eq. (3.45) leads to

$$J = \int_{A^*}\left(\sigma_{ij}\frac{\partial u_j}{\partial x_1} - w\delta_{1i}\right)\frac{\partial q}{\partial x_i}dA \tag{3.49}$$

Eq. (3.49) is applied to the linear or nonlinear elastic problems under the quasistatic conditions where only elastic strain is taken into consideration. This equation is equivalent to Rice's path-independent *J* integral. If all of the elastic strain, plastic strain, thermal strain, body forces and crack face-tractions are taken into consideration, Eq. (3.49) can be derived to a generalized form as

$$\begin{aligned} J = \int_{A^*} \left[\left(\sigma_{ij} \frac{\partial u_j}{\partial x_1} - w\delta_{1i} \right) \frac{\partial q}{\partial x_i} + \left(\sigma_{ij} \frac{\partial \varepsilon_{ij}^p}{\partial x_1} - \frac{\partial w^p}{\partial x_1} + \alpha \sigma_{ii} \frac{\partial \Theta}{\partial x_1} - F_i \frac{\partial u_j}{\partial x_1} \right) q \right] dA \\ - \int_{\Gamma_+ + \Gamma_-} \sigma_{2j} \frac{\partial u_j}{\partial x_1} q d\Gamma \end{aligned} \tag{3.50}$$

In Eq. (3.50), if the additional terms are taken into consideration, the *J* integral becomes path-dependent. For elastic materials, the *J* integral is path-independent while for plastic materials or materials subject to thermal strain, the *J* becomes path-dependent [192,193]. A steady value of *J* at remote contours, especially by adopting an energy domain integral method, can be calculated as a criterion to predict the crack propagation.

c. *Implementation of finite element*

In the finite element analysis for 2-D problems, the crack tip is usually taken as the inner contour Γ_0 while the outer contour Γ_1 coincides with the element boundary around the crack tip [190]. Under this circumstance, the *J* integral can be calculated within the area of Γ_1. A similar volume domain can be defined for 3-D cases. The *q* function should be defined at all nodes within the domain area or volume. The value of *q* should be specified at domain boundaries even though the shape of the *q* function is arbitrary and expressed by several functions, such as the pyramid function and the plateau function. Generally, for 2-D cases, $q=1$ at the inner contour Γ_0 while $q=0$ at the outer contour Γ_1. It has been shown that the shape of *q* function has little effect on the computed value of the *J* integral. The value of *q* can be interpolated as

$$q(x_i)=\sum_{I=1}^{n} N_I q_I \tag{3.51}$$

where *n* is the number of nodes within an element, q_I is nodal value of *q* and N_I is the element shape function. The special derivatives of *q* can be expressed as

$$\frac{\partial q}{\partial x_i}=\sum_{I=1}^{n}\sum_{k=1}^{2\,\mathrm{or}\,3}\frac{\partial N_I}{\partial \xi_k}\frac{\partial \xi_k}{\partial x_j}q_I \tag{3.52}$$

where ξ_i are the parametric coordinates of the elements. If the plastic strain, thermal strain and body forces are not involved, the discretized form of the contour-independent *J* integral under elastic strain and crack surface tractions can be expressed as

$$J=\sum_{A^*\,\mathrm{or}\,V^*}\sum_{p=1}^{m}\left\{\left[\left(\sigma_{ij}\frac{\partial u_j}{\partial x_1}-w\delta_{1i}\right)\frac{\partial q}{\partial x_i}\right]\det\left(\frac{\partial x_j}{\partial \xi_k}\right)\right\}_p w_p-\sum_{\text{Crack faces}}\left(\sigma_{2j}\frac{\partial u_j}{\partial x_1}q\right)w \tag{3.53}$$

where *m* is the number of Gaussian points in an element, and w_p and w are the weighting factors. It should be noted that the terms in $\{\ \}_p$ are required to be evaluated at Gaussian points.

The crack meshes always adopt the quadratic elements in the finite element analysis. These elements have mid-side and corner nodes with quadratic shape functions, as shown in Figs. 3.4 and 3.6a. The linear elements using 4-node for two-dimensional cases (or 8-node for three-dimensional cases) are also available but further refinement of the meshes is required to achieve the same level of accuracy. Generally, the quadrilateral elements are adopted to analyze the crack in 2-D problems since most postprocessing algorithms cannot handle the triangular elements. At the crack tip, a special technique is used to collapse the quadrilateral elements to triangles, as shown in Fig. 3.6a. This doesn’t mean the quadrilateral elements are transformed to the triangular elements. Instead, three nodes on one side of the quadrilateral elements, such as the nodes 1, 2 and 5 in Fig. 3.6a, occupy the same point in space. For the elastic problems, the collapsed nodes at the tip of crack should be tied and a $1/\sqrt{r}$ strain singularity can be obtained by moving the mid-side node to the 1/4 positions. While for the perfectly plastic problems without hardening, the collapsed nodes at the tip of crack should not be tied so that the mid-side nodes give a $1/r$ strain singularity.

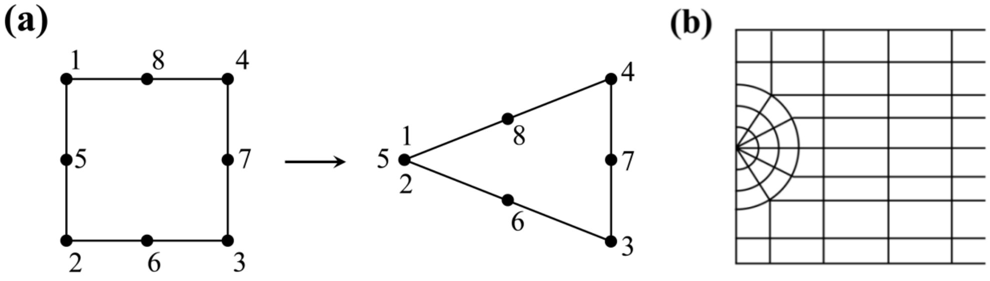

Figure 3.6. (a) Degeneration of a quadrilateral element into a triangular one at the crack tip in 2-D case. (b) “Spider-web” mesh design for an edge-cracked plate.

The “spider-web” configuration has been proved to be the most efficient design of the mesh for the crack-tip region, as shown in Fig. 3.6b for a 2-D plate with a crack. This configuration is consisted of concentric annuluses of quadrilateral elements which are centered at the tip of crack. The innermost quadrilateral elements are degenerated to triangles that are focused on the tip of crack. Proper refinement of the meshes should be adopted to achieve higher accuracy. The J integral can be calculated from the smooth concentric integration domains. For elastic problems, the stress intensity and energy release rate can be calculated with relatively coarse meshes since the crack tip fields are not required to be solved accurately by the domain integration method. On the contrary, for the elastic-plastic problems, the meshes should be sufficiently refined to capture the high level of plastic deformation and calculate the energy release rate.

In this chapter, research methods, including experimental and theoretical approaches, were studied and discussed. These methods will be used to study the four kinds of core-shell nanostructured electrode materials in Chapters 4-7.

Chapter 4. Carbon-coated SnO_2 nanowire electrode[1]

The tin-based oxide materials were commercialized as the electrode materials more than twenty years ago [4,194]. Tin dioxide (SnO_2) anode has theoretical capacity as high as 781 mA h g^{-1}. The high capacity results from the insertion of lithium ions into the SnO_2 electrode materials through the Reactions (2.1) and (2.2) [1]. However, the insertion and extraction of lithium ions induce a colossal volume change of ~280%, leading to the fracture and pulverization of SnO_2 electrode materials and the poor cycling performance of whole lithium ion battery [13,195]. In order to maintain the structural integrity of the electrode materials, carbon coating materials have been used to constrain the volume change and avoid fracture of the electrode materials. Not only the electrochemical performance is improved by the carbon coating technique [196], but also the diffusivity of lithium ions and the electronic conductivity are increased a lot [197-199]. In addition, the solid electrolyte interface (SEI), formed by the decomposition of the electrolyte and the reaction between the electrolyte and the electrode materials, becomes much more stable on the surface of the carbon shell. The stable SEI further contributes to the stability of the carbon-coated SnO_2 electrode materials. Even though the carbon coating technique provides so many advantages for the improvement of cycling performance, the total capacity decreases due to the lower capacity of carbon (372 mA h g^{-1}) in comparison to that of SnO_2. Therefore, on the one hand,

---

[1] The work done in this chapter has been published in the following referred journal paper: Q. Li†, W. Li†, Q. Feng, P. Wang, M. Mao, J. Liu, L. Zhou, H. Wang, H. Yao, Thickness-dependent fracture of amorphous carbon coating on SnO_2 nanowire electrodes, *Carbon* 80 (2014) 793-798. (†Co-first authors)

enough amount of carbon shell should be coated to maintain the structural integrity and improve the cycling performance of the SnO_2 electrode materials. On the other hand, carbon shell should be used as little as possible to increase the total capacity of the electrode. That is, it is important to determine how much carbon should be used so that the structural integrity and capacity can be optimized at the same time.

In this chapter, we began with the discussion on the experimental observation of the thickness-dependent fracture of the carbon shell in the carbon-coated SnO_2 nanowire electrode materials during *in situ* lithiation. Theoretical modeling was subsequently adopted to describe the lithiation process and calculate the concentration of lithium ions in the nanowire electrode based on the equation of diffusion together with initial and boundary conditions. After that, finite element simulation was used to calculate the stress evolution in the carbon shell and find the optimal thickness of carbon shell to maintain the structural integrity and achieve high capacity for the carbon-coated SnO_2 nanowire electrode materials.

4.1. Thickness-dependent fracture of carbon shell

The carbon-coated SnO_2 nanowires were synthesized by hydrothermal templating method. The nanowires were lithiated with the *in situ* observation of TEM (JEM-2100, JEOL). It was found that the lithiation reaction front moves along the nanowire during lithiation, which can be indicated by the volume expansion and phase transition of the nanowire, as shown in Fig. 4.1. The formation of the amorphous phase due to the lithiation of SnO_2 can be distinguished from the remaining parts of crystalline SnO_2 by the contrast in the

TEM images. The carbon shells in Figs. 4.1a and b have different thicknesses and by comparing the two groups of snapshots, it can be found that the fracture of the carbon shell is dependent on the thickness of the shell: for the carbon shell with thickness of 8 nm in Fig. 4.1a, ring cracks occur near the reaction front as indicated by the yellow arrows where the shell is bent due to the diameter difference between lithiated and pristine parts of the nanowire; on the contrary, the 11 nm thick carbon shell remain continuous in Fig. 4.1b. No interfacial failure can be observed and the thickness of the carbon shell has negligible volume change during lithiation.

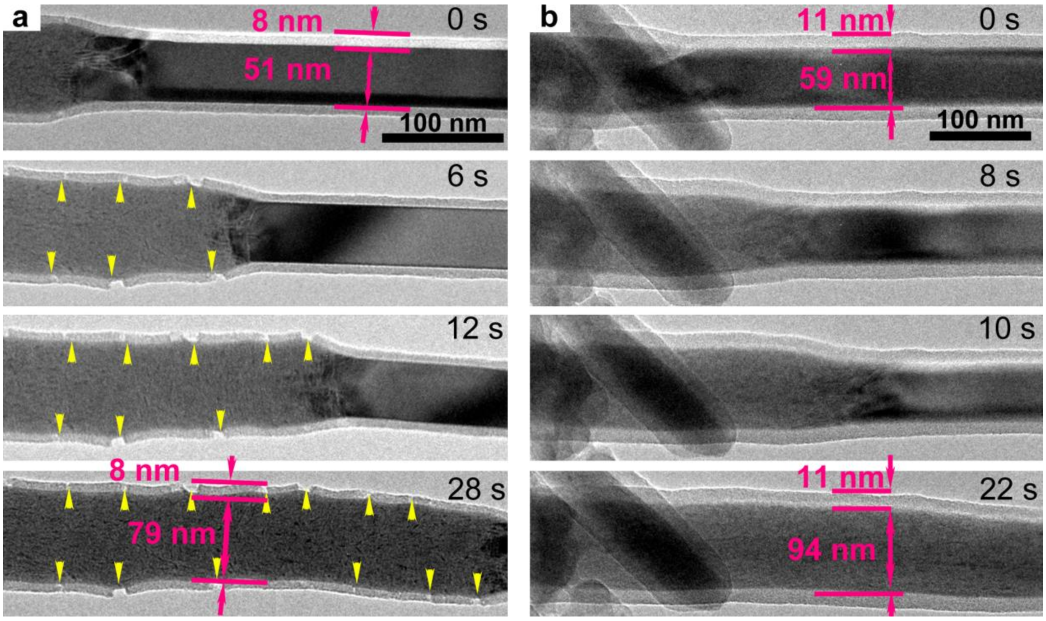

Figure 4.1. Snapshots of the *in situ* lithiation process showing that carbon shell (a) is fractured (marked by yellow arrows) and (b) maintains unfractured during lithiation.

By conducting the lithiation on many nanowires, the fracture was found to be dependent on the geometrical dimensions, which is summarized in Fig. 4.2. The result shows that the thickness, rather than the other parameters such as the diameter of the SnO_2 core, has the dominant influence on fracture occurrence. It can be concluded that the thinner carbon shell is easier to be fractured while the thicker shell can remain integrity during lithiation. A critical thickness of the carbon shell, above which no fracture occurs, is ~9 nm, as highlighted in Fig. 4.2.

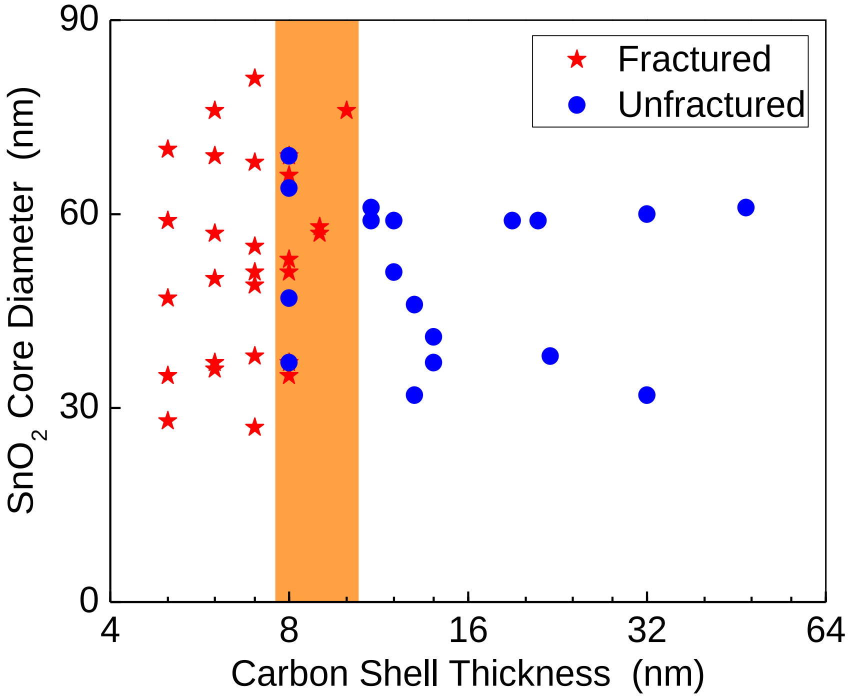

Figure 4.2. Dependence of the fracture of carbon shell on the shell thickness based on *in situ* lithiation observations.

4.2. Theoretical modeling

In order to find the fracture mechanism and explain the thickness-dependent fracture of the carbon shell in the carbon-coated SnO_2 nanowire electrodes, theoretical modeling was conducted. The lithiation process can be regarded as the diffusion of lithium ions into the nanowire from one end to the other during the alloying of lithium ions with the electrode materials. Fig. 4.3 shows the schematic of the diffusion process of the lithium ions (green spheres) in the nanowire electrode when subject to an external voltage. It can be seen that two driving forces contribute to the diffusion of lithium ions: one is the concentration gradient of lithium ions in the nanowire and the other is the external electrical field.

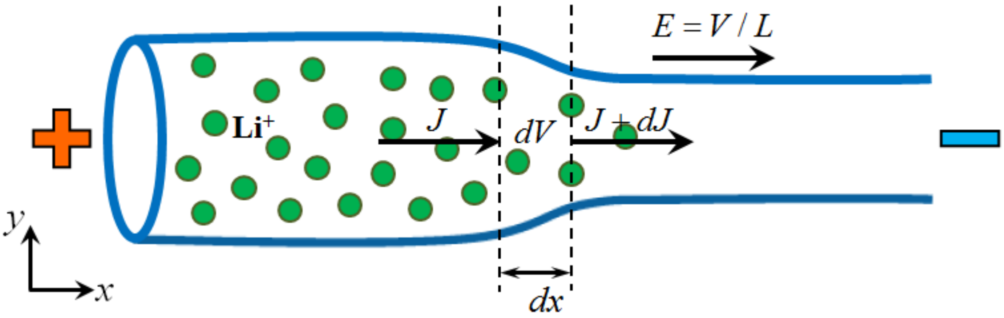

Figure 4.3. Schematic of diffusion of lithium ions in the nanowire electrode subject to an external electric field.

According to Section 3.2.1.c, the diffusion flux *J* of lithium ions along the axial direction can be given by

$$J = \frac{DCe}{k_b T} E - D \frac{\partial C}{\partial x} \tag{4.1}$$

where *D* is the diffusivity coefficient of lithium ions in SnO_2 nanowire, *C* is the concentration of lithium ions in the nanowire, *e* is the charge of one lithium ion, K_b is the Boltzmann constant, *T* is the absolute temperature in Kelvin and *E* is the intensity of the electrical field. Here, the effect of possible stress field and the constraint from carbon shell are ignored. Taking the derivative of Eq. (4.1) with respect to *x* gives

$$\frac{\partial J}{\partial x} = \frac{DEe}{k_b T}\frac{\partial C}{\partial x} - D\frac{\partial^2 C}{\partial x^2} \tag{4.2}$$

According to the conservation of matter, $\frac{\partial J}{\partial x} = -\frac{\partial C}{\partial t}$, Eq. (4.2) is transformed as

$$D\frac{\partial^2 C}{\partial x^2} - \frac{DEe}{k_b T}\frac{\partial C}{\partial x} = \frac{\partial C}{\partial t} \tag{4.3}$$

which can be further normalized to be

$$\frac{\partial^2 \overline{C}}{\partial \overline{x}^2} - \frac{\partial \overline{C}}{\partial \overline{x}} = \frac{\partial \overline{C}}{\partial \overline{t}} \tag{4.4}$$

where $\overline{C} = C / C_s$, $\overline{x} = x / l_0$, $\overline{t} = t / t_0$ with $l_0 = \frac{k_b T}{Ee}$, $t_0 = \frac{1}{D}\left(\frac{k_b T}{Ee}\right)^2$ in which C_S is the concentration of lithium ions in the fully lithiated phase, l_0 and t_0 are the characteristic length and time scales of the system. Now Eq. (4.4) can be solved in a dimensionless time-space domain. The lithiation is assumed to start from $t = 0$, then the initial condition of the normalized concentration of lithium ions can be given by

$$\overline{C}(\overline{t} = 0) = \begin{cases} 1 & (\overline{x} = 0) \\ 0 & (\overline{x} > 0) \end{cases} \tag{4.5}$$

The solution of Eq. (4.4) can be calculated as

$$\overline{C}(\overline{x}, \overline{t}) = \begin{cases} 1 & (\overline{x} < \overline{t}) \\ 1 - \mathrm{Erf}\,(\frac{\overline{x} - \overline{t}}{2\sqrt{\overline{t}}}) & (\overline{x} \geq \overline{t}) \end{cases} \tag{4.6}$$

where Erf(z) is the error function defined by $\mathrm{Erf}(z)=\frac{2}{\sqrt{\pi}}\int_0^z e^{-y^2}dy$. The detailed solution can be found in Appendix A. The concentration of lithium ions can be calculated at specific moments and positions in the nanowire, as shown in Fig. 4.4. It can be summarized from Fig. 4.4 that the nanowire can be divided into three parts based on the concentration of lithium ions. In the part of $\bar{x}\leq\bar{t}$ (or $x\leq l_0 t/t_0$), the concentration of lithium ions is C_s and this part of nanowire can be termed as the “saturation” region. In this region, the nanowire is fully lithiated and the advancing speed of the reaction front can be calculated as l_0/t_0. Following the “saturation” region is the “transition” region, where the concentration of lithium ions decreases from C_s to zero. If 1%C_s is chosen as the cut-off of zero lithium ion concentration, the other bound of the “transition” region is $x=l_0\left(t/t_0+4.6\sqrt{t/t_0}\right)$ and the advancing speed of this region is calculated as $2.3\sqrt{l_0^2/t_0 t}$. The length of the “transition” region is $4.6 l_0\sqrt{t/t_0}$ which is continually increased upon further lithiation. After the “transition” region, since the concentration of lithium ions is lower than 1%C_s, this region is termed as “unlithiated” or “pristine” region. Here, the external electrical field leads to the formation of the “saturation” region while the “transition” region results from the gradient of the lithium ion concentration.

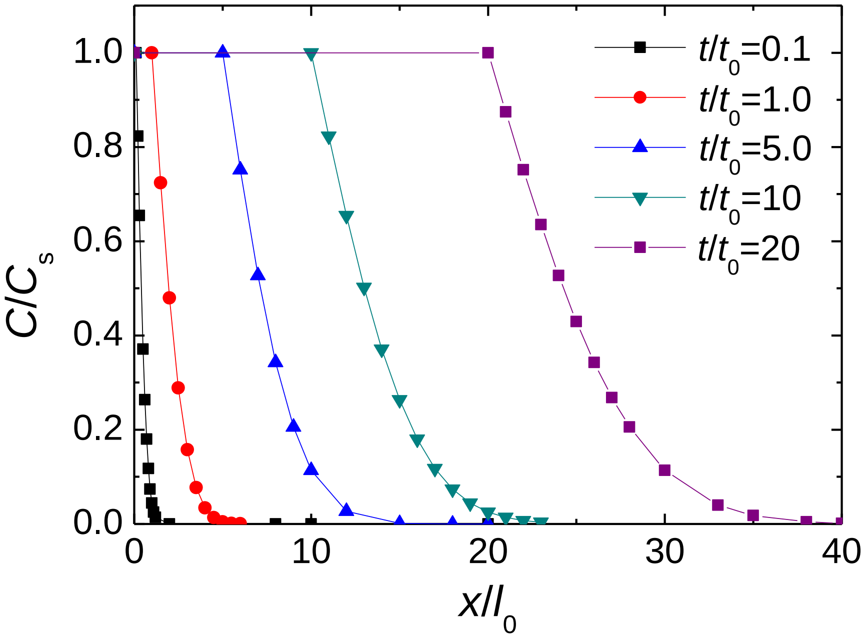

Figure 4.4. Distribution of concentration of lithium ions at different time and positions in the nanowire electrode.

4.3. Finite element simulation

After obtaining the concentration of lithium ions in the nanowire, the volume expansion and corresponding deformation and stress states were calculated by finite element simulation. Assuming the volume expansion of the nanowire is proportional to the concentration of lithium ions, the lithiation-induced volume expansion of the nanowire can be analogously regarded as the thermal expansion of the nanowire if the coefficient of thermal expansion is taken as the coefficient of the lithiation-induced expansion, which is equal to the strain of the unconstrained nanowire at full lithiation. The increase of lithium ion concentration in the nanowire can be treated as the “temperature” increment in the finite element model, as shown in Fig. 4.5. Therefore, the lithiation-induced stress can be calculated as the thermal stress.

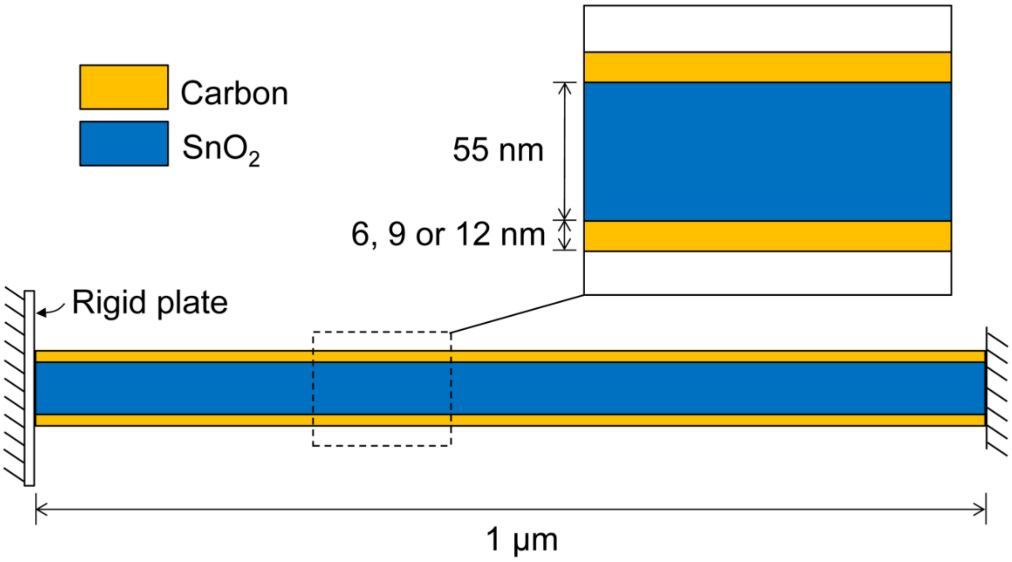

Figure 4.5. Schematic of the finite element model for the carbon-coated SnO_2 nanowire electrode.

A finite element model was established to simulate the lithiation-induced volume expansion in the carbon-coated SnO_2 nanowire electrode. In the model, as shown in Fig. 4.5, the carbon shell was assumed as elastic materials with Young’s modulus and Poisson’s ratio as 300 GPa and 0.25 [200,201]. It should be pointed out that the lithiation of carbon was not taken into consideration in the simulation due to two factors. On the one hand, the lithiation-induced volume expansion of carbon is only 12% [202], which is much lower than that of SnO_2 (~280%). On the other hand, the lithiation has little effect on the mechanical properties of carbon. For example, the tensile stiffness of the carbon fiber does not change while the tensile strength drops by only ~20% due to lithiation [203,204]. After lithiation, the SnO_2 core is transformed into Li_2O, Sn and Li_xSn [1] and the core was assumed to be elastic-perfectly-plastic material with Young's modulus, Poisson's ratio and yielding stress as 150 GPa, 0.3 and 7 GPa [205]. It can be observed from Fig. 4.1 that the radial expansion of the nanowire is around 60%. Such high strain will induce an extremely high hoop stress in the carbon shell. Since the amorphous carbon shell cannot sustain strain of more than 15% [201], cracks will surely form along the longitudinal direction in the carbon shell. But these cracks cannot be directly observed by using TEM due to the limitation in our experiments. Due to the formation of the longitudinal crack, the radial mechanical constraint and the hoop stress caused by the carbon shell can be greatly released. Therefore, the effects from the constraint and the stress field were ignored in the theoretical modeling. Subsequently, the problem can be simplified into a two-dimensional plane stress problem, as shown in Fig. 4.5. Two-dimensional 4-node plane stress thermally coupled quadrilateral bilinear displacement-temperature element (CPS4T) was adopted for both SnO_2 core and carbon shell. The coefficient of "thermal" expansion was taken as 0.5 which corresponds to a 0.5 strain for SnO_2 at full lithiation. The whole model was implemented with a commercial finite element package (ABAQUS, Dassault Systèmes). In order to explain the thickness-dependent fracture of the carbon shell, three different thicknesses (6 nm, 9 nm and 12 nm) were adopted to make a comparison.

Since the concentration of lithium ions in Eq. 4.6 is given in the normalized time-space domain, in order to implement the concentration into the finite element model as the analogous "temperature" increment, the value of the characteristic length l_0 and time t_0 must be given. The length of the nanowire was ~1 μm and the applied voltage was ~2 V, therefore the magnitude of the electrical field intensity E, which is equal to the gradient of the electrical potential, was around 2 × 10^6 V/m. Taking $D = 1.26 \times 10^{-16}$ m^2/s [41], temperature T as 293 K, charge of one lithium ion or electron e as 1.6 $\times 10^{-19}$ C and Boltzmann constant K_b as 1.38 × 10^{-23} J/K, the characteristic length $l_0 = \frac{k_b T}{Ee}$ and time $t_0 = \frac{1}{D}\left(\frac{k_b T}{Ee}\right)^2$ can be calculated as around 12.6 nm and 1.26 s. The advancing speed of the saturation region l_0 / t_0 can be estimated as around 10 nm/s, which is comparable to the value observed from the TEM images in Fig. 4.1.

4.4. Optimal thickness of carbon shell

Upon applying the analogous "temperature" increment in the carbon-coated SnO_2 nanowire electrode, the volume expansion and stress development can be calculated. Fig. 4.6 shows the deformation and stress distribution in the partial lithiated nanowire with carbon shell thickness of 6 nm at $t = 5t_0$. The radial strain of the nanowire is around 56-71% which is comparable with the experimental observation. Such a high radial strain leads to the development of tensile stress in the carbon shell while the compressive stress develops in the lithiated SnO_2 core. The maximum tensile stress occurs at the lithiation front in the carbon shell which is due to the combination of the additional local bending stress and the membrane tensile stress.

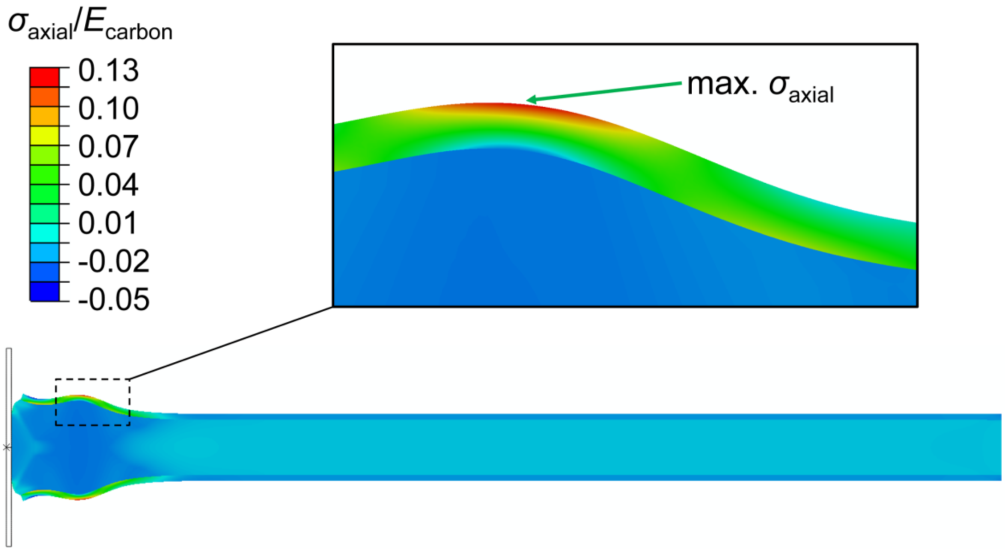

Figure 4.6. Simulation result showing the stress state and deformation of the carbon-coated SnO_2 nanowire electrode after lithiation of $5t_0$.

The evolution of the maximum tensile stress is summarized in Fig. 4.7 for the three cases with different shell thicknesses. For each case, the stress firstly increases as the lithiation proceeds. After reaching the maximum value at around $t = 5t_0$, the stress begins to decrease. By comparing the three different cases, it can be found that the maximum tensile stress depends strongly on the shell thickness: the thinner the shell thickness, the higher the maximum tensile stress. It means that the carbon shell with thinner thickness is easier to be fractured due to the higher tensile stress. It has been shown in the experiments that the critical thickness of carbon shell, above which no fracture occurs, is around 9 nm. According to the maximum tensile stress criterion [180], the strength of the carbon shell can be equal to the maximum tensile stress in the carbon shell with thickness of 9 nm. This value, estimated from Fig. 4.7, is around $0.1E_{carbon}$, which is 30 GPa and agrees well with the values reported in literatures [201,203,204].

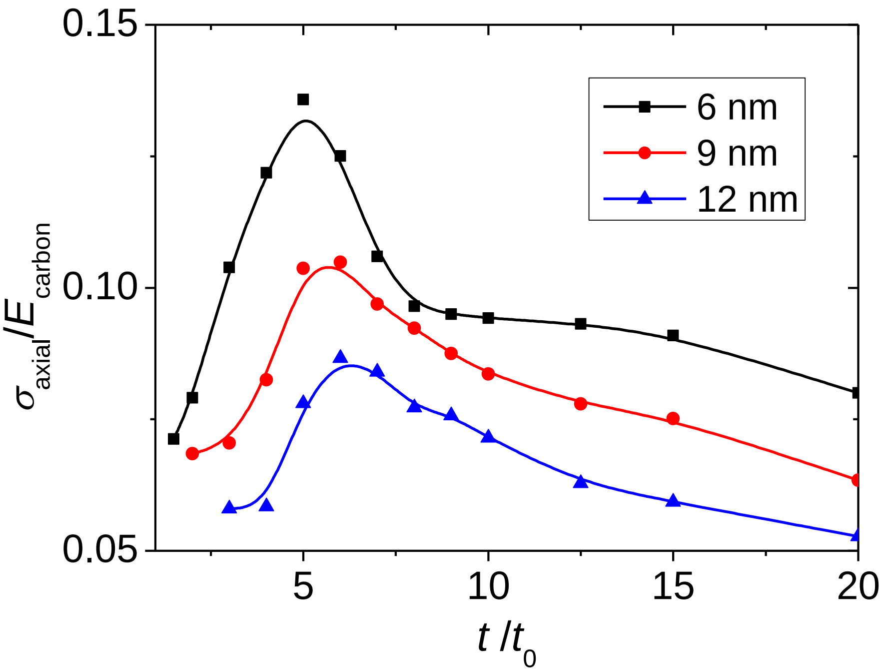

Figure 4.7. Evolution of maximum tensile stress in the carbon shell along axial direction of the nanowire electrode during lithiation.

In this chapter, we focused on the analysis of thickness-dependent fracture of the carbon shell in the carbon-coated SnO_2 nanowire electrodes and the optimization of the electrode materials. *In situ* lithiation showed that the crack in carbon shell of the nanowires is dependent on the thickness of the shell. A critical thickness of ~9 nm, above which no crack occurs, was found based on the experimental observations of nanowires with different thicknesses upon lithiation. The lithiation process of the nanowire was analyzed through theoretical modeling based on the theory of diffusion. The concentration of lithium ions in the nanowire was calculated at specific time and position in the nanowire by solving the equation of diffusion with initial and boundary conditions. By analogously treating the lithiation-induced volume expansion as thermal expansion, the deformation and stress development in the nanowire was obtained by finite element simulations. The maximum axial tensile stress near the reaction front was the reason for the crack initiation and was found to be strongly dependent on the shell thickness: the thinner the shell, the higher the stress. For carbon shells with thickness higher than 9 nm, the maximum tensile stress was always below the fracture strength of amorphous carbon. For those with thickness below 9 nm, the maximum tensile stress became higher than the fracture strength, indicating the fracture of the carbon shell. By adopting this shell thickness (~9 nm), the least amount of carbon will be used so that both structural integrity and maximum capacity can be achieved for the carbon-coated SnO_2 nanowire electrode. The approaches of the theoretical modeling and the finite element simulation should be of great value in analyzing the lithiation in the nanowire-based core-shell nanostructured electrode materials and providing optimal design guidelines for obtaining structural integrity and the highest capacity for the electrode materials at the same time.

Chapter 5. Carbon-coated silicon nanoparticle electrode[2]

Besides SnO_2 anode materials, silicon (Si) anode, as a high capacity electrode material (4200 mA h g^{-1}), also suffers from fracture, pulverization and delamination from current collector due to the dramatic volume change (~400%) during lithiation and delithiation. In order to solve the above problems to achieve stable structural integrity and long cycle life for Si anodes, nanoscale design strategy of the Si anodes has been used and shows that the electrochemical performance can be improved a lot. It was found that the fracture of crystalline Si nanoparticles can be greatly inhibited if their diameter is lower than 150 nm [101]. In addition to the nanoscale design approach, carbon shell has been proved to be an effective way to further optimize the electrochemical performance by constraining the volume change, preventing the formation of unstable solid electrolyte interface on Si surface and increasing the conductivity of lithium ions and electrons, etc. However, in our *in situ* lithiation experiments, it was found that the carbon-coated Si nanoparticles (Si@C NPs) were fractured during lithiation even though the diameter of the crystalline Si nanoparticles was much lower than 150 nm. That is to say, the carbon shell might have a negative effect on the structural integrity of the Si nanoparticle electrode materials by expediting the fracture of the nanoparticle.

---

[2] The work done in this chapter has been published in the following referred journal paper:
W. Li, K. Cao, H. Wang, J. Liu, L. Zhou, H. Yao, Carbon coating may expedite the fracture of carbon-coated silicon core-shell nanoparticles during lithiation, *Nanoscale* 8 (2016) 5254-5259.

In this chapter, in order to investigate fracture mechanism of the Si@C NPs, systematic studies were utilized, including chemical synthesis of the electrode materials, experimental observation of the *in situ* lithiation process and fracture mechanics-based finite element simulation and analysis. First of all, the Si@C NPs were synthesized through hydrothermal method [125]. After that, *in situ* lithiation was conducted on the nanoparticles. The carbon shell was found to facilitate the fracture of the Si nanoparticle and the fracture occurrence was dependent on the geometrical dimensions of the nanoparticles. Finite element simulation was later on conducted to explain the fracture mechanism and an optimal design guideline was proposed to maintain the structural integrity and maximize the capacity for the Si@C NP electrode materials.

5.1. Synthesis and characterization

The synthesis method is shown in Fig. 5.1. Sucrose (600 mg), as the carbon source, was firstly dissolved in a solution of 6 mL deionized water, 8 mL absolute ethanol (99.9 wt%) and 0.6 mL hydrochloric acid (HCl, 37 wt%). The Si nanoparticles (100 mg) were then mixed with the above solution under stirring and then ultrasonicated for 120 min. The total solution was then transferred to a water bath of 70 ˚C under stirring for 3 hours. Subsequently, the solution was dried in the vacuum oven at 120 ˚C for 8 hours. The dried sample (Si-sucrose product) was manually ground and then transformed into the alumina crucible. The crucible was moved to the furnace under the protection of nitrogen and then heated at 800 ˚C for 2 hours. After cooling down, the Si@C NPs were synthesized.

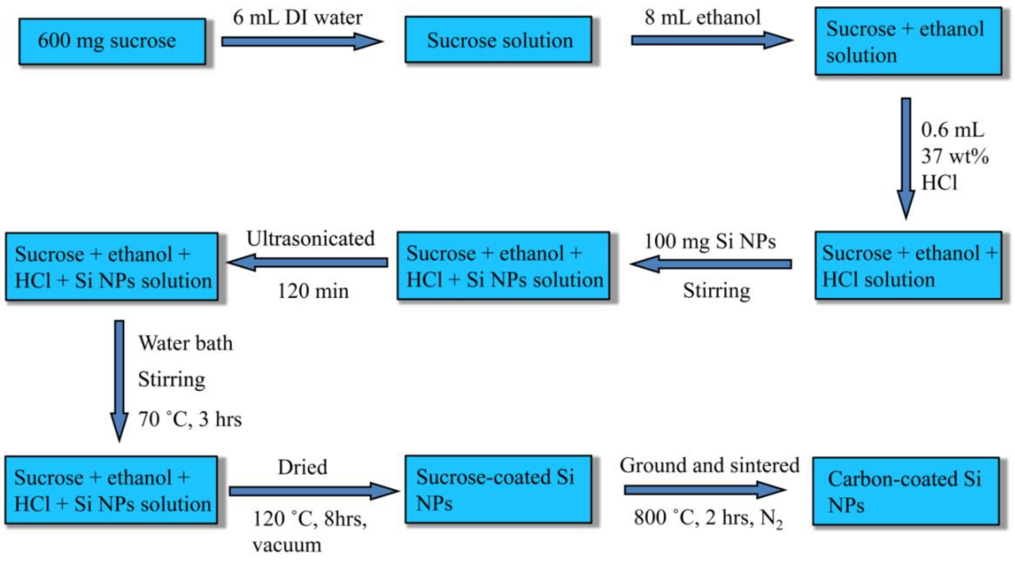

Figure 5.1. Flow chart for the synthesis process of the carbon-coated Si nanoparticle electrode materials.

Figs. 5.2a and b show the morphology and size distribution of the Si@C NPs captured by TEM observation under different magnifications. The Si cores have different diameters and the carbon shells have different thicknesses, indicating the inhomogeneity in geometric sizes of the core-shell structured nanoparticles. The diameters of the Si cores range from 10 to 150 nm while the thicknesses of carbon shells are about 5 to 10 nm. The carbon shell is amorphous and the Si core is crystalline, as shown by the high resolution TEM image in Fig. 5.2c. The crystallinity of Si core can also be confirmed by the selected area electron diffraction pattern as shown in Fig. 5.2d.

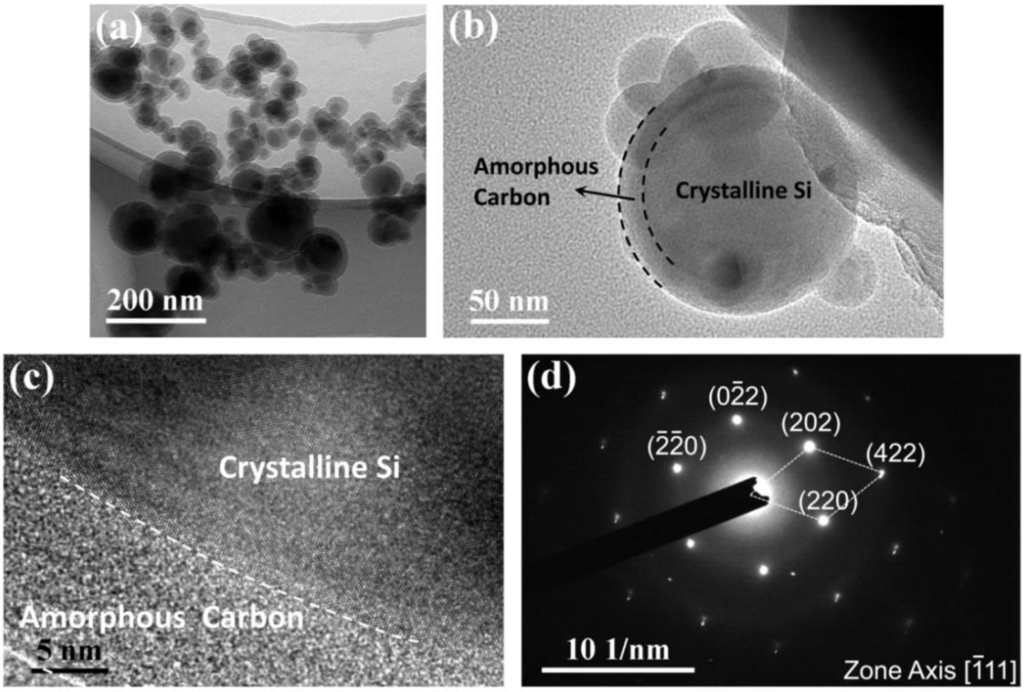

Figure 5.2. (a-b) TEM images showing the morphology of the carbon-coated Si nanoparticles. (c) High-resolution TEM image showing the interface between crystalline Si core and amorphous carbon shell. (d) Selected area electron diffraction pattern of the carbon-coated Si nanoparticle.

5.2. *In situ* lithiation

In order to investigate the lithiation mechanism of the Si@C NP electrodes, *in situ* lithiation was conducted on the nanoparticles with the aid of TEM observation. A solid electrochemical cell was used as the nanoscale battery setup, as shown by the schematic in Fig. 5.3. Then the nanoparticles were attached on the golden rod with silver paste while the counter electrode was the piezo-driven tungsten rod which was covered with lithium metal. A little amount of carbon nanotubes (CNTs) were added into the nanoparticle electrode materials to improve the electrical conductivity. The lithium metal was unavoidable to be oxidized during transferring from glove box into the chamber of TEM. The Li_2O layer formed on the surface and became the solid electrolyte.

The intensity of the electron beam was tuned to the minimum value to avoid the decomposition of the Li_2O layer so that direct contact between the nanoparticles and lithium metal was prevented and the occurrence of the electrochemical reaction was guaranteed. A nano contact between the nanoparticles and the lithium metal was made by moving the tungsten rod and a voltage of –3 V was applied to initiate the lithiation. Lithium ions were transported through the Li_2O layer and inserted into the carbon shell and the Si core. Even though the voltage was higher than a real battery, the electrochemical reaction and phase transition were the same so that the reaction and lithiation/delithiation processes in a real battery can be analyzed by such a nanoscale solid cell inside TEM.

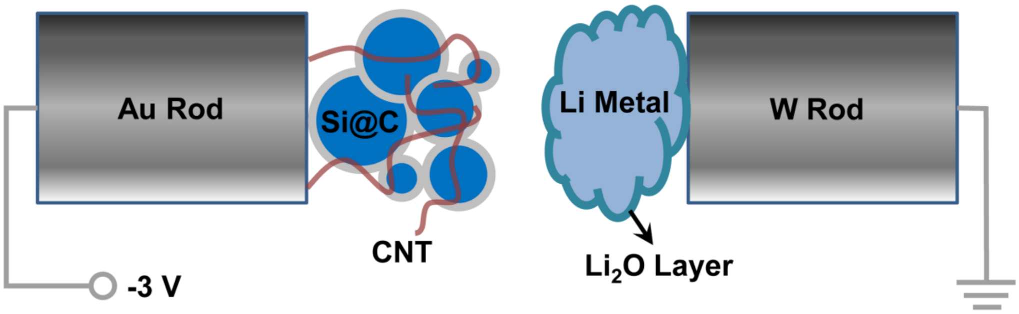

Figure 5.3. Schematic of the setup of the nano half-cell for *in situ* lithiation.

The lithiation process of a Si@C NP was captured and shown in Figs. 5.4a-f. Fig. 5.4a shows the initial state of a nanoparticle with Si core diameter of ~60 nm and carbon shell thickness of ~9 nm. After contacting the lithium metal with the nanoparticle and applying the voltage, the volume of the nanoparticle is expanded due to the insertion of lithium ions and a sharp interface can be clearly seen between the pristine Si core and the lithiated Si shell, as shown in Figs. 5.4b-e. It has been reported that the bare crystalline Si nanoparticle should not be fractured during lithiation if its diameter is lower than 150 nm [101]. However, our *in situ* lithiation result shows that the Si@C NP is fractured as shown in Fig. 5.4f even though the diameter of the Si core is only 60 nm. That is to say, the carbon shell may expedite the fracture of the Si nanoparticle rather than prevent it from being fractured.

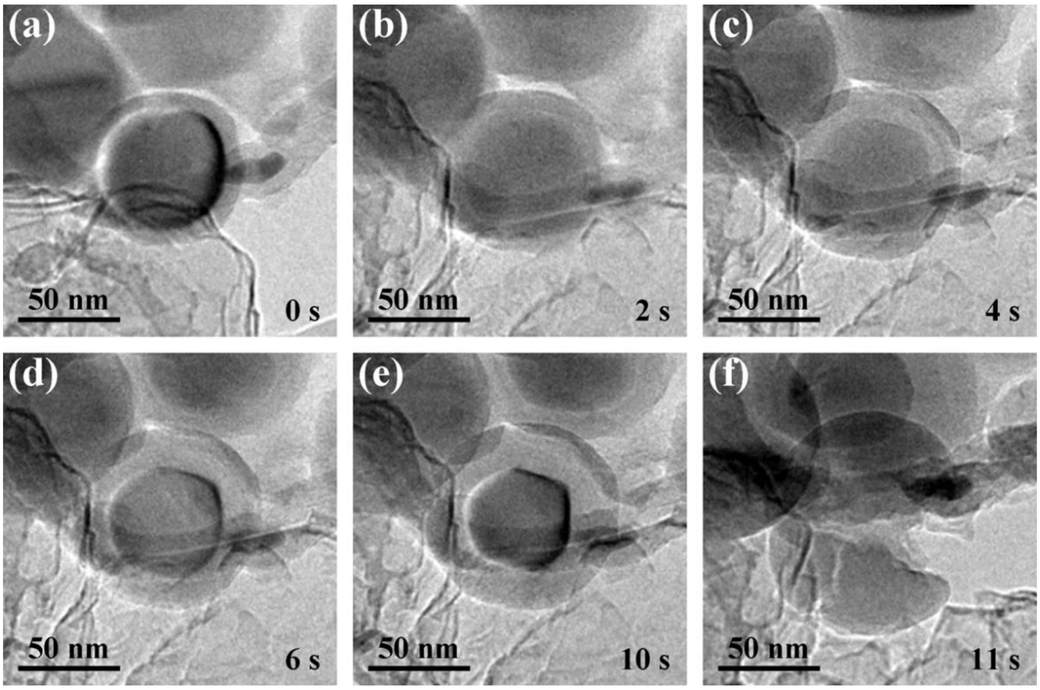

Figure 5.4. Snapshots of the lithiation-induced fracture of the carbon-coated Si nanoparticle electrode materials.

5.3. Geometrical dimension-dependent fracture

In the *in situ* lithiation experiments, we found the geometrical sizes-dependent fracture for the Si@C NP electrode materials during lithiation. The *in situ* lithiation was conducted on dozens of the nanoparticles and the fracture probability is summarized in the *D*-*t* plane, as shown in Fig. 5.5. Here, *D* is the diameter of the Si core while *t* is the thickness of the carbon shell. It can be summarized that the fracture is dependent not only on the diameter of the Si core but also on the thickness of the carbon shell. The nanoparticles tend to maintain integrity with lower *D* and higher *t*. The ratio between *D* and *t* rather than the single *D* or *t* determines the occurrence of the fracture in the nanoparticles upon lithiation. The nanoparticles are fractured when $D/t > 7.0$ while no fracture occurs when $D/t < 3.5$. For the nanoparticles with $3.5 < D/t < 7.0$, whether or not the fracture happens remains random. It can be concluded that there is a critical ratio of *D*/*t* under which the nanoparticles will not be fractured during lithiation and the ratio should be between 3.5 and 7.0.

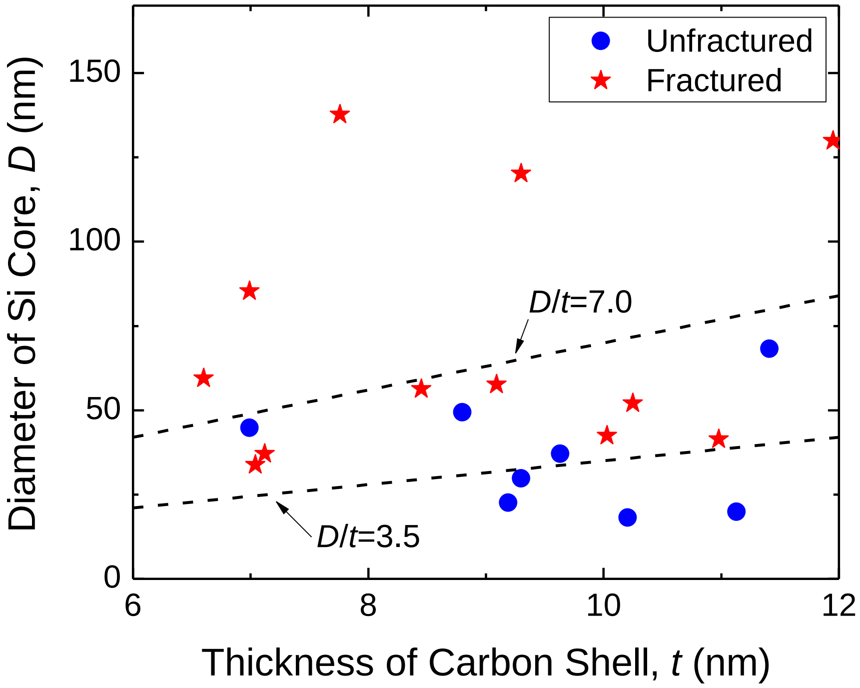

Figure 5.5. Dependence of the lithiation-induced fracture of carbon-coated Si nanoparticles on the diameter of Si core and the thickness of carbon shell.

5.4. Lithiation-induced fracture mechanism

It has been reported that the lithiation in Si is a two-phase reaction-rate controlled process. There is a sharp boundary between the lithiated Si and the pristine Si during lithiation. In order to study the stress and deformation during lithiation and find out the fracture mechanism of the Si@C NPs, such lithiation process was analyzed by finite element simulation. The fracture mechanism was studied by analyzing the stress development in the carbon shell and the energy release rate at the tip of crack after the fracture of the shell.

5.4.1. Stress evolution in the carbon shell during lithiation

A two-dimensional (plane strain) circular solid model was established to simulate the lithiation in the Si@C NP electrode materials, as shown in Fig. 5.6, to study the fracture mechanism of the nanoparticles. The nanoparticle in the finite element model has a Si core with diameter of 100 nm, which is lower than the threshold of safety size (150 nm), and a carbon shell with thickness of 5 nm. Since the governing equations are similar for the diffusion problem and thermal conduction problem, the lithiation-induced volume expansion was simulated by the analogous thermal expansion by treating the increase in lithium ion concentration as the increment of the temperature. Such a thermal expansion problem could be easily tackled by the commercial finite element simulation package (ABAQUS, Dassault Systèmes).

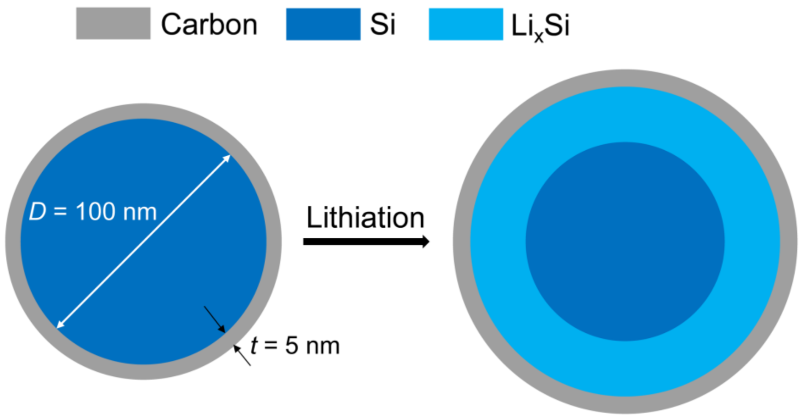

Figure 5.6. Schematic of the finite element model of a carbon-coated Si nanoparticle during lithiation.

To simulate the phase transition during lithiation, the mechanical properties of the Si were assumed to be linearly proportional to the concentration of lithium ions, which was regarded as the normalized temperature in the finite element model. That is, when concentration of lithium ions or the corresponding temperature is zero, the core has the mechanical properties of pristine Si. When the normalized concentration of lithium ions or the temperature is one, the lithiated part of the core will have the properties of lithiated Si ($Li_{15}Si_4$). The lithiation in the carbon shell was neglected due to the negligible volume expansion and the small changes of mechanical properties, as discussed in Section 4.3. Since there is a sharp interface between the pristine Si and the lithiated Si, to simulate the lithiation process, the Si core was divided into many concentric annuluses. To model the inward lithiation process, the prescribed temperature field was applied on the annuluses layer by layer from the outermost one to the innermost one. The simulation results were found to be dependent on the annulus thickness or the number of the annuluses but convergent results could be achieved when the thickness was enough small or the number of the annuluses was enough high, which is discussed in Appendix B. Here, the carbon shell was assumed to be elastic material and the Si and Li_xSi were assumed to be elastic-perfectly-plastic materials with mechanical properties shown in Table 5.1. The radial strain of a Si nanoparticle at full lithiation was adopted as the linear coefficient of the analogous thermal expansion, which was taken as 0.4 for the two-dimensional problem. The bonding between the carbon shell and the Si core was assumed to be perfect and no delamination would occur during lithiation. Such strong interfacial bonding is probably due to the interpenetration of Si and carbon at the interface as shown in Fig. 5.2c and has also been reported in literature [122]. In this finite element simulation, we adopted the two-dimensional eight-node plane-strain thermally coupled quadrilateral, biquadratic displacement-bilinear temperature element with reduced integration (CPE8RT).

Table 5.1. Typical mechanical properties taken in FEA simulations

Materials	Young's modulus (GPa)	Poisson's ratio	Yield strength (GPa)
Carbon	300 [206]	0.25 [206]	-
Si	169 [207]	0.26 [207]	7 [208]
Li_xSi	3.5 [162]	0.23 [166]	0.5 [172,209]

The stress evolution in the carbon shell was firstly analyzed, as shown in Fig. 5.7. It can be found that the maximum tensile stress, which is along the hoop direction, occurs in the carbon shell at the interface. The maximum tensile stress increases with the degree of lithiation. Here the degree of lithiation is defined as the fraction of the Si core that has been lithiated. The maximum tensile stress saturates after 80% lithiation and reaches at ~25 GPa. According to the maximum tensile stress criterion for brittle materials [180], the carbon shell will be fractured if the σ_{max} is higher than the fracture strength σ_{f} of the amorphous carbon. It has been reported that the σ_{f} is around 7 – 30 GPa for the amorphous carbon [206,210]. Therefore, the carbon shell will be fractured at around 6% lithiation if 7 GPa is taken as a conservative estimation of the fracture strength.

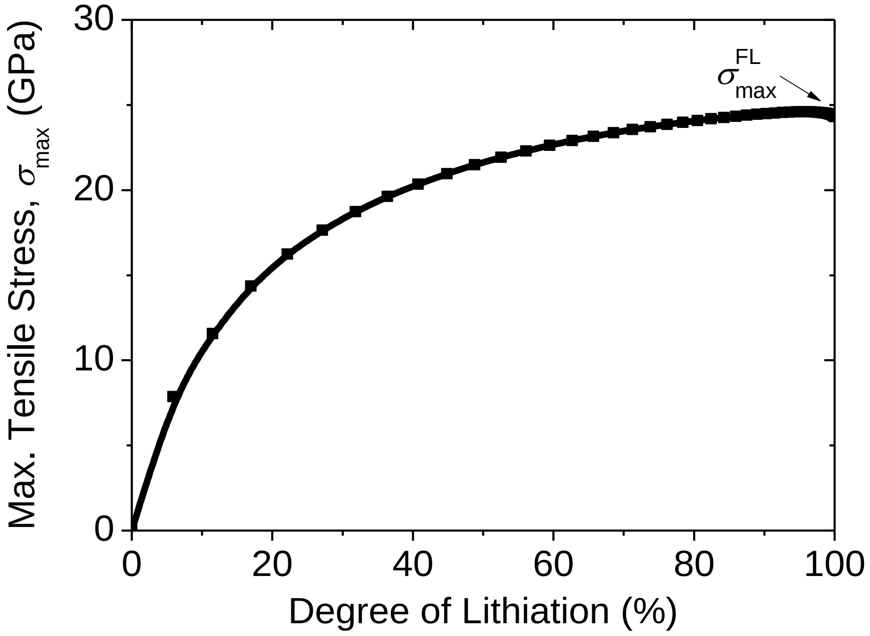

Figure 5.7. Evolution of the maximum tensile stress in the carbon shell during lithiation.

5.4.2. Analysis of crack propagation

Once the carbon shell is cracked, it is important to determine whether the crack can penetrate into the lithiated Si core. As discussed in Section 3.2.2, since the Li_xSi is the elastic-perfectly-plastic material, the propagation can be determined by calculating the energy release rate at the crack tip rather than computing the stress or strain, which is singular near the crack tip. The bonding between the carbon shell and the lithiated Si core is very strong so that the crack is prone to penetrating into the lithiated Si rather than propagating along the carbon/Li$_x$Si interface if the energy release rate at the crack tip is high enough. Such driving force was calculated by J integral [181] through the finite element model as shown in Fig. 5.8. From the magnified image, a crack forms in the carbon shell after 6% lithiation and terminates at the carbon/Li$_x$Si interface. The crack tip is surrounded by many circular contours which are used to calculate the value of J integral.

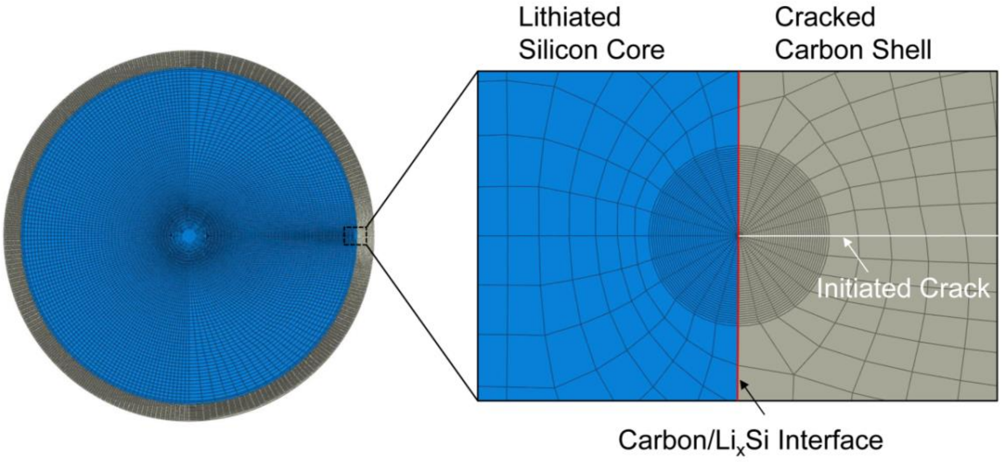

Figure 5.8. Meshed finite element model of the carbon-coated Si nanoparticle with a crack terminating at the carbon/Li$_x$Si interface.

Fig. 5.9 shows the detailed schematic of the contours near the crack tip. The crack tip elements were implemented in ABAQUS, as discussed in Section 3.2.3. The quad-dominated elements were transformed to triangle elements inside the first contour Γ_1 and a singularity of r^{-1} was used for these elements (r is the distance from the crack tip), as shown in Fig. 5.9. The contours were numbered sequentially from the crack tip to the far field.

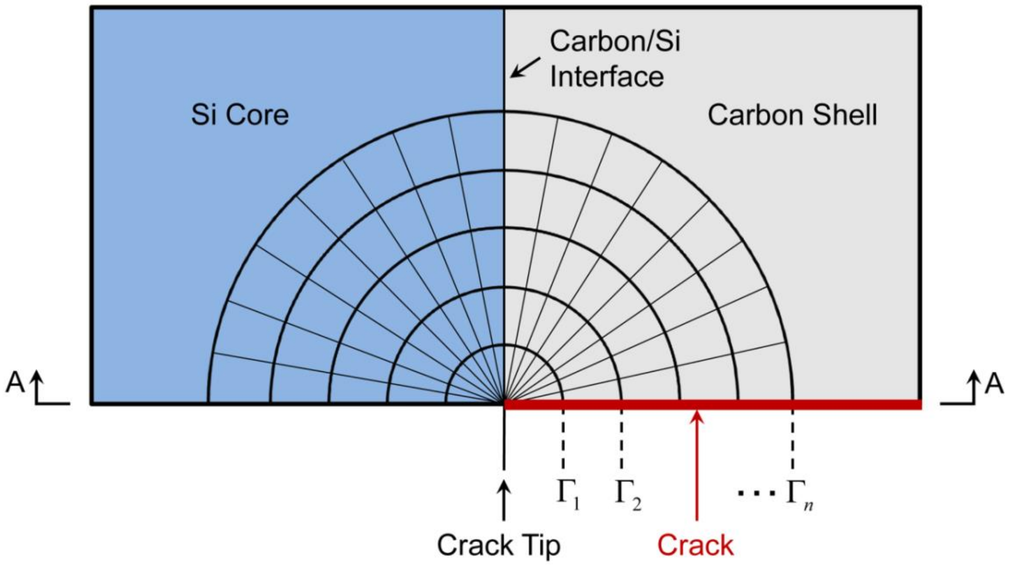

Figure 5.9. Schematic of the contours used for calculation of the *J* integral near the tip of crack.

The values of the *J* integral were calculated and found to have certain path-dependence. But convergent value of *J* integral can be obtained after the fifth contour. Detailed discussion of the path-dependent *J* integral is summarized in Appendix C. Therefore, the *J* value of the fifth contour was used to characterize the propagation of the crack, which is plotted in Fig. 5.10. Since the carbon shell is cracked after 6% lithiation, substantial *J* integral can be observed after such degree of lithiation. The *J* integral is increased rapidly during lithiation and soon exceeds 10 J m^{-2} at around 30% lithiation. It has been reported that the fracture energy, or the critical energy release rate for crack growth of Li_xSi, is around 10 J m^{-2} [174,211]. The *J* integral near the crack tip can easily exceed this value, leading to the penetration of the crack into the lithiated Si core and the fracture of the whole nanoparticle.

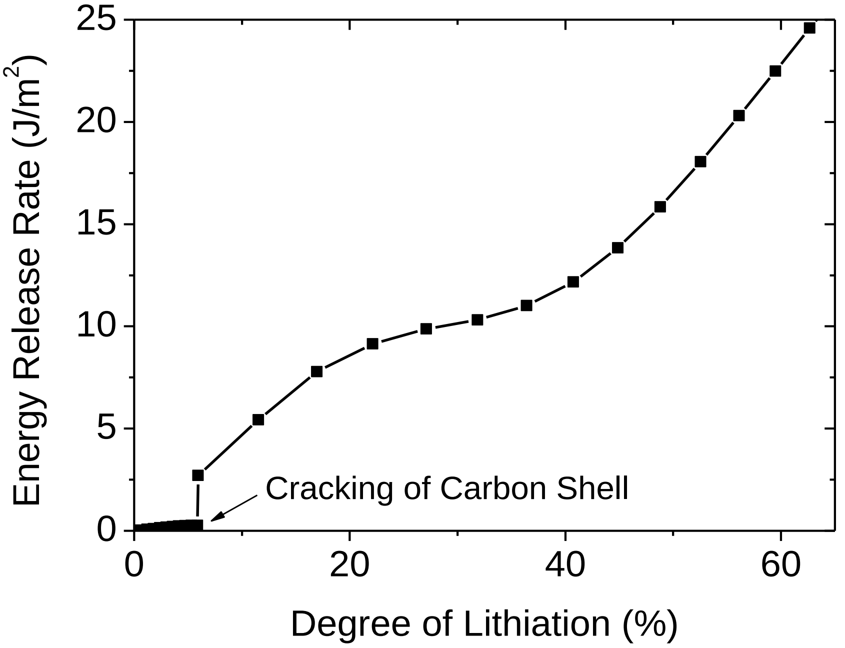

Figure 5.10. Evolution of the energy release rate (*J* integral) near the tip of the crack.

The high energy release rate at the carbon/Li$_x$Si interface is mainly due to the inhomogeneity of the materials along the direction of crack propagation. That is, the difference in mechanical properties between carbon and Li$_x$Si in this case determines the level of energy release rate. It has been reported that such materials' inhomogeneity causes a shielding or anti-shielding phenomenon, depending on the orientation of the inhomogeneity [212]. For example, the crack is facilitated if the crack tends to propagate from the stiff/hard material to the compliant/soft one. On the contrary, the crack is impeded if the crack tends to propagate from the compliant/soft material to the stiff/hard one. It is obvious that our case belongs to the first situation in which carbon is stiffer and harder than the lithiated Si. Therefore, the energy release rate at the crack tip is increased dramatically due to such materials' inhomogeneity. In order to have a better understanding of this effect, a study was conducted by comparing the energy release rate at the crack tip of the Si@C NP and a homogeneous bare Si nanoparticle. Details of the comparison are discussed in Appendix D. Generally, the energy release rate at the crack tip in the Si@C NP increases much faster than that in the bare Si nanoparticle. That is, the carbon shell indeed expedites the crack of the carbon shell and the fracture of the Si@C NP during lithiation.

5.5. Optimization of geometrical dimensions

Even though the carbon shell may facilitate the fracture of the Si nanoparticle during lithiation, the benefits of the carbon shell should not be neglected, such as the good electronic and ionic conductivities and stable solid electrolyte interface on the shell surface. Besides, in our *in situ* lithiation experiments, it was also found that the carbon shell will not be fractured if the geometrical dimensions of the nanoparticles can be optimally designed. Therefore, it is more important to find an optimal design approach so as to take advantage of these benefits as well as avoiding the side effects caused by the fracture and pulverization. According to the above analysis, the carbon shell should not be cracked otherwise the whole nanoparticle will be fractured. As indicated by the experimental observation in Fig. 5.5, the cracking of the carbon shell can be avoided by optimizing the geometrical dimensions (D and t) of the nanoparticles. By using the finite element model in Fig. 5.6, a parametric study was conducted by using different geometrical dimensions to study the stress evolution in the carbon shell. Fig. 5.11 shows the dependence of the maximum tensile stress $\sigma_{\max}^{\mathrm{FL}}$ (normalized by E_{C}) at full lithiation moment on the Si core diameter D and the carbon shell thickness t.

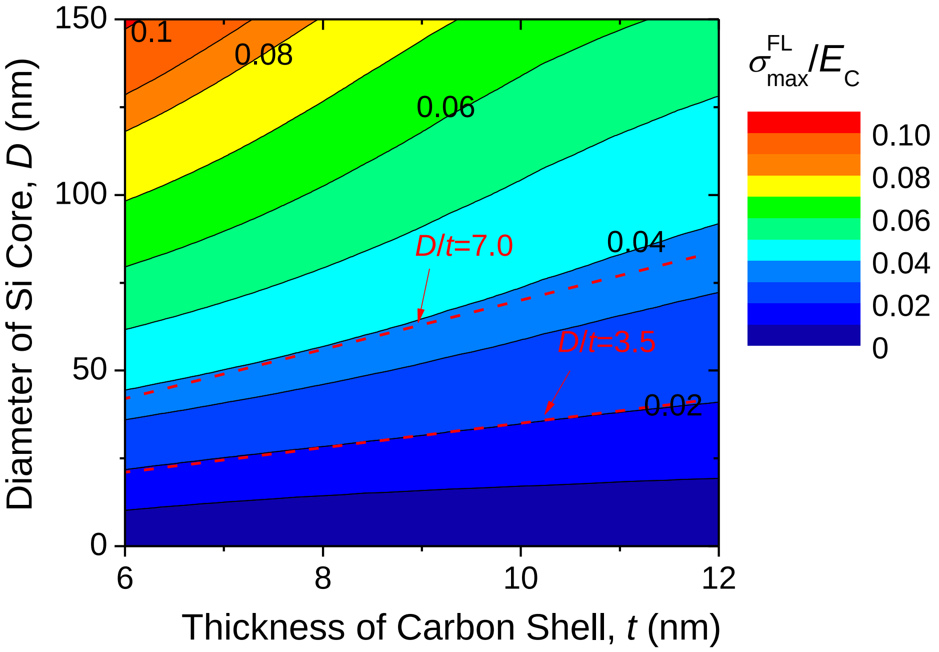

Figure 5.11. Optimal design guideline for the carbon-coated Si nanoparticle electrode materials.

Generally, smaller D and larger t lead to lower $\sigma_{\max}^{\mathrm{FL}}$. It means that the carbon shell can be safer during lithiation if D is decreased and t is increased. This trend agrees well with the experimental observation that the Si@C NPs with smaller D and larger t are easier to remain structural integrity after lithiation. In order to prevent the fracture of the carbon shell, $\sigma_{\max}^{\mathrm{FL}}$ should be lower than the fracture strength of amorphous carbon σ_{f}. For example, if we take σ_{f} as 6 GPa and E_{C} as 300 GPa, the "unfractured" region is the area below the contour line of $\sigma_{\max}^{\mathrm{FL}} / E_{\mathrm{C}} = 0.02$. By comparing with Fig. 5.5, it can be found that this contour line is corresponding to the line defined as $D/t = 3.5$. Similarly, if σ_{f} is taken as 12 GPa, the "unfractured" region will be the area below the contour line of $\sigma_{\max}^{\mathrm{FL}} / E_{\mathrm{C}} = 0.04$, which coincides with the line of $D/t = 7.0$ in Fig. 5.5. Since the fracture of amorphous carbon shell occurs in the region between the two lines of $D/t = 3.5$ and $D/t = 7$ remains random, the fracture strength can be predicted in the range of 6 – 12 GPa. This range is found to be consistent with the value reported in literature [210] and our previous selection of fracture strength (~7 GPa) to judge the initiation of crack in carbon shell for the model in Figs. 5.6 and 5.7.

From the perspective view of capacity, the value of D/t should be as high as possible so that the theoretical capacity of the Si@C NP can achieve a higher value. On the contrary, the value of D/t should be small enough so that the carbon shell, as well as the whole Si@C NP, will not be fractured during lithiation. Based on the above analysis, the value of D/t is chosen as 3.5 so that the nanoparticle electrode materials can remain unfractured and achieve the highest capacity at the same time.

In this chapter, we focused on the explanation of the lithiation and fracture mechanism and the optimal design strategy of the carbon-coated Si nanoparticle electrode materials to avoid the fracture and achieve the high theoretical capacity. First of all, *in situ* lithiation was conducted on the synthesized carbon-coated Si nanoparticles. Previous *in situ* lithiation studies showed that the crystalline Si nanoparticles should not be fractured if its size is below 150 nm. Besides, carbon shell has been normally regarded to protect the Si nanoparticle from being fractured during lithiation. However, in our experiments, an unexpected fracture of the nanoparticles was observed during *in situ* lithation. It was found that the Si nanoparticles are easier to be fractured even though they are coated with an amorphous carbon shell. The carbon shell seems to expedite, rather than impede, the fracture of the Si nanoparticles during lithiation.

It should be pointed out that the Si core has a single crystalline structure (see Fig. 5.2d), indicating the same crystal structure with the reported Si nanoparticle [101]. But the fracture size, as shown by Fig. 5.5, was found to be as small as ~35 nm, which is much smaller than the reported critical value (~150 nm). Besides, a contemporary work also reported the fracture of carbon-coated Si nanoparticle during lithiation in which the size of Si core is ~128 nm, which is also smaller than the critical value [213]. The above comparisons confirm that the particularity of the different Si nanoparticles has no significant effect on the fracture mechanism. In order to find out the fracture mechanism of the carbon-coated Si nanoparticle electrodes, finite element simulation was carried out. It was noticed that the carbon shell will be firstly cracked during lithiation due to the elevated tensile stress. The crack terminating at the crack tip, if subject to further lithiation, tends to propagate into the lithiated Si core and causes the fracture of the whole nanoparticle. The increasing energy release rate at the crack tip is due to the materials' inhomogeneity between the Si core and the carbon shell. Further *in situ* lithiation experiments showed that the fracture can be prevented by controlling the diameter of the Si core and the thickness of the carbon shell. A critical ratio of the diameter over thickness was proposed for the carbon-coated Si nanoparticles so that the fracture can be avoided and the highest theoretical capacity can be obtained. Therefore, through an optimal design strategy of the geometrical dimensions of the carbon-coated Si nanoparticles, the electrode materials can achieve structural integrity and maximum capacity at the same time. Such optimal design guideline should be of great value to the design of core-shell nanostructured high-capacity anode materials for lithium ion batteries.

Chapter 6. Yolk-shell carbon-coated silicon nanoparticle electrode[3]

Coating technique has been widely used to improve the electrochemical performance of the high-capacity anode materials. In Chapter 4 and 5, carbon shell was directly coated on the SnO_2 nanowire and Si nanoparticle electrode materials. It was found that the fracture of carbon shell can be avoided by the optimal design strategies on the geometrical dimensions. However, since much more coating materials are required to resist the lithiation-induced volume expansion and fracture, the total theoretical capacity is decreased due to the lower capacity of carbon than that of SnO_2 or Si. In order to solve the fracture problem as well as increasing capacity for carbon and Si composite electrode materials, the yolk-shell nanostructured electrode materials have been developed and studied. The yolk-shell carbon-coated Si nanoparticle (Si@void@C NP) electrode materials show much better electrochemical performance than the carbon-coated Si nanoparticle electrodes. The improved performance, including the longer cycle life and higher capacity, results from the void space between the Si yolk and the carbon shell to bear the volume change of the Si yolk so that the carbon shell tends to remain structural integrity during cycling. Since the Si yolk can expand more freely, it can accommodate much more lithium ions, leading to a higher capacity for the whole system.

---

[3] The work done in this chapter has been published in the following referred journal paper:
W. Li†, Q. Wang†, K. Cao, J. Tang, H. Wang, L. Zhou, H. Yao, Mechanics-based optimization of yolk-shell carbon-coated silicon nanoparticle as electrode materials for high-capacity lithium ion battery, *Composites Communications* 1 (2016) 1-5. (†Co-first authors)

Besides, the solid electrolyte interface film forms on the surface of the carbon shell and remains unfractured due to the decreased volume expansion of the nanoparticle. All of these advantages contribute to better cycling performance of the nanoparticle electrode materials. Nevertheless, the electrochemical performance, including the cycle life and reversible capacity, varies in different studies, indicating a large space to improve and optimize the performance of the electrode materials. In addition, it is still unclear how much void space should be designed to maintain the structural integrity and maximize the capacity for the Si@void@C NP electrode materials. Therefore, both experimental and theoretical approaches were adopted to study and optimize the Si@void@C NP electrode materials in this chapter.

In situ lithiation was firstly conducted on the Si@void@C NPs. It was found that the fracture is dependent on the geometrical dimensions of the nanoparticles. Later on, rigorous theoretical modeling was established to predict the fracture and the theoretical capacity of the electrode materials. Finally, an optimal design guideline was proposed to maintain the structural integrity and achieve the highest capacity for the Si@void@C NP electrode materials.

6.1. Geometrical dimension-dependent fracture

The Stöber method was used to synthesize the Si@void@C NP electrode materials [123,214,215]. The *in situ* lithiation was conducted on the nanoparticles by using a nanoscale battery setup inside TEM with a Nanofactory® holder, as shown in Fig. 6.1a. The Si@void@C NPs were attached on the golden rod by silver paste and fixed on the holder. The lithium metal was attached on the tungsten rod in a glovebox. During transferring the lithium metal from glovebox to the holder, a Li_2O layer inevitably formed on the surface of lithium metal, serving as the solid electrolyte. The holder was moved into the TEM and then the TEM chamber was vacuumed. After moving the lithium source to contact with the nanoparticles inside the TEM and applying a voltage of –3 V, the nanoparticles can be lithiated. The lithiation process of the nanoparticles was captured by a digital camera inside the TEM.

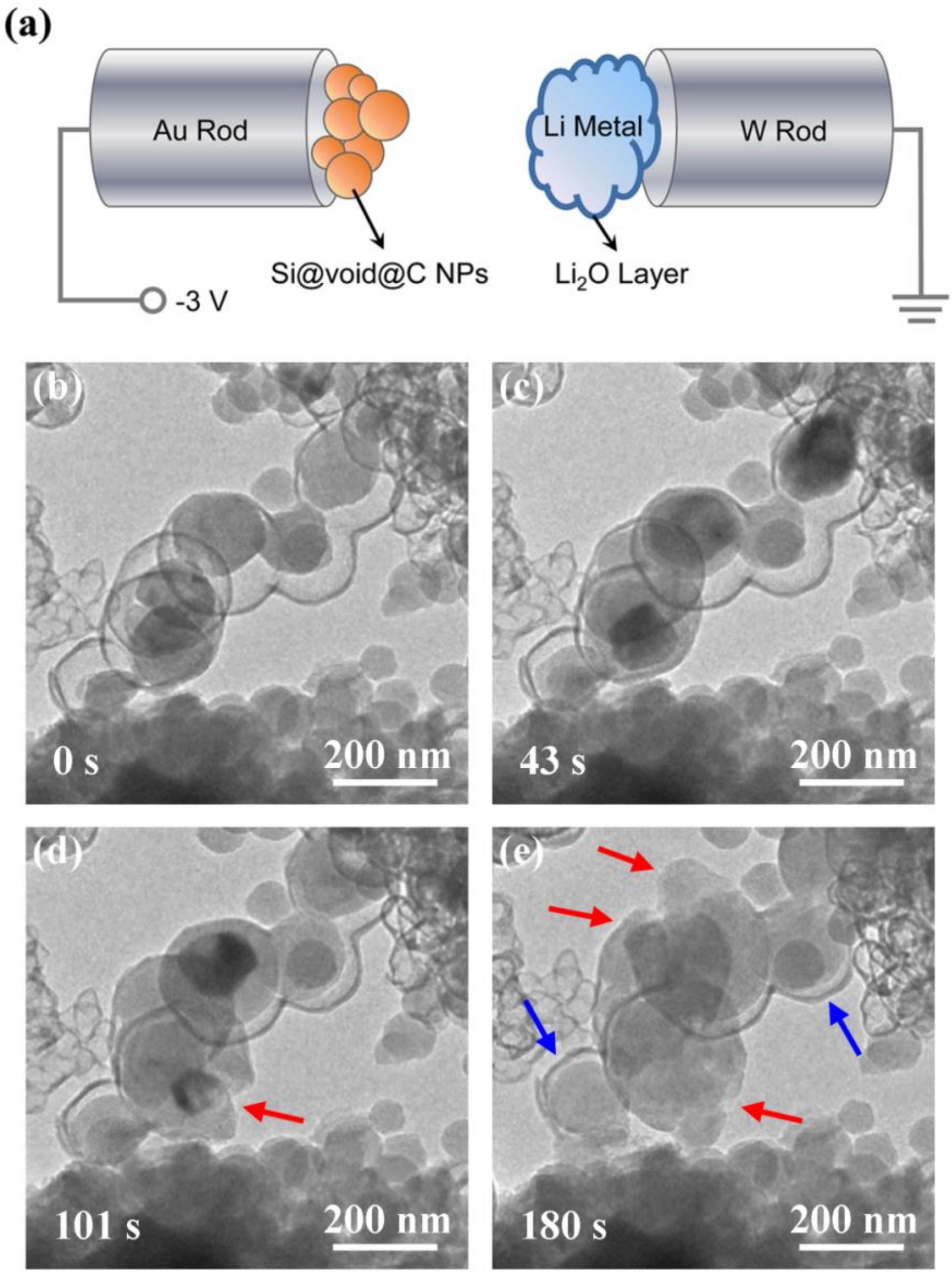

Figure 6.1. (a) Schematic of the setup for the *in situ* lithiation of the yolk-shell carbon-coated Si nanoparticle electrode materials and (b-e) snapshots of the lithiation-induced fracture of the yolk-shell carbon-coated Si nanoparticles during lithiation.

Fig. 6.1b shows the initial state and the morphologies of several nanoparticles in which the void space can be seen between the Si yolk and the carbon shell. After applying the voltage, the nanoparticles are lithiated as shown in Fig. 6.1c.

The volume of the Si yolks is expanded, the void space between the yolk and the shell becomes smaller and the sharp interface appears between the pristine crystalline Si core and the amorphous lithiated Si shell. After lithiation of 101 s, one of the nanoparticles is fractured as indicated by the red arrow in Fig. 6.1d. At the final moment of lithiation in Fig. 6.1e, three of the nanoparticles are fractured as indicated by red arrows while the other two nanoparticles remain continuous as marked by the blue arrows after lithiation of 180 s.

The above *in situ* lithiation was conducted on dozens of the Si@void@C NPs. The fracture and continuity of the nanoparticles are summarized in Fig. 6.2. Here $\overline{R}_{\mathrm{C}}$ and $\bar{t}$ are the radius R_{C} and thickness t of the carbon shell normalized by the radius of the Si yolk R_{Si}. It can be seen that Si@void@C NPs tend to remain unfractured with larger $\overline{R}_{\mathrm{C}}$ and $\bar{t}$ while the nanoparticles are fractured if $\overline{R}_{\mathrm{C}}$ and $\bar{t}$ are smaller. These results show a clear geometrical dimension-dependent fracture of the Si@void@C NPs during lithiation.

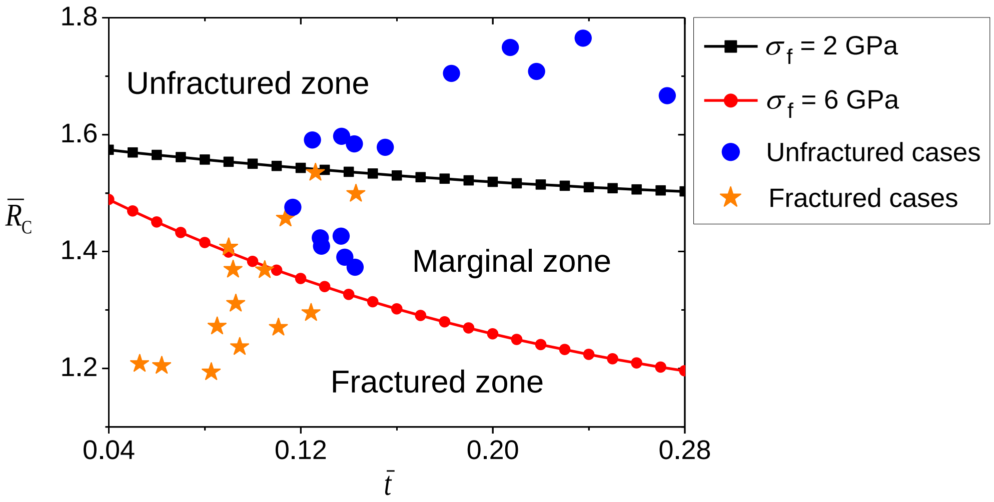

Figure 6.2. Dependence of the lithiation-induced fracture of the yolk-shell carbon-coated Si nanoparticles on the geometrical dimensions $\bar{R}_C$ and $\bar{t}$.

6.2. Theoretical modeling

In order to study the fracture mechanism of the Si@void@C NPs upon lithiation, theoretical modeling is established to calculate the stress and deformation in the carbon shell of the Si@void@C NPs. The tensile stress develops in the carbon shell after the Si yolk contacts with the inner wall of the carbon shell during lithiation, as shown in Fig. 6.3. Upon full lithiation, the lithiated Si yolk is constrained by the carbon shell and subject to hydrostatic compression. Therefore, only elastic deformation is required to be considered in the Si yolk while the influence by the plastic deformation can be ignored.

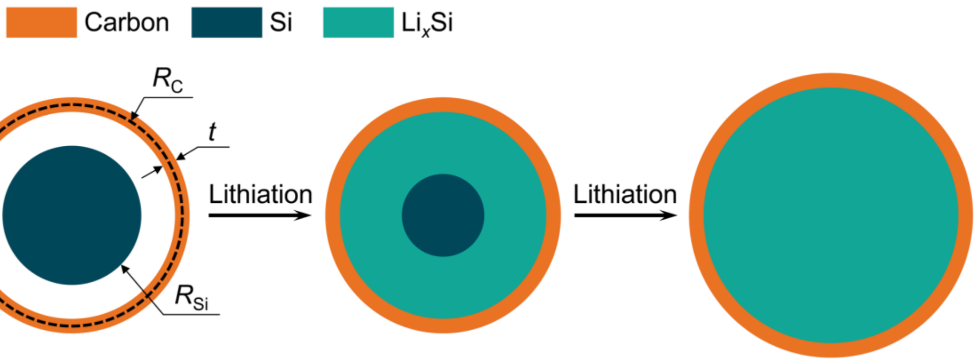

Figure 6.3. Schematic of a yolk-shell carbon-coated Si nanoparticle during lithiation.

At the moment of full lithiation, the mechanical strain in the radial direction $\varepsilon_{\mathrm{Si}}$ in the lithiated Si yolk is given by

$$\varepsilon_{\mathrm{Si}} = \frac{1-2\nu_{\mathrm{Li}_x\mathrm{Si}}}{E_{\mathrm{Li}_x\mathrm{Si}}}\sigma_{\mathrm{Si}} \tag{6.1}$$

where $E_{\mathrm{Li}_x\mathrm{Si}}$ and $\nu_{\mathrm{Li}_x\mathrm{Si}}$ are the Young's modulus and Poisson's ratio of the lithiated Si and σ_{Si} is the hydrostatic compression stress in the lithiated Si yolk. The carbon shell is expanded upon full lithiation and the tangential stress σ_t and radial stress σ_r in the carbon shell are given by

$$\sigma_t(r) = \frac{p_i a^3}{2r^3}\frac{2r^3+b^3}{b^3-a^3} \quad (a \le r \le b) \tag{6.2a}$$

$$\sigma_r(r) = \frac{p_i a^3}{r^3}\frac{b^3-r^3}{a^3-b^3} \quad (a \le r \le b) \tag{6.2b}$$

where a and b are the initial inner and outer radii of the carbon shell with $a = R_{\mathrm{C}} - 0.5t$ and $b = R_{\mathrm{C}} + 0.5t$ and p_i is the inner pressure applied on the inner surface of the carbon shell. After the contact between the lithiated Si yolk and the carbon shell at the moment of full lithiation, Newton's Third Law gives

$$p_i = \sigma_{\mathrm{Si}} \frac{R_{\mathrm{Si}}^2}{a^2} \tag{6.3}$$

Substituting Eqs. (6.1) and (6.3) into Eq. (6.2a) leads to

$$\sigma_t(r) = \frac{E_{\mathrm{Li}_x\mathrm{Si}}\varepsilon_{\mathrm{Si}}}{2\left(1-2\nu_{\mathrm{Li}_x\mathrm{Si}}\right)} \frac{aR_{\mathrm{Si}}^2}{b^3-a^3}\left[2+\left(\frac{b}{r}\right)^3\right] \quad (a \le r \le b) \tag{6.4}$$

From Eq. (6.4), we can know that σ_t is a monotonic function of *r* and it reaches the maximum value of $\sigma_t^{\max}$ when $r = a$. Substituting $r = a$ gives the maximum tensile stress $\sigma_t^{\max}$ in the carbon shell as

$$\sigma_t^{\max} = \frac{E_{\mathrm{Li}_x\mathrm{Si}}\varepsilon_{\mathrm{Si}}}{2\left(1-2\nu_{\mathrm{Li}_x\mathrm{Si}}\right)} \frac{R_{\mathrm{Si}}^2}{a^2} \frac{2a^3+b^3}{b^3-a^3} \tag{6.5}$$

According to the Hooke's law, the mechanical strain in the tangential direction ε_t in the carbon shell can be expressed as

$$\varepsilon_t = \frac{1}{E_{\mathrm{C}}}\left(\sigma_t - \nu_{\mathrm{C}}\sigma_t - \nu_{\mathrm{C}}\sigma_r\right) \tag{6.6}$$

where E_{C} and ν_{C} are the Young's modulus and Poisson's ratio of carbon. Substituting Eqs. (6.2a) and (6.2b) into Eq. (6.6) yields

$$\varepsilon_t(r) = \frac{p_i a^3}{E_{\mathrm{C}} r^3}\left[\left(1-\nu_{\mathrm{C}}\right)\frac{2r^3+b^3}{2\left(b^3-a^3\right)} + \nu_{\mathrm{C}}\frac{b^3-r^3}{b^3-a^3}\right] \quad (a \le r \le b) \tag{6.7}$$

Letting $r = a$ in Eq. (6.7), the tangential strain at the inner surface of the carbon shell can be given as

$$\varepsilon_t^{r=a} = \frac{p_i}{E_\mathrm{C}}\left[(1-\nu_\mathrm{C})\frac{2a^3+b^3}{2(b^3-a^3)}+\nu_\mathrm{C}\right] \tag{6.8}$$

A geometrical relationship can be obtained after the contact between the lithiated Si yolk and the carbon shell, which is

$$R_\mathrm{Si}(1+\varepsilon_0-\varepsilon_\mathrm{Si}) = a(1+\varepsilon_t^{r=a}) \tag{6.9}$$

where ε_0 is the linear coefficient of expansion of a free Si nanoparticle upon full lithiation. Here, we take ε_0 as 0.6, corresponding to a volume expansion of ~400% for the Si nanoparticle. Substituting Eqs. (6.1), (6.3) and (6.8) into Eq. (6.9) leads to

$$\frac{R_\mathrm{Si}(1+\varepsilon_0-\varepsilon_\mathrm{Si})-a}{\frac{a}{E_\mathrm{C}}\left[(1-\nu_\mathrm{C})\frac{2a^3+b^3}{2(b^3-a^3)}+\nu_\mathrm{C}\right]} = \frac{R_\mathrm{Si}^2}{a^2}\frac{E_{\mathrm{Li}_x\mathrm{Si}}\varepsilon_\mathrm{Si}}{1-2\nu_{\mathrm{Li}_x\mathrm{Si}}} \tag{6.10}$$

Eq. (6.5) can be transformed to

$$\frac{R_\mathrm{Si}^2}{a^2}\frac{E_{\mathrm{Li}_x\mathrm{Si}}\varepsilon_\mathrm{Si}}{1-2\nu_{\mathrm{Li}_x\mathrm{Si}}} = 2\sigma_t^\mathrm{max}\frac{b^3-a^3}{2a^3+b^3} \tag{6.11}$$

Combination of Eqs. (6.10) and (6.11) gives

$$R_\mathrm{Si}(1+\varepsilon_0-\varepsilon_\mathrm{Si})-a = \frac{\sigma_t^\mathrm{max}a}{E_\mathrm{C}}\left[(1-\nu_\mathrm{C})+\frac{2\nu_\mathrm{C}(b^3-a^3)}{2a^3+b^3}\right] \tag{6.12}$$

The radial strain in the lithiated Si yolk $\varepsilon_{\mathrm{Si}}$ can be eliminated through the combination of Eq. (6.5) and Eq. (6.12), which leads to

$$\begin{aligned}\sigma_t^{\max} = E_{\mathrm{C}}\left(1+\varepsilon_0 - \bar{R}_{\mathrm{C}} + 0.5\bar{t}\right) / \Bigg\{ & \frac{3\bar{R}_{\mathrm{C}}^2\bar{t} + 0.25\bar{t}^3}{3\bar{R}_{\mathrm{C}}^3 - 1.5\bar{R}_{\mathrm{C}}^2\bar{t} + 2.25\bar{R}_{\mathrm{C}}\bar{t}^2 - 0.125\bar{t}^3} \\ & \times \left[2\nu_{\mathrm{C}}\left(\bar{R}_{\mathrm{C}} - 0.5\bar{t}\right) + \frac{2E_{\mathrm{C}}}{E_{\mathrm{Li}_x\mathrm{Si}}}\left(1-2\nu_{\mathrm{Li}_x\mathrm{Si}}\right)\left(\bar{R}_{\mathrm{C}} - 0.5\bar{t}\right)^2 \right] + \left(1-\nu_{\mathrm{C}}\right)\left(\bar{R}_{\mathrm{C}} - 0.5\bar{t}\right) \Bigg\}\end{aligned} \tag{6.13}$$

where $\bar{R}_{\mathrm{C}} = R_{\mathrm{C}} / R_{\mathrm{Si}}$ and $\bar{t} = t / R_{\mathrm{Si}}$. Combination of Eq. (6.5) and Eq. (6.13) leads to

$$\begin{aligned}\varepsilon_{\mathrm{Si}} = {} & 2\left(1-2\nu_{\mathrm{Li}_x\mathrm{Si}}\right)\left(1+\varepsilon_0 - \bar{R}_{\mathrm{C}} + 0.5\bar{t}\right)\left(\bar{R}_{\mathrm{C}} - 0.5\bar{t}\right)^2 \\ & \div \left[\frac{2E_{\mathrm{Li}_x\mathrm{Si}}\nu_{\mathrm{C}}}{E_{\mathrm{C}}}\left(\bar{R}_{\mathrm{C}} - 0.5\bar{t}\right) + 2\left(1-2\nu_{\mathrm{Li}_x\mathrm{Si}}\right)\left(\bar{R}_{\mathrm{C}} - 0.5\bar{t}\right)^2 \right. \\ & \left. + \frac{E_{\mathrm{Li}_x\mathrm{Si}}}{E_{\mathrm{C}}}\left(1-\nu_{\mathrm{C}}\right)\left(\bar{R}_{\mathrm{C}} - 0.5\bar{t}\right) \frac{3\bar{R}_{\mathrm{C}}^3 - 1.5\bar{R}_{\mathrm{C}}^2\bar{t} + 2.25\bar{R}_{\mathrm{C}}\bar{t}^2 - 0.125\bar{t}^3}{3\bar{R}_{\mathrm{C}}^2\bar{t} + 0.25\bar{t}^3} \right]\end{aligned} \tag{6.14}$$

According to the maximum tensile stress criterion [180], the carbon shell will not be fractured if the maximum tensile stress $\sigma_t^{\max}$ is lower than the fracture strength σ_{f} of the amorphous carbon. By taking $\sigma_t^{\max} \le \sigma_{\mathrm{f}}$, the critical conditions under which no fracture of the carbon shell occurs can be obtained. The mechanical properties of carbon and $\mathrm{Li}_x\mathrm{Si}$ are taken as the values in Table 1 of Section 5.4.1. If we take $2\,\mathrm{GPa} \le \sigma_{\mathrm{f}} \le 6\,\mathrm{GPa}$, such critical conditions can be plotted by the two curves on the $\bar{R}_{\mathrm{C}}$-$\bar{t}$ plane as shown in Fig. 6.2. It can be predicted that the carbon shell will not be fractured after full lithiation if the geometrical dimensions $\bar{R}_{\mathrm{C}}$ and $\bar{t}$ are selected above the critical curves. Otherwise the carbon shell will be fractured. By comparing the theoretical predictions (the solid curves) with the experimental observations (the scattering symbols), it can be summarized that all the fractured Si@void@C NPs have geometrical dimensions below the critical curve for $\sigma_{\mathrm{f}} = 6\,\mathrm{GPa}$ while the nanoparticles remain continuous with geometrical dimensions above the critical curve for $\sigma_{\mathrm{f}} = 2\,\mathrm{GPa}$. For the nanoparticles locating in the marginal zone between the two critical curves, whether or not the fracture occurs is random. This means that the fracture strength σ_{f} of the amorphous carbon shell falls in the range of 2 – 6 GPa, which is consistent with the parameters reported in literature [216]. In order to ensure the structural integrity of the Si@void@C NPs, as a conservative estimation, the geometrical dimensions ($\bar{R}_{\mathrm{C}}$ and $\bar{t}$) of the nanoparticles should be selected above the critical curve of $\sigma_{\mathrm{f}} = 2\,\mathrm{GPa}$ so that all the Si@void@C NPs will not be fractured during lithiation.

6.3. Capacity optimization

In addition to obtain the structural integrity during lithiation, the theoretical capacity of the Si@void@C NPs is another factor which influences the electrochemical performance of the nanoparticle electrode materials. The theoretical capacity of the Si@void@C NP comes from both Si yolk and carbon shell and can be estimated based on the theoretical capacities, mass ratios and volume expansion of both Si and carbon. The volume change of a free Si yolk at the moment of full lithiation ΔV_1 is given by

$$\Delta V_1 = V_0[(1+\varepsilon_0)^3 - 1] \tag{6.15}$$

where V_0 is the initial volume of the Si yolk. For the Si@void@C NP, if the volume expansion of the Si yolk is constrained by the carbon shell during lithiation, the volume change of the constrained Si yolk ΔV_2 can be expressed as

$$\Delta V_2 = V_0[(1+\varepsilon_0 - \varepsilon_{\mathrm{Si}})^3 - 1] \tag{6.16}$$

The theoretical capacity contributed by the constrained Si yolk is assumed to be proportional to the volume change of the Si yolk. Thus the capacity of the Si yolk C_{Yolk} upon full lithiation is given by

$$C_{\mathrm{Yolk}} = C_{\mathrm{Si}} \frac{m_{\mathrm{Si}}}{m_{\mathrm{Si}} + m_{\mathrm{C}}} \frac{\Delta V_2}{\Delta V_1} \tag{6.17}$$

where C_{Si} is the theoretical capacity (4200 mA h g^{-1}) of Si and m_{Si} and m_{C} are the mass of the Si yolk and the carbon shell respectively. The carbon shell is assumed to be fully lithiated and the theoretical capacity contributed by the carbon shell C_{Shell} is given by

$$C_{\mathrm{Shell}} = C_{\mathrm{C}} \frac{m_{\mathrm{C}}}{m_{\mathrm{Si}} + m_{\mathrm{C}}} \tag{6.18}$$

where C_{C} denotes the theoretical capacity (372 mA h g^{-1}) of carbon. The mass of the Si yolk and the carbon shell can be expressed as

$$m_{\mathrm{Si}} = \frac{4}{3}\pi R_{\mathrm{Si}}^3 \rho_{\mathrm{Si}} \tag{6.19a}$$

$$m_{\mathrm{C}} = \left[\frac{4}{3}\pi\left(R_{\mathrm{C}} + 0.5t\right)^3 - \frac{4}{3}\pi\left(R_{\mathrm{C}} - 0.5t\right)^3\right]\rho_{\mathrm{C}} \tag{6.19b}$$

where ρ_{Si} (2.33 g cm^{-3}) and ρ_{C} (2.25 g cm^{-3}) are the densities of Si and carbon, respectively [202]. The summation of C_{Yolk} and C_{Shell} is equal to total theoretical capacity C of the Si@void@C NP which is derived as

$$C=\frac{C_{\mathrm{Si}}}{1+\bar{\rho}\left(3\bar{R}_{\mathrm{C}}^{2}\bar{t}+0.25\bar{t}^{3}\right)}\frac{\left(1+\varepsilon_0-\varepsilon_{\mathrm{Si}}\right)^3-1}{\left(1+\varepsilon_0\right)^3-1}+\frac{C_{\mathrm{C}}\bar{\rho}\left(3\bar{R}_{\mathrm{C}}^{2}\bar{t}+0.25\bar{t}^{3}\right)}{1+\bar{\rho}\left(3\bar{R}_{\mathrm{C}}^{2}\bar{t}+0.25\bar{t}^{3}\right)} \tag{6.20}$$

where $\bar{\rho}=\rho_{\mathrm{C}}/\rho_{\mathrm{Si}}$. By substituting the mechanical properties and theoretical capacities of the materials into the Eq. (6.20), the capacity C can be plotted as a function of the geometrical dimensions $\bar{R}_{\mathrm{C}}$ and $\bar{t}$ as shown in Fig. 6.4.

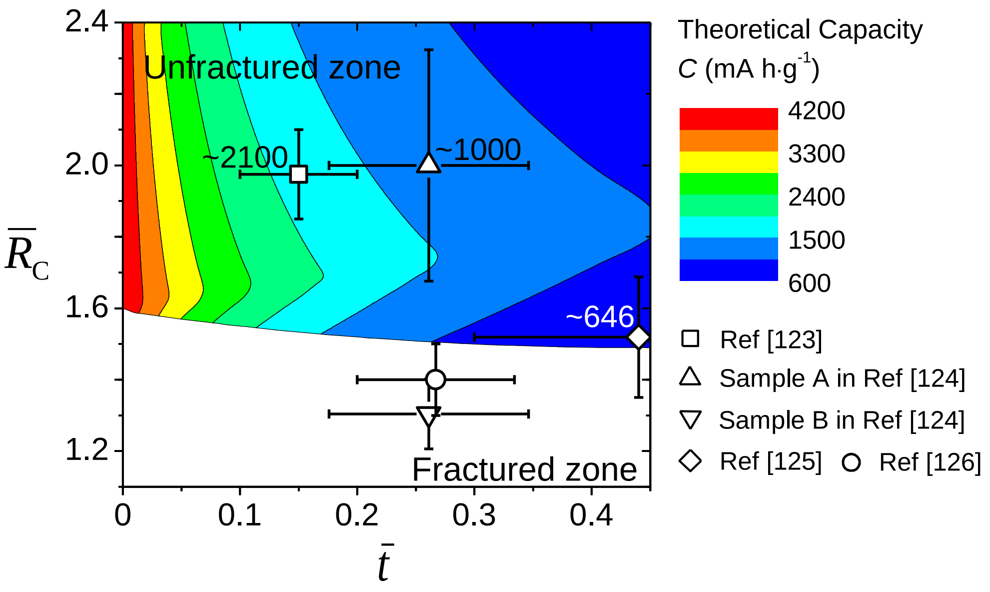

Figure 6.4. Optimal design guideline for the yolk-shell carbon-coated Si nanoparticle electrode materials showing the dependence of fracture and theoretical capacity on geometrical dimensions $\bar{R}_{\mathrm{C}}$ and $\bar{t}$. The hollow symbols represent the distribution of geometrical dimensions of the Si@void@C NPs in the literature [123-126] and sample A and B refer to the “YS Si@50*m*C” and “YS Si@10*m*C” in ref. [124], respectively.

Fig. 6.4 gives a design guideline for the Si@void@C NP electrode materials to achieve structure integrity and high capacity at the same time. The nanoparticles with geometrical dimensions above the critical curve of $\sigma_{\mathrm{f}} = 2\,\mathrm{GPa}$ can remain continuous and their theoretical capacity can be predicted from the guideline, which is illustrated by the contours. Generally, for given diameter of the Si yolk, smaller thickness of carbon shell leads to higher capacity and the capacity can be further optimized by selecting an optimal radius for the carbon shell.

It might be interesting to compare the estimated capacities from this map with the results reported in literatures [123-126]. The ranges of the geometrical dimensions of the nanoparticles in these literatures are marked by the symbols with error bars in Fig. 6.4. Among all the products of the Si@void@C NP electrode materials, three groups of them have geometrical dimensions locating in the unfractured region, indicating their stable structure integrity during electrochemical cycling. According to Eq. (6.20), their capacities are estimated to be around 1546-2169, 1135-1631 and 535-972 mA h g^{-1} as shown in Fig. 6.4 which agree well with the experimentally measured capacities of ~2100, ~1000 and ~646 mA h g^{-1}, respectively. On the contrary, the other two groups of the Si@void@C NPs have dimensions in the fractured region. This indicates that they may not have stable cycling performance since the nanoparticles are easier to be fractured during lithiation. This prediction is also confirmed by the quick drop of their measured capacities during electrochemical cycling measurements.

In this chapter, *in situ* lithiation was conducted on the yolk-shell carbon-coated Si nanoparticle electrode materials. It was found that the fracture of the nanoparticles upon lithiation was dependent on the geometrical dimensions, such as the radius and thickness of the carbon shell and the radius of the Si yolk. Rigorous theoretical modeling was established to explain the geometrical dimensions-dependent fracture of the carbon shell and provide a design guideline to obtain structural integrity and high capacity for the nanoparticle electrode materials. By the end of this chapter, the theoretical modeling was applied to predict the fracture occurrence and capacity of the yolk-shell carbon-coated Si nanoparticle electrode materials in the literatures. The theoretical prediction was confirmed by the experimental results and observations reported in literatures. These experimental and theoretical approaches and the design guideline should be of significant value to guide the design and synthesis of the yolk-shell structured electrode materials for lithium ion batteries.

Chapter 7. Silicon-coated copper nanowire electrode

Optimal design guidelines have been proposed to maintain the structural integrity and maximize the capacity for the core-shell nanostructured electrode materials in previous chapters. In addition to the fracture problems of the high-capacity electrode materials, loss of structural integrity may result from the interfacial failure of the electrode materials from the current collector, induced by the large volume change of electrodes during cycling. Such interfacial failure leads to the loss of electronic conductivity and the decayed cycling performance of the lithium ion batteries. In order to improve the interfacial strength between the electrode materials and the current collector, modification of the current collector has been widely studied, as discussed in Section 2.4. By using the Si-coated copper (Cu) nanowire array current collector, the electrochemical performance of the lithium ion battery has been significantly improved to achieve ~2000 cycles with a reversible capacity of more than 1000 mA h g^{-1}. Such improvement is probably due to enhanced structural stability of the Si-coated Cu nanowire array structure by the increased adhesion and interfacial strength between the Si shell and the Cu core. However, it is still unclear about how the lithiation and delithiation occur in the Si-coated Cu core-shell nanowire electrode materials, which is the premise to explain the enhancement of structural stability. Besides, it may be interesting to study the mechanism of fracture, interfacial and fatigue failure of the core-shell structured nanowire electrode.

In this chapter, the Cu nanowires were synthesized by hydrothermal methods [175] and the Si shell was coated on the nanowires through magnetron sputtering technique [155,160,171,176]. The *in situ* lithiation and delithiation were conducted on the nanowires to reveal the mechanism of insertion and extraction of lithium ions and the reason of achieving high structural stability for the Si-coated Cu nanowire electrode materials.

7.1. Synthesis and characterization

The 120 g NaOH powder was firstly dissolved in 200 mL deionized water under stirring and cooled down to room temperature. Later on, 10 mL 0.1M $Cu(NO_3)_2$ solution, 3 mL absolute Ethylenediamine (EDA) and 0.25 mL N_2H_4 (35 wt%) were added into the above solution. The mixture of the solution was then moved into a water bath at 80 ˚C for 1 hour. The reaction product was rinsed by 3 wt% N_2H_4 solution and collected through centrifugal machine at 10000 rpm of 6 min. Subsequently, the Cu nanowires were saved in the solution of 3 wt% N_2H_4 for the characterization of morphology and components and the following magnetron sputtering of Si shell. Fig. 7.1 shows the flow chart of the synthesis process for the Si-coated Cu nanowires.

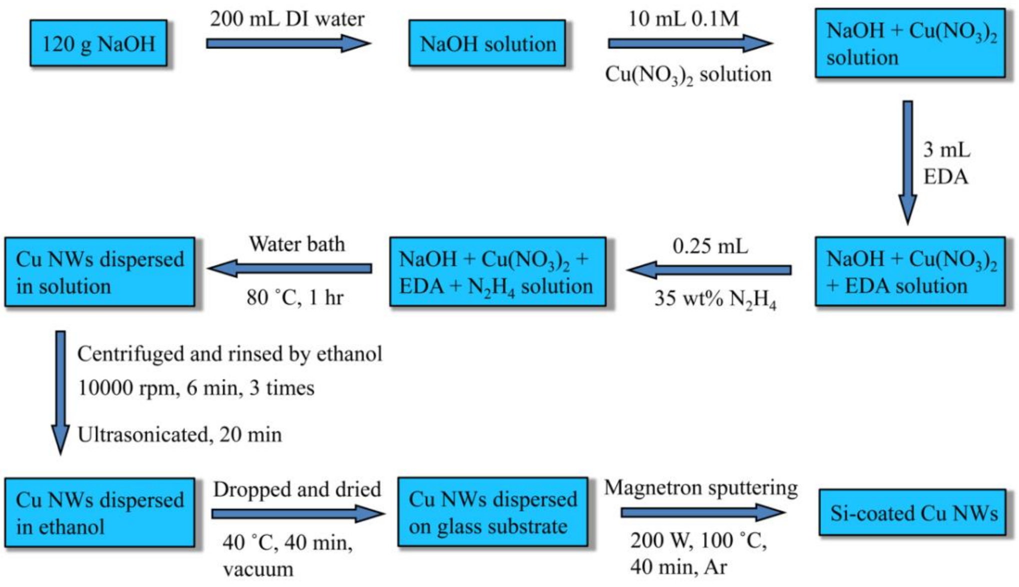

Figure 7.1. Flow chart for the synthesis of the Si-coated Cu nanowires.

The Cu nanowire reaction product was later on centrifuged and rinsed by absolute ethanol at 10000 rpm of 6 min for 3 times. The segregated Cu nanowires were dispersed in absolute ethanol and ultrasonicated for 20 min. After dispersed uniformly in the absolute ethanol, the Cu nanowires were dropped onto the glass substrate, which was subsequently moved into the vacuum oven and dried at 40 ˚C for 40 min. The dried Cu nanowires were later on moved into the magnetron sputtering machine for coating of Si at the power of 200W and temperature of 100 ˚C for 40 min in the atmosphere of argon (Ar). The pre-sputtering procedure was conducted by gradually increasing power to 200 W with the rate of 40 W per 15 seconds. After sputtering, the power was decreased by the rate of 40 W per 10 seconds. Finally, the Si-coated Cu nanowires were synthesized.

The morphology of the Cu nanowires is shown in Fig. 7.2a, in which the diameter of the nanowire is around 70 nm and the length is more than 860 nm, indicating the high aspect ratio of at least 10. The crystalline structure of the Cu nanowire is confirmed by the high-resolution TEM image in Fig. 7.2c and the selected area electron diffraction pattern in Fig. 7.2e. The Si-coated Cu nanowire is shown in Fig. 7.2b and the amorphous Si shell and the crystalline Cu core with an interface in between can be clearly seen by the high-resolution TEM image in Fig. 7.2d. The circular diffraction rings in the Fig. 7.2f are intensified, confirming the existence of the amorphous phase, which is the amorphous Si shell in the Si-coated Cu nanowire.

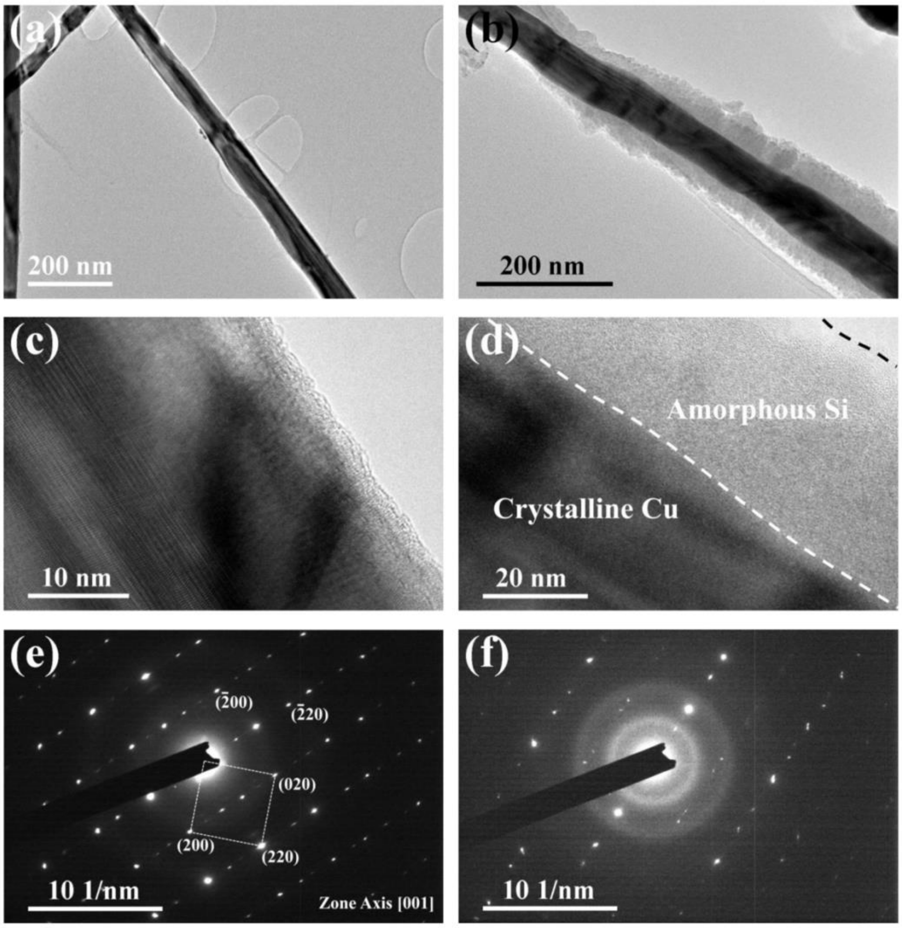

Figure 7.2. TEM images showing the morphologies of (a) Cu nanowire and (b) Si-coated Cu nanowire. High-resolution TEM images of (c) Cu nanowire and (d) Si-coated Cu nanowire. Selected area electron diffraction patterns of (e) Cu nanowire and (f) Si-coated Cu nanowire.

7.2. Growth of lithium nanostructures during delithiation

In order to investigate the lithiation and delithiation mechanism of the Si-coated Cu nanowire electrode materials, *in situ* lithiation and delithiation were conducted. Fig. 7.3 shows the schematic of the setup for the nanoscale half-cell with the nanowires as the electrode material and the lithium metal as the reference electrode material inside TEM. The Si-coated Cu nanowires were attached on the golden rod with silver paster and mounted on the TEM holder. The lithium metal was attached on the tungsten rod in the glovebox. During the transferring of lithium metal from the glovebox to the TEM holder in the air, the Li_2O layer formed and served as the solid electrolyte. The holder was subsequently moved into the TEM and the TEM chamber was vacuumed for the *in situ* lithiation and delithiation.

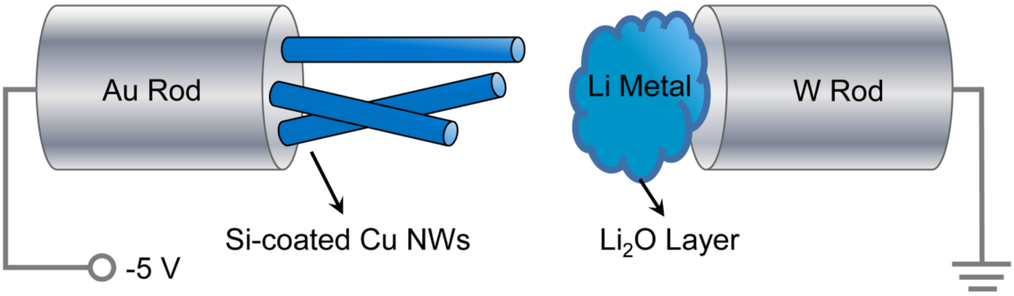

Figure 7.3. Schematic of the setup for the *in situ* lithiation and delithiation of the Si-coated Cu nanowire electrode materials.

The initial morphology of a Si-coated Cu nanowire is shown in Fig. 7.4a. It can be seen that the nanowire electrode is consisted of the Cu core and the Si shell, which are marked by the annotation in Fig. 7.4a. After contacting the nanowire electrode with the lithium source at the left bottom corner and applying a voltage of –5 V, the Si shell was lithiated with a volume expansion, as shown in Figs. 7.4b-c. It can be found that the lithiation proceeds from the end of the lithium source to the other end with a proceeding volume expansion along the nanowire. Fig. 7.4c shows the full lithiation state of the nanowire after lithiation of 240 s, in which the volume expansion of the Si shell can be clearly seen. Figs. 7.4d-f show the snapshots of delithiation process, in which the volume contraction occurs concurrently along the nanowire. Unexpectedly, the lithium nanostructures were extracted from the delithiated Si shell upon a positive voltage was applied. Much more lithium nanostructures appeared upon further delithiation, as shown from Figs. 7.4e-f. Fig. 7.4f shows the final state of delithiation in which a large amount of lithium nanostructures can be seen, as indicated by the white arrows. Such lithium nanostructures disappeared randomly when exposed to the electron beam inside the TEM. During the second lithiation process, as shown in Fig.7.4g-i, the volume of the Si shell expanded again due to the insertion of lithium ions into the Si shell and the formation of Li_xSi. The lithium nanostructures on the surface of the shell disappeared after the negative voltage was applied. Such lithium nanostructures may be either absorbed by the Si shell to form Li_xSi or eliminated due to the exposure under electron beam. After full lithiation, the volume of the Si shell was expanded again, as shown in Fig. 7.4i.

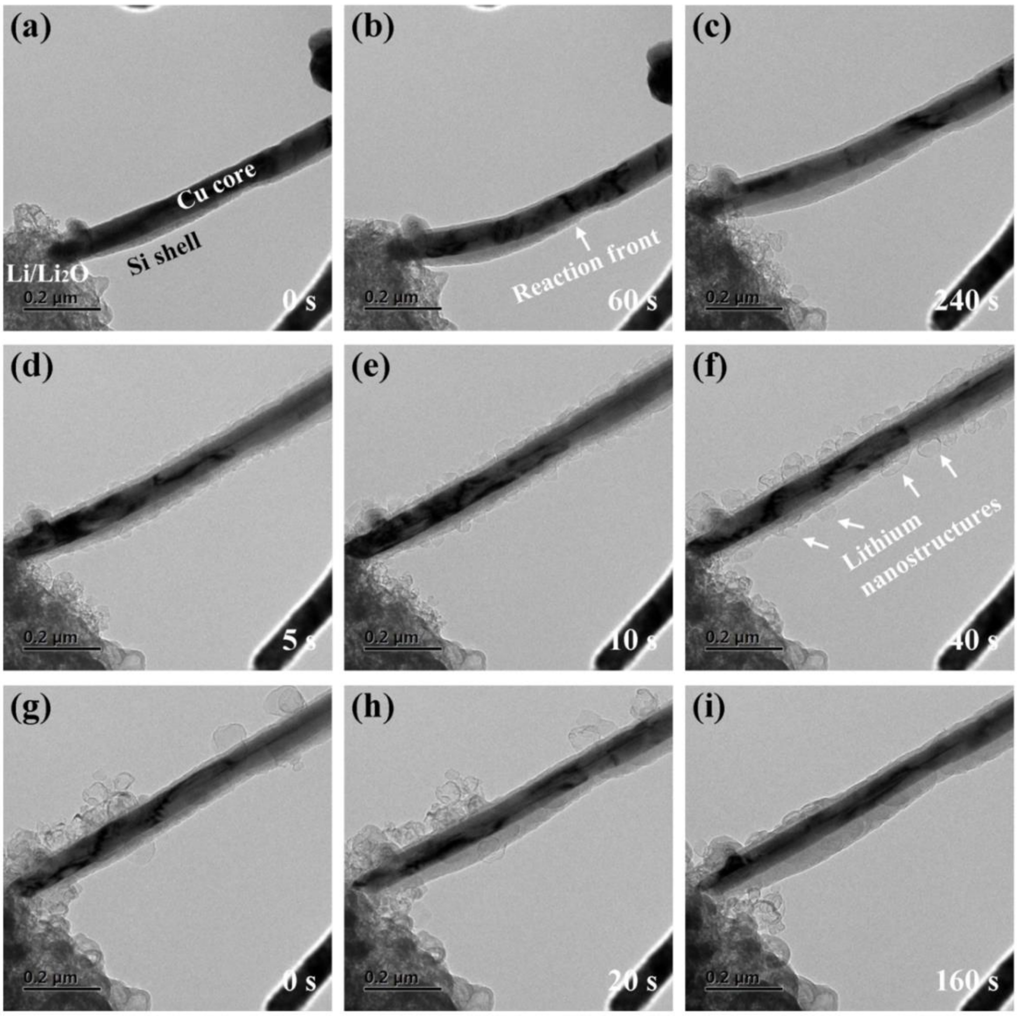

Figure 7.4. Snapshots of the *in situ* TEM characterization for (a-c) first lithiation, (d-f) first delithiation and (g-i) second lithiation processes of the Si-coated Cu nanowire electrode.

The nanostructured lithium, such as the dendritic and mossy lithium, has been observed to form on the surface of lithium electrode materials during electrochemical cycling [217-223] and the growth mechanism was studied by several theoretical works [224-226]. It has been found that the formation of lithium dendrite or moss is induced and affected by several factors, including the surface morphology of the electrode, the current density, the gradient of ionic concentration in the liquid electrolyte, etc. For example, in comparison to the electrode materials with smooth surface, the dendritic lithium is prone to growing on the roughened surface or in the vicinity of the surface defects where the current density varies on the surface of the electrode materials and is intensified at these positions [222]. Besides, by increasing the current density, the morphology of the lithium nanostructures evolve from mossy-like to dendritic-like, probably due to the increased strength of electric field at the specific reaction spots [218,219,221]. At low current density, the surface morphology plays a major role in the growth of the lithium nano- and microstructures while at high current density, the gradient of ionic concentration in the electrolyte becomes more important [220].

It can be seen from Fig. 7.4a that the thickness of the Si shell varies a little along the axial direction. During the delithiation process, the lithium nanostructures tend to grow on the non-uniform (or roughened) surface of the Si shell. In addition, since Cu has low resistance and high electronic conductivity, the current density in the Si-coated Cu nanowire electrode becomes higher than that in the bare Si nanostructured electrode. Such high current density probably results in the formation of lithium nanostructures on the surface of Si shell, as observed from the *in situ* delithiation process in Figs. 7.4d-e. Furthermore, due to the lower current density in the bare Si nanostructured electrode, no formation of the lithium nanostructures was observed during *in situ* lithiation/delithiation processes as reported in literatures [47,102]. Besides, even though carbon materials are able to increase the electron conductivity of the Si electrode materials, no lithium nanostructure was found during the *in situ* cycling tests in neither our own studies (e.g. carbon/Si nanoparticle electrodes) nor literatures [92,120]. Therefore, the Cu core probably plays an important role in increasing the current density so that the lithium nanostructures can form during delithiation, in addition to effect of the non-uniform/roughened Si shell structure. In order to confirm these hypotheses, further investigations should be taken to study the lithiation and delithiation processes of the bare Si nanowire and Si-coated carbon nanowire electrode materials and compare the results with the Si-coated Cu nanowire electrode materials.

It has been reported that the formation of such lithium nanostructures may impale the separator and cause the short circuit, leading to the failure and potential safety issues for lithium ion batteries. Our experimental results show that the lithium nanostructures probably induce the fracture of the Si shell during the *in situ* delithiation process. Fig. 7.5 shows the snapshots of the fracture occurrence of the Si shell in a Si-coated Cu nanowire electrode during the first delithiation process. It can be seen from Fig. 7.5a that the lithium nanostructures grow on the surface of the Si shell at the beginning of delithiation, as indicated by the white arrows. After continuing delithiation of 11 s, some bulk lithium nanostructures form at several locations, as shown by the yellow arrows in Fig. 7.5b. One second later, parts of the bulk lithium nanostructures disappear and probably form Li_xSi with the contiguous delithiated Si, inducing a large volume expansion and fracture of the Si shell, as indicated by the red arrows in Fig. 7.5c. The experimental observation shows that such lithium nanostructures may be disadvantageous to structural integrity due to the lithiation-induced fracture of the Si shell during the delithiation process.

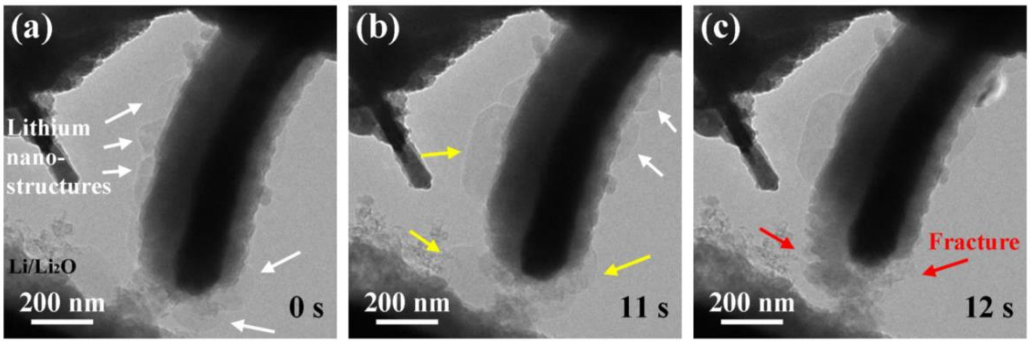

Figure 7.5. Snapshots of the fracture of Si shell in the Si-coated Cu nanowire electrode during 1st delithiation.

Similar phenomenon has also been observed during the 10th delithiation process of a Si-coated Cu nanowire, as shown in Fig. 7.6. From Figs. 7.6a-c, it can be seen that the volume of the shell is contracted during delithiation and the lithium nanostructures form on the surface of the shell, as indicated by the black arrows. A huge lithium nanostructure forms after delithiation of 98 s, as indicated by the yellow arrow in Fig. 7.6c, and one second later, the lithium nanostructures probably react with the contiguous delithiated Si shell and form Li_xSi again, leading to a sudden volume expansion and fracture of the Si shell, as shown by the red arrow in Fig. 7.6d.

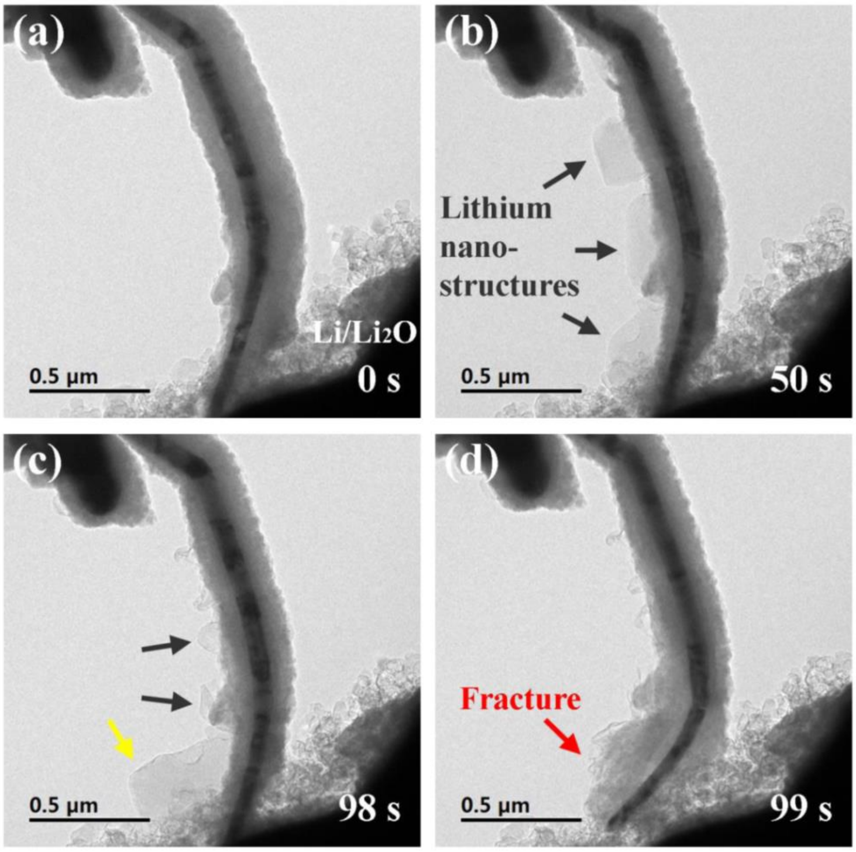

Figure 7.6. Snapshots of the fracture of Si shell in a Si-coated Cu nanowire electrode during 10th delithiation.

7.3. Stable cycling performance

In order to investigate the reason for the long cycle life of the Si-coated Cu nanowire electrode materials, the nanowire electrodes were lithiated and delithiated for up to 11 cycles, as shown in Figs. 7.7. Figs. 7.7a, c and e show the states of full lithiation of one Si-coated Cu nanowire electrode after the 1st, 6th and 11th lithiation, respectively. In comparison with Fig. 7.7a, larger volume expansion of the nanowire can be observed at the states of 6th and 11th lithiation, as shown in Figs. 7.7c and e. Such high volume change was not observed for the 1st lithiation, probably due to the partial lithiation of the nanowire during the first lithiation process. The nanowire electrode was bent, as shown in in Figs.

7.7c and e, due to the unbalanced stress state in the lithiated Si shell with non-uniform thickness.

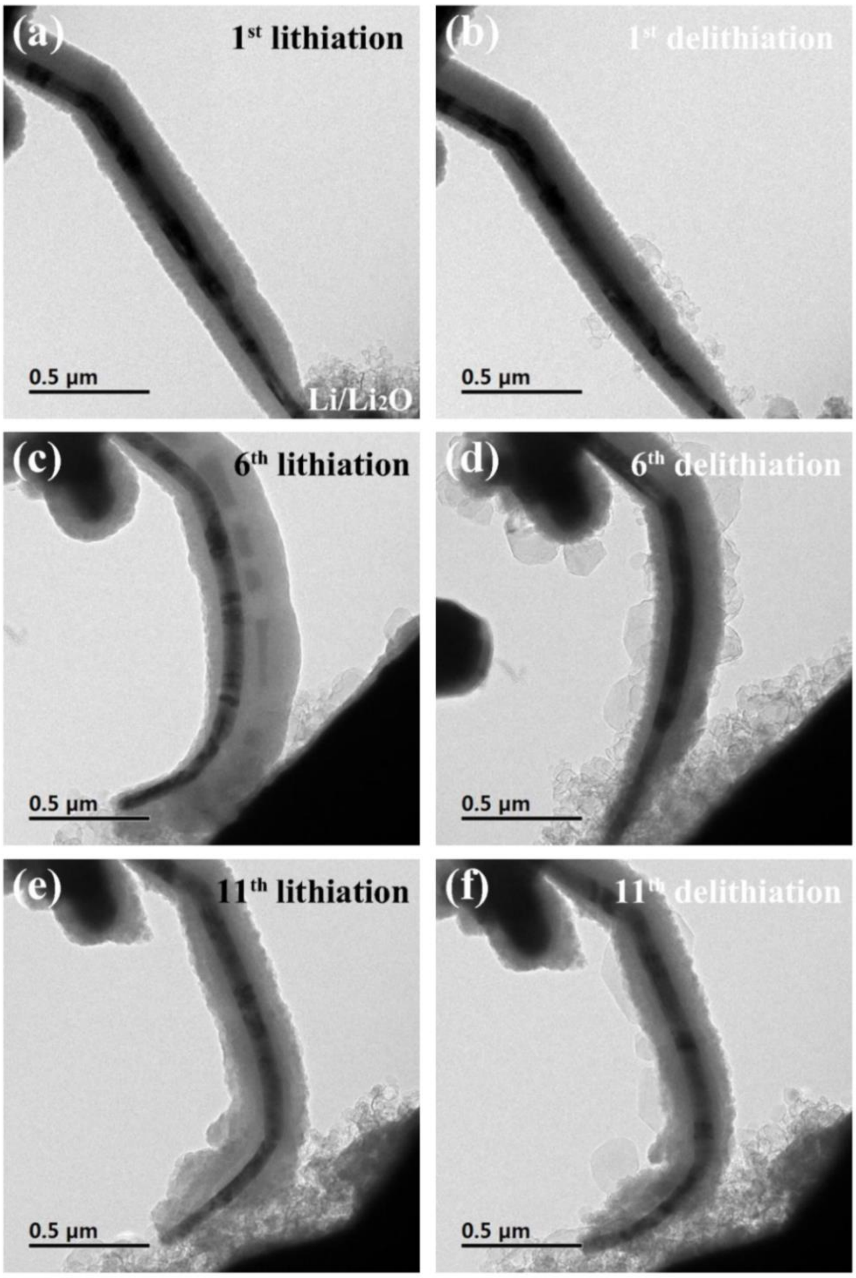

Figure 7.7. Snapshots of the *in situ* lithiation and delithiation cycling tests of the Si-coated Cu nanowire electrode.

During delithiation, the volume of the Si shell was contracted, as shown in Figs. 7.7b, d and f for the 1st, 6th and 11th cycle, respectively. In addition, the lithium nanostructures were extracted during the delithiation process. Even though fracture occurred in the delithiated Si shell during the 10th delithiation, as shown in Fig. 7.6d for the nanowire electrode, and the surface of the Si shell became rough after 11 cycles, the Si shell still adhered well with the Cu core, indicating the strong adhesion and interfacial strength between the Si shell and the Cu core. Such high adhesion and interfacial strength leads to the good structural stability and promising stable cycle life of the Si-coated Cu nanowire electrode materials, indicating the advantages of the Cu nanowire array current collector for lithium ion batteries.

In this chapter, we studied the lithiation and delithiation processes of the Si-coated Cu nanowire electrode materials. The crystalline Cu nanowires were firstly synthesized through hydrothermal method and the amorphous Si shell was coated on the Cu nanowires by using magnetron sputtering technique. During *in situ* lithiation, the nanowire was lithiated from one end to the other with volume expansion. The lithium nanostructures formed and grew on the surface of the delithiated Si shell during the delithiation process. The formation of the lithium nanostructures was probably due to the non-uniform surface of the Si shell and the high current density in the nanowire. Such lithium nanostructures were observed to react with the delithiated Si shell and form Li_xSi again, leading to the volume expansion and fracture of the delithiated Si shell during delithiation. Even though fracture occurred during delithiation, the interfacial bonding between the Si shell and Cu core could be still stable for at least 11 cycles, indicating strong adhesion between the Si and Cu.

Further lithiation and delithiation experiments should be conducted on the control cases, including the bare Si nanowire and the Si-coated carbon nanowire electrodes, to find out the mechanism for the growth of the lithium nanostructures. Theoretical and simulation approaches should also be adopted to propose methods to control the growth of the lithium nanostructures and find an optimal design method to avoid the fracture. This study should be of great importance for the design of the core-shell structured electrode materials with high-capacity electrode material as the shell for lithium ion batteries.

Chapter 8. Conclusions and discussions

We systematically studied the lithiation/delithiation and fracture mechanisms of the core-shell nanostructured electrode materials and proposed optimal design guidelines for the electrode materials by using both experimental and theoretical methods. The electrode materials included the carbon-coated SnO_2 nanowire, the carbon-coated Si nanoparticle, the yolk-shell carbon-coated Si nanoparticle and the Si-coated Cu nanowire. In this chapter, we will discuss and summarize the experimental observations and theoretical results, and outline the future works derived from the results and predictions in the previous chapters.

8.1. Conclusions and discussions

SnO_2 and Si nanomaterials, as high-capacity anode materials, undergo large volume change during electrochemical cycling. Such large volume change induces the fracture and pulverization of the electrode materials and the capacity fading and short cycle life of the lithium ion batteries. In order to improve the electrochemical performance, carbon coating technique has been utilized to constrain the volume expansion and avoid the fracture of the SnO_2 and Si nanostructured electrode materials. Carbon coating can increase the electronic conductivity of the electrode materials. Besides, the diffusivity of the lithium ions can also be increased. If the carbon coating is not cracked, the solid electrolyte interface on the surface of the coating can be stable and the electrochemical performance of the electrode materials can be improved. Therefore, the carbon-coated nanoparticle/nanowire electrode materials show a longer and more stable cycle life than the bare nanoparticle/nanowire electrode materials. On the other hand, the carbon shell should be used as little as possible to achieve the highest theoretical capacity for the core-shell nanostructured electrode materials due to the lower capacity of carbon than that of SnO_2 or Si. Hence, both experimental and theoretical approaches were adopted to study the lithiation/delithiation and fracture mechanisms and propose optimal design guidelines for the electrode materials. In addition to the fracture problems, the electrochemical performance of the electrode materials is also dependent on the structural integrity between the electrode material and the current collector, such as the interfacial and fatigue strength during cycling. Therefore, the structural integrity studies were also conducted on the Si-coated Cu nanowire electrode materials with the high-capacity electrode materials as the shell to instruct the design for lithium ion batteries. The key findings about the four kinds of electrode materials are summarized as following.

- We studied the fracture mechanism of the carbon shell on the carbon-coated SnO_2 nanowire electrode material based on the theory of diffusion and fracture mechanics. A critical thickness of the carbon shell, ~9 nm, was found so that the carbon shell can maintain continuous and the composite material can achieve the maximum capacity upon lithiation. The lithium ion concentration was calculated by theoretical modeling for high-capacity core-shell nanowire electrode materials. The deformation and stress states in the shell and core of the nanowire electrode can be determined by analogously treating the lithiation-induced expansion as thermal expansion by using finite element simulation.

- We synthesized the carbon shell on the Si nanoparticles by using hydrothermal method. We found that the carbon shell may expedite the fracture of the carbon-coated Si nanoparticles through *in situ* lithiation technique. That is, the carbon-coated Si nanoparticle was fractured upon lithiation even though the diameter of the crystalline Si core was far smaller than the recognized safety threshold size (~150 nm). The fracture mechanism was analyzed by finite element simulation based on the theory of fracture mechanics. It was found that the crack was initiated in the carbon shell and propagated into the lithiated Si core due to the elevated driving force caused by material's inhomogeneity between the shell and the core, leading to the fracture of the carbon-coated Si nanoparticle. A critical ratio of D/t (D for the diameter of the Si core and t for thickness of carbon shell) was proposed to prevent the fracture and maximize the capacity for the carbon-coated Si nanoparticle electrode materials.
- We studied the fracture mechanism of the yolk-shell carbon-coated Si nanoparticle electrode materials by using *in situ* lithiation technique and theoretical modeling based on theory of elasticity and fracture mechanics. The *in situ* lithiation results showed that the yolk-shell carbon-coated Si nanoparticles tend to be fractured, depending on the characteristic structural features such as the diameter of the Si yolk, the thickness of the carbon shell and the interspace between the yolk and the shell. That is, for given diameter of Si yolk, the nanoparticles are subject

to fracture with thinner carbon shell and smaller yolk-shell interspace. A mechanics-based theoretical model is conducted to analyze the stress development in the carbon shell and the theoretical capacity of the yolk-shell carbon-coated Si nanoparticle. A diagram for structural optimization was obtained so that the electrode materials can be designed to avoid the fracture and achieve the maximum capacity.

- We studied the Si-coated Cu nanowire electrode materials through *in situ* lithiation characterization. The Si-coated Cu nanowires were synthesized by hydrothermal method and magnetron sputtering technique. It was found that the lithium nanostructures grew on the surface of the Si shell during delithiation and such lithium nanostructures might react with the Si shell and form Li_xSi again. If bulk lithium nanostructures formed on the surface of the shell, a large volume expansion would occur, leading to the fracture of the Si shell. Further cycling tests of the nanowire electrode materials showed that even though fracture occurred, the structural integrity could be maintained as long as the interfacial adhesion between the Si shell and the Cu core remained strong enough. The *in situ* lithiation experimental results indicated that the electrochemical performance can be improved by designing high-capacity electrode materials as the shell and the supporting materials as the core.

It should be pointed out that the studies in this thesis are mainly focused on the fracture of individual nanowire and nanoparticle electrodes. The safety and the cycling performance of the overall electrode materials are dependent on many other factors, such as the fracture of the overall electrode materials, the stability of the solid electrolyte interface, the interfacial strength between the electrode materials and the current collector, etc. Even though the volume of the individual nanowire or nanoparticle has been constrained by the coating technique, the volume of the overall electrode materials can still be expanded, probably leading to the fracture of the electrode materials and the delamination between the electrodes and current collector.

Besides, for the carbon-coated SnO_2 nanowire, the fracture is purely dependent on a critical value (thickness of carbon shell), while the fracture of the carbon-coated Si and the yolk-shell carbon-coated Si nanoparticles is dependent on the geometrical ratios. Such difference is mainly due to the different lithiation mechanisms in SnO_2 and Si anode materials. For SnO_2 nanowire, there is a transition region in which the nanowire is partially lithiated. The maximum tensile stress is a sum of the axial tensile stress and the bending stress in the carbon shell near the reaction front. That is, the bending stress also contributes to the fracture occurrence of the carbon shell, in addition to the axial tensile stress in the carbon shell caused by the elongation of the nanowire. However, for the Si anode material, the fracture of the carbon shell is only due to the hoop tensile stress in the carbon shell, caused by the volume expansion of the Si core. In addition, for the SnO_2 anode, we only tested the nanowires with diameter from 30 to 80 nm. There could be a minor trend showing that the fracture of the carbon shell is dependent on SnO_2 core diameter. But carbon shell thickness has much more significant effect on the fracture than the SnO_2 core diameter.

The mechanical properties, including the fracture strength, of carbon shell are different due to the different synthesis methods. For the carbon-coated SnO_2 nanowire, glucose was used as carbon source and the synthesis process included heating at 190 ˚C for 12 hours in sealed autoclave and annealing at 450 ˚C for 2 hours in air. For the carbon-coated Si nanoparticle, sucrose was used as carbon source and the mixture was stirred at 70 ˚C for 3 hours and dried in vacuum oven at 120 ˚C for 8 hours before heated at 800 ˚C for 2 hours in the nitrogen atmosphere. For the yolk-shell carbon-coated Si nanoparticle, the resorcinol-formaldehyde resin was used as carbon source and the mixture was heated at 400 ˚C for 2 hours and then at 800 ˚C for 2 hours in the nitrogen atmosphere. This is also why the fracture strength of the carbon shell is a critical value for carbon-coated SnO_2 nanowire while there is a range for the fracture strength of the nanoparticle electrode materials.

In summary, four kinds of core-shell nanostructured electrode materials were studied through comprehensive experimental and/or theoretical approaches. The synthesis and characterization methods and the *in situ* lithiation/delithiation techniques should be of important value for studying the mechanical and electrochemical properties of the electrode materials for lithium ion batteries. The theoretical modeling, based on the equation of diffusion, theory of elasticity and fracture mechanics, can also be applied to analyze the lithiation/delithiation process and provide design guidelines for other materials. The finite element simulation approach should have potential application in analyzing the stress states, deformation and fracture mechanism of the electrode materials during lithiation and delithiation. By adopting the optimal design strategies proposed in this thesis, the electrochemical performance of the core-shell nanostructured electrode materials can be improved a lot for lithium ion batteries.

8.2. Outlook to the future work

The work in this thesis was focused on the structural integrity and optimal design of various core-shell nanostructured electrode materials. The future directions include the following aspects. First of all, further experimental and theoretical works should be conducted to study the growth mechanism of the lithium nanostructures on the surface of the Si-coated Cu nanowire electrodes during delithiation. It has been reported that the formation of the lithium nanostructures may be due to the high current density in the nanowire and the roughened surface of the Si shell. In order to confirm these hypotheses, the *in situ* lithiation and delithiation should be conducted on other nanowire electrodes with different electron conductivities, such as the bare Si nanowire electrodes and the Si-coated carbon nanowire electrodes, as well as the Si-coated Cu nanowire with smooth Si shell. In addition to the experiments, theoretical investigations should also be conducted. Another possible explanation for the formation of lithium nanostructures can be due to the uneven stress state in the Si shell during delithiation. In order to verify this speculation, experimental investigation, theoretical analysis and molecular dynamic simulation will be carried out to study the delithiation process of the Si-coated Cu nanowire electrode materials.

The *in situ* lithiation and delithiation cycling tests showed very good cycling performance of the Si-coated Cu nanowire electrode materials. In order to utilize the supreme cycling stability, two kinds of modified Cu current collector will be fabricated and assembled in coin-type half-cells for further electrochemical tests. The first kind of the current collector is the Cu nanoarray current collector, on which the Si electrode materials will be coated through magnetron sputtering technique. The nanostructures of the Cu nanoarray include nanofiber, nanocone and nanotube. The optimal design strategy will be exerted on the nanostructure by optimizing the thickness of the Si shell, the diameter and length of the Cu nanoarray and the inter-array distance between neighboring nanoarrays. Through such a design, the inter-nanoarray space (and inner space for nanotube array) will be made full use of and the maximum capacity and longest cycling life will be achieved. Another structure is the 3-D Si-coated Cu nanowire network anode materials. The 3-D Cu nanowire network will be synthesized as the current collector, due to its excellent structure stability and high electron conductivity. Binders and conductive additives are probably not required for this kind of electrode materials. Different amounts of the Si electrode material will be coated on the 3-D Cu nanowire network through magnetron sputtering technique. The network structure will be incorporated into the coin-type half-cell and the best performance will be obtained by comparing the amounts of the Si electrode materials through the electrochemical tests. These two kinds of modified Cu current collectors will exhibit high structural integrity and good cycling performance for lithium ion batteries.

The yolk-shell carbon-coated Si nanoparticle electrode materials show improved electrochemical performance by optimizing the geometrical structure. Inspired by the optimal design strategy, this approach will be utilized to design the yolk-shell carbon-coated Si or SnO_2 nanowire anode materials. The theoretical modeling in Chapter 6 will be revised to predict the fracture of the carbon shell in the yolk-shell nanowire electrodes. It is promising to obtain an optimal design guideline for the yolk-shell carbon-coated Si/SnO_2 nanowire electrode materials by optimizing the diameter and length of Si/SnO_2 nanowire, the interspace between Si/SnO_2 nanowire and carbon shell and the thickness of carbon shell. The electrochemical performance of the electrode materials will be tested by assembling them into the coin-type half-cell to achieve better electrochemical performance for lithium ion batteries.

Appendices

A. Solution of Eq. (4.4)

The diffusion equation of the lithium ion concentration in the SnO_2 nanowire is given by

$$\frac{\partial^2 \overline{C}}{\partial \bar{x}^2} - \frac{\partial \overline{C}}{\partial \bar{x}} = \frac{\partial \overline{C}}{\partial \bar{t}} \tag{A1}$$

Suppose $\bar{y} = \frac{\bar{x} - \bar{t}}{2\sqrt{\bar{t}}}$, then the partial derivatives of $\bar{y}$ over $\bar{x}$ and $\bar{t}$ are

$$\frac{\partial \bar{y}}{\partial \bar{x}} = \frac{1}{2\sqrt{\bar{t}}} \tag{A2}$$

$$\frac{\partial \bar{y}}{\partial \bar{t}} = -\frac{\bar{x}}{4\sqrt{\bar{t}^3}} - \frac{1}{4\sqrt{\bar{t}}} \tag{A3}$$

By definition, we can get

$$\frac{\partial \overline{C}}{\partial \bar{t}} = \frac{d\overline{C}}{d\bar{y}} \frac{\partial \bar{y}}{\partial \bar{t}} = -\left(\frac{\bar{x}}{4\sqrt{\bar{t}^3}} + \frac{1}{4\sqrt{\bar{t}}} \right) \frac{d\overline{C}}{d\bar{y}} \tag{A4}$$

$$\frac{\partial \overline{C}}{\partial \bar{x}} = \frac{d\overline{C}}{d\bar{y}} \frac{\partial \bar{y}}{\partial \bar{x}} = \frac{1}{2\sqrt{\bar{t}}} \frac{d\overline{C}}{d\bar{y}} \tag{A5}$$

$$\frac{\partial^2 \overline{C}}{\partial \bar{x}^2} = \frac{\partial}{\partial \bar{x}} \left(\frac{\partial \overline{C}}{\partial \bar{x}} \right) = \frac{\partial}{\partial \bar{x}} \left(\frac{1}{2\sqrt{\bar{t}}} \frac{d\overline{C}}{d\bar{y}} \right) \tag{A6}$$

Since $\bar{x} = 2\sqrt{\bar{t}}\,\bar{y} + \bar{t}$, Eq. (A6) can be expressed as

$$\frac{\partial^2 \overline{C}}{\partial \bar{x}^2} = \frac{1}{4\bar{t}} \frac{d^2 \overline{C}}{d\bar{y}^2} \tag{A7}$$

Substituting Eqs. (A4), (A5) and (A7) into Eq. (A1) leads to

$$\frac{1}{4\bar{t}} \frac{d^2 \overline{C}}{d\bar{y}^2} - \frac{1}{2\sqrt{\bar{t}}} \frac{d\overline{C}}{d\bar{y}} = -\left(\frac{\bar{x}}{4\sqrt{\bar{t}^3}} + \frac{1}{4\sqrt{\bar{t}}} \right) \frac{d\overline{C}}{d\bar{y}} \tag{A8}$$

Eq. (A8) can be simplified into

$$\frac{d^2 \overline{C}}{d\bar{y}^2} = \left(\sqrt{\bar{t}} - \frac{\bar{x}}{\sqrt{\bar{t}}} \right) \frac{d\overline{C}}{d\bar{y}} \tag{A9}$$

Recalling that $\bar{y} = \frac{\bar{x} - \bar{t}}{2\sqrt{\bar{t}}}$, Eq. (A9) can be transformed to

$$\frac{d^2 \overline{C}}{d\bar{y}^2} = -2\bar{y} \frac{d\overline{C}}{d\bar{y}} \tag{A10}$$

Let $\bar{z} = \frac{d\overline{C}}{d\bar{y}}$, then Eq. (A10) becomes

$$\frac{d\bar{z}}{d\bar{y}} = -2\bar{y}\bar{z} \tag{A11}$$

$$-2\int \bar{y} d\bar{y} = \int \frac{d\bar{z}}{\bar{z}} \tag{A12}$$

Taking the integration of Eq. (A12) yields

$$-\bar{y}^2 = \ln \bar{z} - \ln \mathrm{B} \tag{A13}$$

where B is the integration constant. Rearranging Eq. (A13) leads to

$$\bar{z} = \mathrm{B} \exp\left(-\bar{y}^2 \right) \tag{A14}$$

Since $\bar{z} = \frac{d\overline{C}}{d\bar{y}}$, Eq. (A14) can be transformed to

$$\int d\overline{C} = \mathrm{B}\int \exp\left(-\bar{y}^2\right)d\bar{y} \tag{A15}$$

where $\bar{y} = \frac{\bar{x}-\bar{t}}{2\sqrt{\bar{t}}}$. Here, the function $f = \exp\left(-\bar{y}^2\right)$ represents the "bell-shaped curve" and the solution of Eq. (A15) is based on the initial and boundary conditions.

The initial condition of the normalized concentration of lithium ion is given by

$$\overline{C}\left(\bar{t}=0\right) = \begin{cases} 1 & \left(\bar{x}=0\right) \\ 0 & \left(\bar{x}>0\right) \end{cases} \tag{A16}$$

That is,

$$\overline{C} = \begin{cases} 1 & \left(\bar{y}=0\right) \\ 0 & \left(\bar{y}=+\infty\right) \end{cases} \tag{A17}$$

Applying Eq. (A17) into Eq. (A15) gives

$$\int_1^0 d\overline{C} = \mathrm{B}\int_0^{+\infty} \exp\left(-\bar{y}^2\right)d\bar{y} \tag{A18}$$

The error function $\mathrm{Erf}\left(z\right) = \frac{2}{\sqrt{\pi}}\int_0^z \exp\left(-\bar{y}^2\right)d\bar{y}$ has the following property of

$$\int_0^{+\infty} \exp\left(-\bar{y}^2\right)d\bar{y} = \frac{\sqrt{\pi}}{2} \tag{A19}$$

Therefore, $\mathrm{B} = -\frac{2}{\sqrt{\pi}}$. Eq. (A15) is transformed to

$$\int d\overline{C} = -\frac{2}{\sqrt{\pi}}\int \exp\left(-\bar{y}^2\right)d\bar{y} \tag{A20}$$

After lithiation begins, the boundary condition is given by

$$\overline{C}\left(\bar{t} > 0\right) = \begin{cases} \overline{C} & \left(\bar{x} < +\infty\right) \\ 0 & \left(\bar{x} = +\infty\right) \end{cases} \tag{A21}$$

with $\bar{y} = \dfrac{\bar{x} - \bar{t}}{2\sqrt{\bar{t}}}$. Then we can get

$$\overline{C} = \begin{cases} \overline{C} & \left(\bar{y} < +\infty\right) \\ 0 & \left(\bar{y} = +\infty\right) \end{cases} \tag{A22}$$

Substituting Eq. (A22) into Eq. (A20) leads to

$$\int_{\overline{C}}^{0} d\overline{C} = -\frac{2}{\sqrt{\pi}}\int_{\bar{y}}^{+\infty} \exp\left(-\bar{y}^2\right)d\bar{y} \tag{A23}$$

The error function $\mathrm{Erf}\left(z\right)$ has the following property of

$$\mathrm{Erf}\ \left(\bar{y}\right) = 1 - \frac{2}{\sqrt{\pi}}\int_{\bar{y}}^{+\infty} \exp\left(-\bar{y}^2\right)d\bar{y} \tag{A24}$$

Substituting Eq. (A24) into Eq. (A23) yields

$$\overline{C} = 1 - \mathrm{Erf}\left(\bar{y}\right) \tag{A25}$$

It should be noted that $\overline{C}$ is no larger than 1. Therefore, $\overline{C} = 1$ when $\bar{y} < 0$ (or $\bar{x} < \bar{t}$). Eq. (A25) represents the lithium ion concentration when $\bar{y} \geq 0$ (or $\bar{x} \geq \bar{t}$). Therefore, the solution of the diffusion equation Eq. (4.4) is

$$\bar{C}\left(\bar{x},\bar{t}\right)=\begin{cases} 1 & \left(\bar{x}<\bar{t}\right) \\ 1-\mathrm{Erf}\,(\dfrac{\bar{x}-\bar{t}}{2\sqrt{\bar{t}}}) & \left(\bar{x}\geq\bar{t}\right) \end{cases} \tag{A26}$$

where Erf(z) is the error function defined by $\mathrm{Erf}\,(z)=\dfrac{2}{\sqrt{\pi}}\int_0^z e^{-y^2}\,dy$.

B. Convergence check

Since the reaction front is very sharp between the pristine Si and the lithiated Si during lithiation, the gradient of lithium ion concentration was neglected in our finite element model. The Si core of the carbon-coated Si nanoparticle was discretized into N shells as shown in Fig. A1a. The diameter of the Si core is 100 nm and the thickness of the carbon shell is 5 nm. The unit temperature increment was applied on the annuluses one after another from the outermost layer to the innermost core to simulate the progress of lithiation. In order to find how many annuluses can lead to a convergent result, the numbers of the annuluses were taken as 5, 10, 20, 40 and 80 in five cases. The maximum tensile stress in the carbon shell was calculated for the five cases, as shown in Fig. A1b. It can be found that the convergent result is obtained when the number of annuluses is higher than 40 for the carbon-coated Si nanoparticle electrode. Therefore, $N = 50$ was used in our simulation.

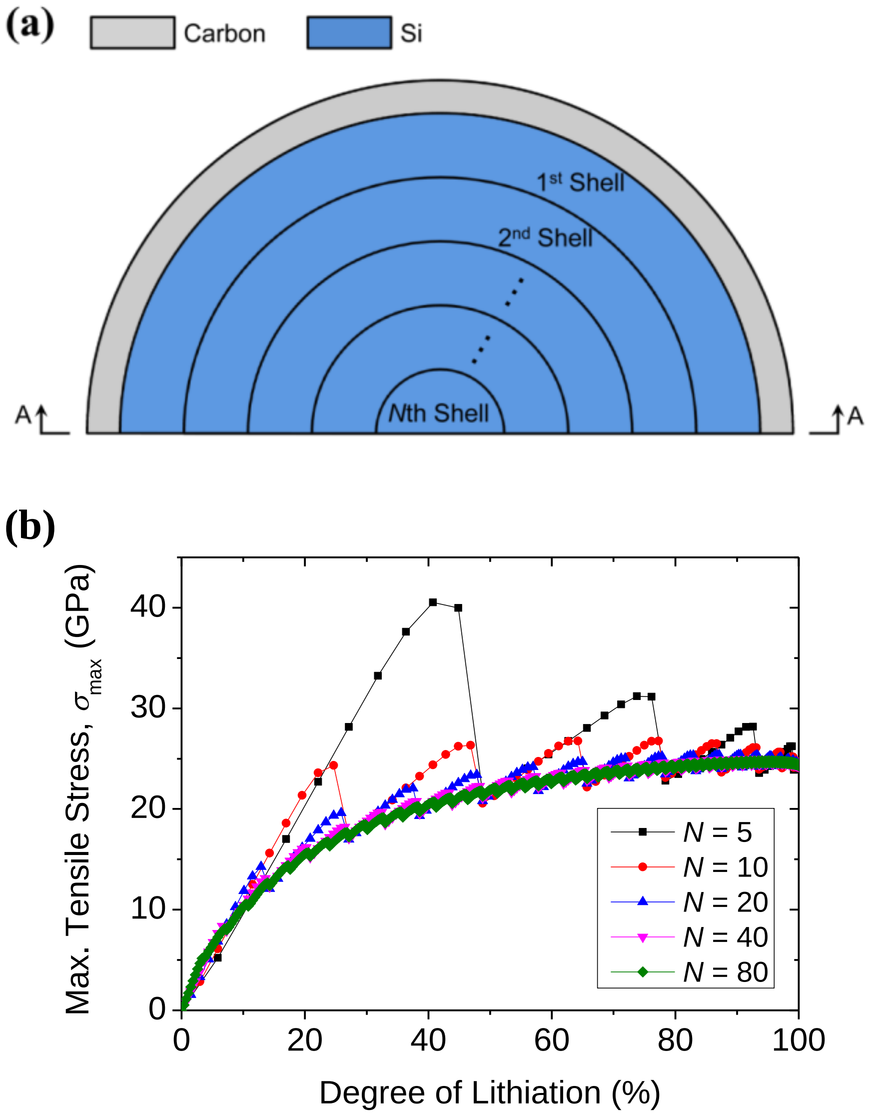

Figure A1. (a) Schematic of the finite element model for the carbon-coated Si nanoparticle electrode with the Si core being separated into *N* annuluses and (b) evolution of maximum tensile stress in the carbon shell as a function of degree of lithiation for different number of annuluses.

C. Path-dependent *J* integral

Fig. 5.9 shows the schematic of the contour paths for calculating the *J* integral near the crack tip. The crack is terminated at the carbon/Li$_x$Si interface. The energy release rates of the first six paths were calculated, as shown in Fig. A2. It can be seen that the energy release rate is path-dependent and decrease from the inside to the outside. The energy release rates of all the paths increase fast and soon exceed the fracture energy of the lithiated Si. It has been reported that due to the material's inhomogeneity, the near-tip *J* integral is higher than the far-field *J* integral if the crack approaches the interface from a higher strength material to a lower strength material. From Fig. A2, a convergent *J* integral can be obtained after the fifth path. Therefore, in our analysis, energy release rate of the fifth path, $J_{\Gamma 5}$, is taken as the effective crack tip energy release rate.

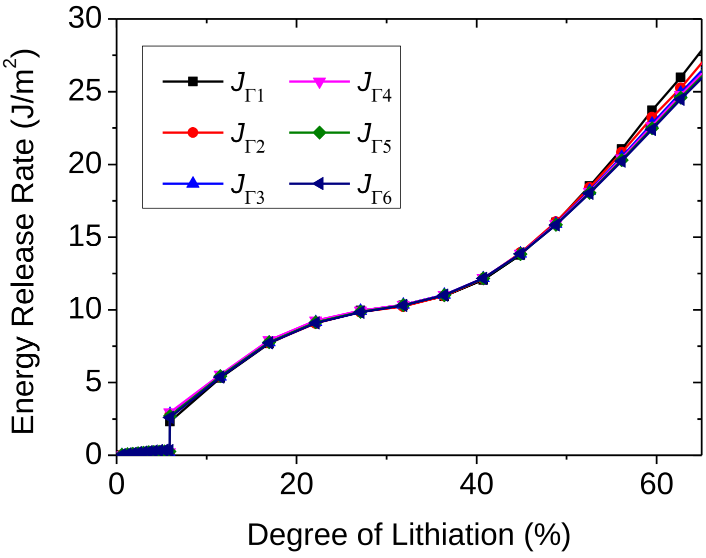

Figure A2. Evolution of the energy release rate of the first six contour paths around the tip of the crack.

D. Materials' inhomogeneity effect on energy release rate

A comparison study was made to further examine the effect of material's inhomogeneity on the energy release rate. The inserted images in Fig. A3 show finite element models for the carbon-coated Si nanoparticle with Si core diameter of 100 nm and carbon shell thickness of 5 nm and the Si nanoparticle with diameter of 110 nm. The crack length in the carbon shell of the carbon-coated Si nanoparticle is equal to that in the Si nanoparicle, which is 5 nm. The near tip J integrals, J_{tip}, were calculated in both models and summarized in Fig. A3. It can be found that the energy release rate near the crack tip of the carbon-coated Si nanoparticle increases much faster than that of the bare Si nanoparticle and soon exceeds the fracture energy of lithiated Si. This difference in energy release rate is due to the inhomogeneity effect and J integral increases when the crack tends to propagate from a stiff/hard material to a compliant/soft material.

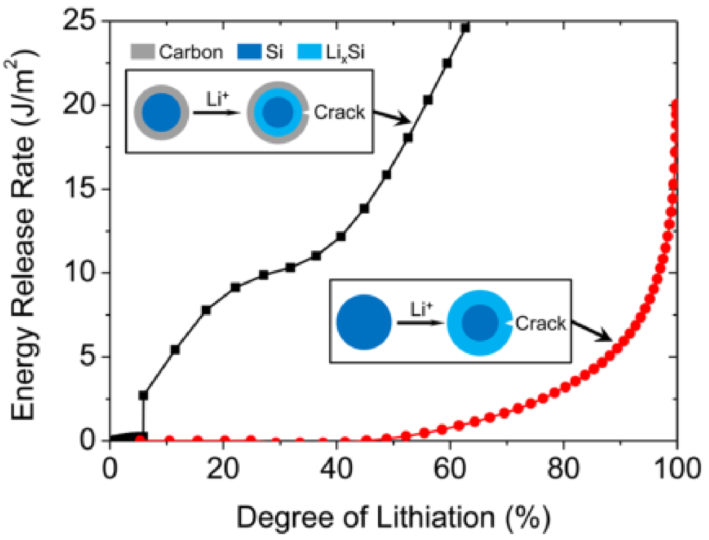

Figure A3. Evolution of the energy release rates around the tip of the cracks in a carbon-coated Si nanoparticle and a bare Si nanoparticle.

References

[1] I. A. Courtney, J. R. Dahn, Electrochemical and *in situ* X-ray diffraction studies of the reaction of lithium with tin oxide composites, *Journal of The Electrochemical Society* 144 (1997) 2045-2052.

[2] J. S. Chen, L. A. Archer, X. W. Lou, SnO_2 hollow structures and TiO_2 nanosheets for lithium-ion batteries, *Journal of Materials Chemistry* 21 (2011) 9912-9924.

[3] M. Mohamedi, S.-J. Lee, D. Takahashi, M. Nishizawa, T. Itoh, I. Uchida, Amorphous tin oxide films: preparation and characterization as an anode active material for lithium ion batteries, *Electrochimica Acta* 46 (2001) 1161-1168.

[4] Y. Idota, T. Kubota, A. Matsufuji, Y. Maekawa, T. Miyasaka, Tin-based amorphous oxide: a high-capacity lithium-ion-storage material, *Science* 276 (1997) 1395-1397.

[5] I. A. Courtney, J. R. Dahn, Key factors controlling the reversibility of the reaction of lithium with SnO_2 and Sn_2BPO_6 glass, *Journal of the Electrochemical Society* 144 (1997) 2943-2948.

[6] D. Deng, M. G. Kim, J. Y. Lee, J. Cho, Green energy storage materials: nanostructured TiO_2 and Sn-based anodes for lithium-ion batteries, *Energy & Environmental Science* 2 (2009) 818-837.

[7] J. S. Chen, X. W. Lou, SnO_2-based nanomaterials: synthesis and application in lithium-ion batteries, *Small* 9 (2013) 1877-1893.

[8] H. Wang, A. L. Rogach, Hierarchical SnO_2 nanostructures: recent advances in design, synthesis, and applications, *Chemistry of Materials* 26 (2014) 123-133.

[9] L. Liu, F. Xie, J. Lyu, T. Zhao, T. Li, B. G. Choi, Tin-based anode materials with well-designed architectures for next-generation lithium-ion batteries, *Journal of Power Sources* 321 (2016) 11-35.

[10] J. Zhu, Z. Lu, S. T. Aruna, D. Aurbach, A. Gedanken, Sonochemical synthesis of SnO_2 nanoparticles and their preliminary study as Li insertion electrodes, *Chemistry of Materials* 12 (2000) 2557-2566.

[11] H.-J. Ahn, H.-C. Choi, K.-W. Park, S.-B. Kim, Y.-E. Sung, Investigation of the structural and electrochemical properties of size-controlled SnO_2 nanoparticles, *The Journal of Physical Chemistry B* 108 (2004) 9815-9820.

[12] C. Kim, M. Noh, M. Choi, J. Cho, B. Park, Critical size of a nano SnO_2 electrode for Li-secondary battery, *Chemistry of Materials* 17 (2005) 3297-3301.

[13] S. Han, B. Jang, T. Kim, S. M. Oh, T. Hyeon, Simple synthesis of hollow tin dioxide microspheres and their application to lithium-ion battery anodes, *Advanced Functional Materials* 15 (2005) 1845-1850.

[14] R. Demir-Cakan, Y.-S. Hu, M. Antonietti, J. Maier, M.-M. Titirici, Facile one-pot synthesis of mesoporous SnO_2 microspheres via nanoparticles assembly and lithium storage properties, *Chemistry of Materials* 20 (2008) 1227-1229.

[15] Z. Ying, Q. Wan, H. Cao, Z. T. Song, S. L. Feng, Characterization of SnO_2 nanowires as an anode material for Li-ion batteries, *Applied Physics Letters* 87 (2005) 113108.

[16] M.-S. Park, G.-X. Wang, Y.-M. Kang, D. Wexler, S.-X. Dou, H.-K. Liu, Preparation and electrochemical properties of SnO_2 nanowires for application in lithium-ion batteries, *Angewandte Chemie International Edition* 119 (2007) 764-767.

[17] Y.-D. Ko, J.-G. Kang, J.-G. Park, S. Lee, D.-W. Kim, Self-supported SnO_2 nanowire electrodes for high-power lithium-ion batteries, *Nanotechnology* 20 (2009) 455701.

[18] Y. Wang, J. Y. Lee, H. C. Zeng, Polycrystalline SnO_2 nanotubes prepared via infiltration casting of nanocrystallites and their electrochemical application, *Chemistry of Materials* 17 (2005) 3899-3903.

[19] J. Ye, H. Zhang, R. Yang, X. Li, L. Qi, Morphology-controlled synthesis of SnO_2 Nanotubes by using 1D silica mesostructures as sacrificial templates and their applications in lithium-ion batteries, *Small* 6 (2010) 296-306.

[20] J. Wang, N. Du, H. Zhang, J. Yu, D. Yang, Large-scale synthesis of SnO_2 nanotube arrays as high-performance anode materials of Li-ion batteries, *The Journal of Physical Chemistry C* 115 (2011) 11302-11305.

[21] C. Wang, Y. Zhou, M. Ge, X. Xu, Z. Zhang, J. Z. Jiang, Large-scale synthesis of SnO_2 nanosheets with high lithium storage capacity, *Journal of the American Chemical Society* 132 (2010) 46-47.

[22] C. Wang, G. Du, K. Ståhl, H. Huang, Y. Zhong, J. Z. Jiang, Ultrathin SnO_2 nanosheets: oriented attachment mechanism, nonstoichiometric defects, and enhanced lithium-ion battery performances, *The Journal of Physical Chemistry C* 116 (2012) 4000-4011.

[23] X. W. Lou, Y. Wang, C. Yuan, J. Y. Lee, L. A. Archer, Template-free synthesis of SnO_2 hollow nanostructures with high lithium storage capacity, *Advanced Materials* 18 (2006) 2325-2329.

[24] Z. Wang, D. Luan, F. Y. C. Boey, X. W. Lou, Fast formation of SnO_2 nanoboxes with enhanced lithium storage capability, *Journal of the American Chemical Society* 133 (2011) 4738-4741.

[25] W.-S. Kim, Y. Hwa, J.-H. Jeun, H.-J. Sohn, S.-H. Hong, Synthesis of SnO_2 nano hollow spheres and their size effects in lithium ion battery anode application, *Journal of Power Sources* 225 (2013) 108-112.

[26] X. M. Yin, C. C. Li, M. Zhang, Q. Y. Hao, S. Liu, L. B. Chen, T. H. Wang, One-step synthesis of hierarchical SnO_2 hollow nanostructures via self-assembly for high power lithium ion batteries, *The Journal of Physical Chemistry C* 114 (2010) 8084-8088.

[27] H. B. Wu, J. S. Chen, X. W. Lou, H. H. Hng, Synthesis of SnO_2 hierarchical structures assembled from nanosheets and their lithium storage properties, *The Journal of Physical Chemistry C* 115 (2011) 24605-24610.

[28] X. W. Lou, D. Deng, J. Y. Lee, L. A. Archer, Preparation of SnO_2/carbon composite hollow spheres and their lithium storage properties, *Chemistry of Materials* 20 (2008) 6562-6566.

[29] D. Deng, J. Y. Lee, Hollow core-shell mesospheres of crystalline SnO_2 nanoparticle aggregates for high capacity Li^+ ion storage, *Chemistry of Materials* 20 (2008) 1841-1846.

[30] X. H. Liu, J. Y. Huang, In situ TEM electrochemistry of anode materials in lithium ion batteries, *Energy & Environmental Science* 4 (2011) 3844-3860.

[31] X. H. Liu, Y. Liu, A. Kushima, S. Zhang, T. Zhu, J. Li, J. Y. Huang, In situ TEM experiments of electrochemical lithiation and delithiation of individual nanostructures, *Advanced Energy Materials* 2 (2012) 722-741.

[32] X. Ma, W. Luo, M. Yan, L. He, L. Mai, *In situ* characterization of electrochemical processes in one dimensional nanomaterials for energy storages devices, *Nano Energy* 24 (2016) 165-188.

[33] D. S. Shih, I. M. Robertson, H. K. Birnbaum, Hydrogen embrittlement of α titanium: *In situ* tem studies, *Acta Metallurgica* 36 (1988) 111-124.

[34] J. Y. Huang, S. Chen, S. H. Jo, Z. Wang, D. X. Han, G. Chen, M. S. Dresselhaus, Z. F. Ren, Atomic-scale imaging of wall-by-wall breakdown and concurrent transport measurements in multiwall carbon nanotubes, *Physical Review Letters* 94 (2005) 236802.

[35] J. Y. Huang, S. Chen, Z. Q. Wang, K. Kempa, Y. M. Wang, S. H. Jo, G. Chen, M. S. Dresselhaus, Z. F. Ren, Superplastic carbon nanotubes, *Nature* 439 (2006) 281-281.

[36] J. B. Hannon, S. Kodambaka, F. M. Ross, R. M. Tromp, The influence of the surface migration of gold on the growth of silicon nanowires, *Nature* 440 (2006) 69-71.

[37] S. Kodambaka, J. Tersoff, M. C. Reuter, F. M. Ross, Germanium nanowire growth below the eutectic temperature, *Science* 316 (2007) 729-732.

[38] J. A. Rodríguez-Manzo, M. Terrones, H. Terrones, H. W. Kroto, L. Sun, F. Banhart, In situ nucleation of carbon nanotubes by the injection of carbon atoms into metal particles, *Nature nanotechnology* 2 (2007) 307-311.

[39] C. Jin, K. Suenaga, S. Iijima, Plumbing carbon nanotubes, *Nature Nanotechnology* 3 (2008) 17-21.

[40] Z. W. Shan, R. K. Mishra, S. A. Syed Asif, O. L. Warren, A. M. Minor, Mechanical annealing and source-limited deformation in submicrometre-diameter Ni crystals, *Nature Materials* 7 (2008) 115-119.

[41] J. Y. Huang, L. Zhong, C. M. Wang, J. P. Sullivan, W. Xu, L. Q. Zhang, S. X. Mao, N. S. Hudak, X. H. Liu, A. Subramanian, H. Fan, L. Qi, A. Kushima, J. Li, In situ observation of the electrochemical lithiation of a single SnO_2 nanowire electrode, *Science* 330 (2010) 1515-1520.

[42] C.-M. Wang, W. Xu, J. Liu, J.-G. Zhang, L. V. Saraf, B. W. Arey, D. Choi, Z.-G. Yang, J. Xiao, S. Thevuthasan, D. R. Baer, In situ transmission electron microscopy observation of microstructure and phase evolution in a SnO_2 nanowire during lithium intercalation, *Nano Letters* 11 (2011) 1874-1880.

[43] L. Zhong, X. H. Liu, G. F. Wang, S. X. Mao, J. Y. Huang, Multiple-stripe lithiation mechanism of individual SnO_2 nanowires in a flooding geometry, *Physical Review Letters* 106 (2011) 248302.

[44] A. Nie, L.-Y. Gan, Y. Cheng, H. Asayesh-Ardakani, Q. Li, C. Dong, R. Tao, F. Mashayek, H.-T. Wang, U. Schwingenschlögl, R. F. Klie, R. S. Yassar, Atomic-scale observation of lithiation reaction front in nanoscale SnO_2 materials, *ACS Nano* 7 (2013) 6203-6211.

[45] M. J. Williamson, R. M. Tromp, P. M. Vereecken, R. Hull, F. M. Ross, Dynamic microscopy of nanoscale cluster growth at the solid-liquid interface, *Nature Materials* 2 (2003) 532-536.

[46] H. Zheng, R. K. Smith, Y.-w. Jun, C. Kisielowski, U. Dahmen, A. P. Alivisatos, Observation of single colloidal platinum nanocrystal growth trajectories, *Science* 324 (2009) 1309-1312.

[47] X. H. Liu, H. Zheng, L. Zhong, S. Huang, K. Karki, L. Q. Zhang, Y. Liu, A. Kushima, W. T. Liang, J. W. Wang, J.-H. Cho, E. Epstein, S. A. Dayeh, S. T. Picraux, T. Zhu, J. Li, J. P. Sullivan, J. Cumings, C. Wang, S. X. Mao, Z. Z. Ye, S. Zhang, J. Y. Huang, Anisotropic swelling and fracture of silicon nanowires during lithiation, *Nano Letters* 11 (2011) 3312-3318.

[48] R. A. Sharma, R. N. Seefurth, Thermodynamic properties of the lithium-silicon system, *Journal of The Electrochemical Society* 123 (1976) 1763-1768.

[49] B. A. Boukamp, G. C. Lesh, R. A. Huggins, All-solid lithium electrodes with mixed-conductor matrix, *Journal of The Electrochemical Society* 128 (1981) 725-729.

[50] J. H. Ryu, J. W. Kim, Y.-E. Sung, S. M. Oh, Failure modes of silicon powder negative electrode in lithium secondary batteries, *Electrochemical and Solid-State Letters* 7 (2004) A306-A309.

[51] S. Bourderau, T. Brousse, D. M. Schleich, Amorphous silicon as a possible anode material for Li-ion batteries, *Journal of Power Sources* 81–82 (1999) 233-236.

[52] J. P. Maranchi, A. F. Hepp, P. N. Kumta, High capacity, reversible silicon thin-film anodes for lithium-ion batteries, *Electrochemical and Solid-State Letters* 6 (2003) A198-A201.

[53] U. Kasavajjula, C. Wang, A. J. Appleby, Nano- and bulk-silicon-based insertion anodes for lithium-ion secondary cells, *Journal of Power Sources* 163 (2007) 1003-1039.

[54] M. T. McDowell, S. W. Lee, W. D. Nix, Y. Cui, 25th anniversary article: understanding the lithiation of silicon and other alloying anodes for lithium-ion batteries, *Advanced Materials* 25 (2013) 4966-4985.

[55] M. R. Zamfir, H. T. Nguyen, E. Moyen, Y. H. Lee, D. Pribat, Silicon nanowires for Li-based battery anodes: a review, *Journal of Materials Chemistry A* 1 (2013) 9566-9586.

[56] M. A. Rahman, G. Song, A. I. Bhatt, Y. C. Wong, C. Wen, Nanostructured silicon anodes for high-performance lithium-ion batteries, *Advanced Functional Materials* 26 (2016) 647-678.

[57] T. Kennedy, M. Brandon, K. M. Ryan, Advances in the application of silicon and germanium nanowires for high-performance lithium-ion batteries, *Advanced Materials* 28 (2016) 5696-5704.

[58] J. K. Lee, C. Oh, N. Kim, J.-Y. Hwang, Y.-K. Sun, Rational design of silicon-based composites for high-energy storage devices, *Journal of Materials Chemistry A* 4 (2016) 5366-5384.

[59] H. Li, X. Huang, L. Chen, Z. Wu, Y. Liang, A high capacity nano-Si composite anode material for lithium rechargeable batteries, *Electrochemical and Solid-State Letters* 2 (1999) 547-549.

[60] D. Mazouzi, B. Lestriez, L. Roué, D. Guyomard, Silicon composite electrode with high capacity and long cycle life, *Electrochemical and Solid-State Letters* 12 (2009) A215-A218.

[61] H. Kim, M. Seo, M.-H. Park, J. Cho, A critical size of silicon nano-anodes for lithium rechargeable batteries, *Angewandte Chemie International Edition* 49 (2010) 2146-2149.

[62] H. Ma, F. Cheng, J. Chen, J. Zhao, C. Li, Z. Tao, J. Liang, Nest-like silicon nanospheres for high-capacity lithium storage, *Advanced Materials* 19 (2007) 4067-4070.

[63] Y. Kwon, G.-S. Park, J. Cho, Synthesis and electrochemical properties of lithium-electroactive surface-stabilized silicon quantum dots, *Electrochimica Acta* 52 (2007) 4663-4668.

[64] N. Liu, K. Huo, M. T. McDowell, J. Zhao, Y. Cui, Rice husks as a sustainable source of nanostructured silicon for high performance Li-ion battery anodes, *Scientific Reports* 3 (2013) 1919.

[65] C. K. Chan, H. Peng, G. Liu, K. McIlwrath, X. F. Zhang, R. A. Huggins, Y. Cui, High-performance lithium battery anodes using silicon nanowires, *Nature nanotechnology* 3 (2008) 31-35.

[66] K. Peng, J. Jie, W. Zhang, S.-T. Lee, Silicon nanowires for rechargeable lithium-ion battery anodes, *Applied Physics Letters* 93 (2008) 033105.

[67] N. Liu, L. Hu, M. T. McDowell, A. Jackson, Y. Cui, Prelithiated silicon nanowires as an anode for lithium ion batteries, *ACS Nano* 5 (2011) 6487-6493.

[68] M.-H. Park, M. G. Kim, J. Joo, K. Kim, J. Kim, S. Ahn, Y. Cui, J. Cho, Silicon nanotube battery anodes, *Nano Letters* 9 (2009) 3844-3847.

[69] T. Song, J. Xia, J.-H. Lee, D. H. Lee, M.-S. Kwon, J.-M. Choi, J. Wu, S. K. Doo, H. Chang, W. I. Park, D. S. Zang, H. Kim, Y. Huang, K.-C. Hwang, J. A. Rogers, U. Paik, Arrays of sealed silicon nanotubes as anodes for lithium ion batteries, *Nano Letters* 10 (2010) 1710-1716.

[70] J.-K. Yoo, J. Kim, Y. S. Jung, K. Kang, Scalable fabrication of silicon nanotubes and their application to energy storage, *Advanced Materials* 24 (2012) 5452-5456.

[71] J. Graetz, C. C. Ahn, R. Yazami, B. Fultz, Highly reversible lithium storage in nanostructured silicon, *Electrochemical and Solid-State Letters* 6 (2003) A194-A197.

[72] S. Ohara, J. Suzuki, K. Sekine, T. Takamura, Li insertion/extraction reaction at a Si film evaporated on a Ni foil, *Journal of Power Sources* 119–121 (2003) 591-596.

[73] T. Takamura, S. Ohara, M. Uehara, J. Suzuki, K. Sekine, A vacuum deposited Si film having a Li extraction capacity over 2000 mAh/g with a long cycle life, *Journal of Power Sources* 129 (2004) 96-100.

[74] C. Yu, X. Li, T. Ma, J. Rong, R. Zhang, J. Shaffer, Y. An, Q. Liu, B. Wei, H. Jiang, Silicon thin films as anodes for high-performance lithium-ion batteries with effective stress relaxation, *Advanced Energy Materials* 2 (2012) 68-73.

[75] R. A. Huggins, W. D. Nix, Decrepitation model for capacity loss during cycling of alloys in rechargeable electrochemical systems, *Ionics* 6 (2000) 57-63.

[76] Y. Yu, L. Gu, C. Zhu, S. Tsukimoto, P. A. van Aken, J. Maier, Reversible storage of lithium in silver-coated three-dimensional macroporous silicon, *Advanced Materials* 22 (2010) 2247-2250.

[77] J. Cho, Porous Si anode materials for lithium rechargeable batteries, *Journal of Materials Chemistry* 20 (2010) 4009-4014.

[78] H. Jia, P. Gao, J. Yang, J. Wang, Y. Nuli, Z. Yang, Novel three-dimensional mesoporous silicon for high power lithium-ion battery anode material, *Advanced Energy Materials* 1 (2011) 1036-1039.

[79] M. Thakur, S. L. Sinsabaugh, M. J. Isaacson, M. S. Wong, S. L. Biswal, Inexpensive method for producing macroporous silicon particulates (MPSPs) with pyrolyzed polyacrylonitrile for lithium ion batteries, *Scientific Reports* 2 (2012) 795.

[80] Y. Zhao, X. Liu, H. Li, T. Zhai, H. Zhou, Hierarchical micro/nano porous silicon Li-ion battery anodes, *Chemical Communications* 48 (2012) 5079-5081.

[81] M. Thakur, R. B. Pernites, N. Nitta, M. Isaacson, S. L. Sinsabaugh, M. S. Wong, S. L. Biswal, Freestanding macroporous silicon and pyrolyzed polyacrylonitrile as a composite anode for lithium ion batteries, *Chemistry of Materials* 24 (2012) 2998-3003.

[82] M. Thakur, M. Isaacson, S. L. Sinsabaugh, M. S. Wong, S. L. Biswal, Gold-coated porous silicon films as anodes for lithium ion batteries, *Journal of Power Sources* 205 (2012) 426-432.

[83] J. Zhu, C. Gladden, N. Liu, Y. Cui, X. Zhang, Nanoporous silicon networks as anodes for lithium ion batteries, *Physical Chemistry Chemical Physics* 15 (2013) 440-443.

[84] M. Ge, J. Rong, X. Fang, A. Zhang, Y. Lu, C. Zhou, Scalable preparation of porous silicon nanoparticles and their application for lithium-ion battery anodes, *Nano Research* 6 (2013) 174-181.

[85] X. Li, M. Gu, S. Hu, R. Kennard, P. Yan, X. Chen, C. Wang, M. J. Sailor, J.-G. Zhang, J. Liu, Mesoporous silicon sponge as an anti-pulverization structure for high-performance lithium-ion battery anodes, *Nature Communications* 5 (2014).

[86] T. Wada, T. Ichitsubo, K. Yubuta, H. Segawa, H. Yoshida, H. Kato, Bulk-nanoporous-silicon negative electrode with extremely high cyclability for lithium-ion batteries prepared using a top-down process, *Nano Letters* 14 (2014) 4505-4510.

[87] M. Ge, Y. Lu, P. Ercius, J. Rong, X. Fang, M. Mecklenburg, C. Zhou, Large-scale fabrication, 3D tomography, and lithium-ion battery application of porous silicon, *Nano Letters* 14 (2014) 261-268.

[88] W. Wang, Z. Favors, R. Ionescu, R. Ye, H. H. Bay, M. Ozkan, C. S. Ozkan, Monodisperse porous silicon spheres as anode materials for lithium ion batteries, *Scientific Reports* 5 (2015).

[89] J. L. Goldman, B. R. Long, A. A. Gewirth, R. G. Nuzzo, Strain anisotropies and self-limiting capacities in single-crystalline 3D silicon

microstructures: models for high energy density lithium-ion battery anodes, *Advanced Functional Materials* 21 (2011) 2412-2422.

[90] S. W. Lee, M. T. McDowell, J. W. Choi, Y. Cui, Anomalous shape changes of silicon nanopillars by electrochemical lithiation, *Nano Letters* 11 (2011) 3034-3039.

[91] S. W. Lee, M. T. McDowell, L. A. Berla, W. D. Nix, Y. Cui, Fracture of crystalline silicon nanopillars during electrochemical lithium insertion, *Proceedings of the National Academy of Sciences* 109 (2012) 4080-4085.

[92] C.-M. Wang, X. Li, Z. Wang, W. Xu, J. Liu, F. Gao, L. Kovarik, J.-G. Zhang, J. Howe, D. J. Burton, Z. Liu, X. Xiao, S. Thevuthasan, D. R. Baer, In situ TEM investigation of congruent phase transition and structural evolution of nanostructured silicon/carbon anode for lithium ion batteries, *Nano Letters* 12 (2012) 1624-1632.

[93] M. Gu, Z. Wang, J. G. Connell, D. E. Perea, L. J. Lauhon, F. Gao, C. Wang, Electronic origin for the phase transition from amorphous Li_xSi to Crystalline $Li_{15}Si_4$, *ACS Nano* 7 (2013) 6303-6309.

[94] X. H. Liu, L. Q. Zhang, L. Zhong, Y. Liu, H. Zheng, J. W. Wang, J.-H. Cho, S. A. Dayeh, S. T. Picraux, J. P. Sullivan, S. X. Mao, Z. Z. Ye, J. Y. Huang, Ultrafast electrochemical lithiation of individual Si nanowire anodes, *Nano Letters* 11 (2011) 2251-2258.

[95] T. D. Hatchard, J. R. Dahn, In situ XRD and electrochemical study of the reaction of lithium with amorphous silicon, *Journal of The Electrochemical Society* 151 (2004) A838-A842.

[96] B. Key, R. Bhattacharyya, M. Morcrette, V. Seznéc, J.-M. Tarascon, C. P. Grey, Real-time NMR investigations of structural changes in silicon electrodes for lithium-ion batteries, *Journal of the American Chemical Society* 131 (2009) 9239-9249.

[97] B. Key, M. Morcrette, J.-M. Tarascon, C. P. Grey, Pair distribution function analysis and solid state NMR studies of silicon electrodes for lithium ion batteries: understanding the (de)lithiation mechanisms, *Journal of the American Chemical Society* 133 (2011) 503-512.

[98] M. N. Obrovac, L. Christensen, Structural changes in silicon anodes during lithium insertion/extraction, *Electrochemical and Solid-State Letters* 7 (2004) A93-A96.

[99] J. W. Wang, X. H. Liu, K. Zhao, A. Palmer, E. Patten, D. Burton, S. X. Mao, Z. Suo, J. Y. Huang, Sandwich-lithiation and longitudinal crack in amorphous silicon coated on carbon nanofibers, *ACS Nano* 6 (2012) 9158-9167.

[100] K. Karki, E. Epstein, J.-H. Cho, Z. Jia, T. Li, S. T. Picraux, C. Wang, J. Cumings, Lithium-assisted electrochemical welding in silicon nanowire battery electrodes, *Nano Letters* 12 (2012) 1392-1397.

[101] X. H. Liu, L. Zhong, S. Huang, S. X. Mao, T. Zhu, J. Y. Huang, Size-dependent fracture of silicon nanoparticles during lithiation, *ACS Nano* 6 (2012) 1522-1531.

[102] M. T. McDowell, S. W. Lee, J. T. Harris, B. A. Korgel, C. Wang, W. D. Nix, Y. Cui, In situ TEM of two-phase lithiation of amorphous silicon nanospheres, *Nano Letters* 13 (2013) 758-764.

[103] M. T. McDowell, I. Ryu, S. W. Lee, C. Wang, W. D. Nix, Y. Cui, Studying the kinetics of crystalline silicon nanoparticle lithiation with in situ transmission electron microscopy, *Advanced Materials* 24 (2012) 6034-6041.

[104] X. H. Liu, J. W. Wang, S. Huang, F. Fan, X. Huang, Y. Liu, S. Krylyuk, J. Yoo, S. A. Dayeh, A. V. Davydov, S. X. Mao, S. T. Picraux, S. Zhang, J. Li, T. Zhu, J. Y. Huang, In situ atomic-scale imaging of electrochemical lithiation in silicon, *Nature Nanotechnology* 7 (2012) 749-756.

[105] J. W. Wang, Y. He, F. Fan, X. H. Liu, S. Xia, Y. Liu, C. T. Harris, H. Li, J. Y. Huang, S. X. Mao, T. Zhu, Two-phase electrochemical lithiation in amorphous silicon, *Nano Letters* 13 (2013) 709-715.

[106] M. Yoshio, H. Wang, K. Fukuda, T. Umeno, N. Dimov, Z. Ogumi, Carbon-coated Si as a lithium-ion battery anode material, *Journal of The Electrochemical Society* 149 (2002) A1598-A1603.

[107] S. H. Ng, J. Wang, D. Wexler, K. Konstantinov, Z. P. Guo, H. K. Liu, Highly reversible lithium storage in spheroidal carbon-coated silicon nanocomposites as anodes for lithium-ion batteries, *Angewandte Chemie International Edition* 45 (2006) 6896-6899.

[108] S. H. Ng, J. Wang, D. Wexler, S. Y. Chew, H. K. Liu, Amorphous carbon-coated silicon nanocomposites: a low-temperature synthesis via spray pyrolysis and their application as high-capacity anodes for lithium-ion batteries, *The Journal of Physical Chemistry C* 111 (2007) 11131-11138.

[109] S. H. Ng, J. Wang, K. Konstantinov, D. Wexler, S. Y. Chew, Z. P. Guo, H. K. Liu, Spray-pyrolyzed silicon/disordered carbon nanocomposites for lithium-ion battery anodes, *Journal of Power Sources* 174 (2007) 823-827.

[110] M. K. Datta, P. N. Kumta, Silicon, graphite and resin based hard carbon nanocomposite anodes for lithium ion batteries, *Journal of Power Sources* 165 (2007) 368-378.

[111] H. Chen, Z. Dong, Y. Fu, Y. Yang, Silicon nanowires with and without carbon coating as anode materials for lithium-ion batteries, *Journal of Solid State Electrochemistry* 14 (2010) 1829-1834.

[112] J. Song, S. Chen, M. Zhou, T. Xu, D. Lv, M. L. Gordin, T. Long, M. Melnyk, D. Wang, Micro-sized silicon-carbon composites composed of carbon-coated sub-10 nm Si primary particles as high-performance anode materials for lithium-ion batteries, *Journal of Materials Chemistry A* 2 (2014) 1257-1262.

[113] L. Xue, G. Xu, Y. Li, S. Li, K. Fu, Q. Shi, X. Zhang, Carbon-coated Si nanoparticles dispersed in carbon nanotube networks as anode material for lithium-ion batteries, *ACS Applied Materials & Interfaces* 5 (2013) 21-25.

[114] L. Ji, X. Zhang, Electrospun carbon nanofibers containing silicon particles as an energy-storage medium, *Carbon* 47 (2009) 3219-3226.

[115] H. Chen, Y. Xiao, L. Wang, Y. Yang, Silicon nanowires coated with copper layer as anode materials for lithium-ion batteries, *Journal of Power Sources* 196 (2011) 6657-6662.

[116] S. Murugesan, J. T. Harris, B. A. Korgel, K. J. Stevenson, Copper-coated amorphous silicon particles as an anode material for lithium-ion batteries, *Chemistry of Materials* 24 (2012) 1306-1315.

[117] E. L. Memarzadeh, W. P. Kalisvaart, A. Kohandehghan, B. Zahiri, C. M. B. Holt, D. Mitlin, Silicon nanowire core aluminum shell coaxial nanocomposites for lithium ion battery anodes grown with and without a TiN interlayer, *Journal of Materials Chemistry* 22 (2012) 6655-6668.

[118] A. Kohandehghan, P. Kalisvaart, M. Kupsta, B. Zahiri, B. S. Amirkhiz, Z. Li, E. L. Memarzadeh, L. A. Bendersky, D. Mitlin, Magnesium and magnesium-silicide coated silicon nanowire composite anodes for lithium-ion batteries, *Journal of Materials Chemistry A* 1 (2013) 1600-1612.

[119] H. Wu, G. Chan, J. W. Choi, I. Ryu, Y. Yao, M. T. McDowell, S. W. Lee, A. Jackson, Y. Yang, L. Hu, Y. Cui, Stable cycling of double-walled silicon nanotube battery anodes through solid-electrolyte interphase control, *Nature Nanotechnology* 7 (2012) 310-315.

[120] M. Gu, Y. Li, X. Li, S. Hu, X. Zhang, W. Xu, S. Thevuthasan, D. R. Baer, J.-G. Zhang, J. Liu, C. Wang, *In situ* TEM study of lithiation behavior of silicon nanoparticles attached to and embedded in a carbon matrix, *ACS Nano* 6 (2012) 8439-8447.

[121] K. Zhao, M. Pharr, L. Hartle, J. J. Vlassak, Z. Suo, Fracture and debonding in lithium-ion batteries with electrodes of hollow core–shell nanostructures, *Journal of Power Sources* 218 (2012) 6-14.

[122] M. E. Stournara, Y. Qi, V. B. Shenoy, From ab initio calculations to multiscale design of Si/C core–shell particles for Li-ion anodes, *Nano Letters* 14 (2014) 2140-2149.

[123] N. Liu, H. Wu, M. T. McDowell, Y. Yao, C. Wang, Y. Cui, A yolk-shell design for stabilized and scalable Li-ion battery alloy anodes, *Nano Letters* 12 (2012) 3315-3321.

[124] J. Yang, Y.-X. Wang, S.-L. Chou, R. Zhang, Y. Xu, J. Fan, W.-X. Zhang, H. K. Liu, D. Zhao, S. X. Dou, Yolk-shell silicon-mesoporous carbon anode with compact solid electrolyte interphase film for superior lithium-ion batteries, *Nano Energy* 18 (2015) 133-142.

[125] X.-Y. Zhou, J.-J. Tang, J. Yang, J. Xie, L.-L. Ma, Silicon@carbon hollow core-shell heterostructures novel anode materials for lithium ion batteries, *Electrochimica Acta* 87 (2013) 663-668.

[126] L. Su, J. Xie, Y. Xu, L. Wang, Y. Wang, M. Ren, Preparation and lithium storage performance of yolk-shell Si@void@C nanocomposites, *Physical Chemistry Chemical Physics* 17 (2015) 17562-17565.

[127] X. Li, P. Meduri, X. Chen, W. Qi, M. H. Engelhard, W. Xu, F. Ding, J. Xiao, W. Wang, C. Wang, J.-G. Zhang, J. Liu, Hollow core-shell structured porous Si-C nanocomposites for Li-ion battery anodes, *Journal of Materials Chemistry* 22 (2012) 11014-11017.

[128] S. Chen, M. L. Gordin, R. Yi, G. Howlett, H. Sohn, D. Wang, Silicon core-hollow carbon shell nanocomposites with tunable buffer voids for high capacity anodes of lithium-ion batteries, *Physical Chemistry Chemical Physics* 14 (2012) 12741-12745.

[129] H. Tao, L.-Z. Fan, W.-L. Song, M. Wu, X. He, X. Qu, Hollow core-shell structured Si/C nanocomposites as high-performance anode materials for lithium-ion batteries, *Nanoscale* 6 (2014) 3138-3142.

[130] Y. Ru, D. G. Evans, H. Zhu, W. Yang, Facile fabrication of yolk-shell structured porous Si-C microspheres as effective anode materials for Li-ion batteries, *RSC Advances* 4 (2014) 71-75.

[131] K. Wan, S. F. Y. Li, Z. Gao, K. S. Siow, Tin-based oxide anode for lithium-ion batteries with low irreversible capacity, *Journal of Power Sources* 75 (1998) 9-12.

[132] Y. Yu, C.-H. Chen, Y. Shi, A tin-based amorphous oxide composite with a porous, spherical, multideck-cage morphology as a highly reversible anode material for lithium-ion batteries, *Advanced Materials* 19 (2007) 993-997.

[133] W. Xu, N. L. Canfield, D. Wang, J. Xiao, Z. Nie, J.-G. Zhang, A three-dimensional macroporous Cu/SnO_2 composite anode sheet prepared via a novel method, *Journal of Power Sources* 195 (2010) 7403-7408.

[134] D. Kim, D. Lee, J. Kim, J. Moon, Electrospun Ni-added SnO_2–carbon nanofiber composite anode for high-performance lithium-ion batteries, *ACS Applied Materials & Interfaces* 4 (2012) 5408-5415.

[135] J. Lin, Z. Peng, C. Xiang, G. Ruan, Z. Yan, D. Natelson, J. M. Tour, Graphene nanoribbon and nanostructured SnO_2 composite anodes for lithium ion batteries, *ACS Nano* 7 (2013) 6001-6006.

[136] Z. P. Guo, J. Z. Wang, H. K. Liu, S. X. Dou, Study of silicon/polypyrrole composite as anode materials for Li-ion batteries, *Journal of Power Sources* 146 (2005) 448-451.

[137] J. K. Lee, K. B. Smith, C. M. Hayner, H. H. Kung, Silicon nanoparticles-graphene paper composites for Li ion battery anodes, *Chemical Communications* 46 (2010) 2025-2027.

[138] W. Wang, P. N. Kumta, Nanostructured hybrid silicon/carbon nanotube heterostructures: reversible high-capacity lithium-ion anodes, *ACS Nano* 4 (2010) 2233-2241.

[139] B. Fuchsbichler, C. Stangl, H. Kren, F. Uhlig, S. Koller, High capacity graphite–silicon composite anode material for lithium-ion batteries, *Journal of Power Sources* 196 (2011) 2889-2892.

[140] M. Dasog, J. Kehrle, B. Rieger, J. G. C. Veinot, Silicon nanocrystals and silicon-polymer hybrids: synthesis, surface engineering, and applications, *Angewandte Chemie International Edition* 55 (2016) 2322-2339.

[141] N. S. Hochgatterer, M. R. Schweiger, S. Koller, P. R. Raimann, T. Wöhrle, C. Wurm, M. Winter, Silicon/graphite composite electrodes for high-capacity anodes: influence of binder chemistry on cycling stability, *Electrochemical and Solid-State Letters* 11 (2008) A76-A80.

[142] L. Chen, X. Xie, J. Xie, K. Wang, J. Yang, Binder effect on cycling performance of silicon/carbon composite anodes for lithium ion batteries, *Journal of Applied Electrochemistry* 36 (2006) 1099-1104.

[143] B. Koo, H. Kim, Y. Cho, K. T. Lee, N.-S. Choi, J. Cho, A highly cross-linked polymeric binder for high-performance silicon negative electrodes in lithium ion batteries, *Angewandte Chemie International Edition* 51 (2012) 8762-8767.

[144] M.-H. Ryou, J. Kim, I. Lee, S. Kim, Y. K. Jeong, S. Hong, J. H. Ryu, T.-S. Kim, J.-K. Park, H. Lee, J. W. Choi, Mussel-inspired adhesive binders for high-performance silicon nanoparticle anodes in lithium-ion batteries, *Advanced Materials* 25 (2013) 1571-1576.

[145] C. Erk, T. Brezesinski, H. Sommer, R. Schneider, J. Janek, Toward silicon anodes for next-generation lithium ion batteries: a comparative performance study of various polymer binders and silicon nanopowders, *ACS Applied Materials & Interfaces* 5 (2013) 7299-7307.

[146] J. Song, M. Zhou, R. Yi, T. Xu, M. L. Gordin, D. Tang, Z. Yu, M. Regula, D. Wang, Interpenetrated gel polymer binder for high-performance silicon anodes in lithium-ion batteries, *Advanced Functional Materials* 24 (2014) 5904-5910.

[147] B. P. N. Nguyen, N. A. Kumar, J. Gaubicher, F. Duclairoir, T. Brousse, O. Crosnier, L. Dubois, G. Bidan, D. Guyomard, B. Lestriez, Nanosilicon-based thick negative composite electrodes for lithium batteries with graphene as conductive additive, *Advanced Energy Materials* 3 (2013) 1351-1357.

[148] W.-R. Liu, Z.-Z. Guo, W.-S. Young, D.-T. Shieh, H.-C. Wu, M.-H. Yang, N.-L. Wu, Effect of electrode structure on performance of Si anode in Li-ion batteries: Si particle size and conductive additive, *Journal of Power Sources* 140 (2005) 139-144.

[149] Y.-L. Kim, Y.-K. Sun, S.-M. Lee, Enhanced electrochemical performance of silicon-based anode material by using current collector with modified surface morphology, *Electrochimica Acta* 53 (2008) 4500-4504.

[150] X.-Y. Fan, F.-S. Ke, G.-Z. Wei, L. Huang, S.-G. Sun, Sn–Co alloy anode using porous Cu as current collector for lithium ion battery, *Journal of Alloys and Compounds* 476 (2009) 70-73.

[151] W. Xu, N. L. Canfield, D. Wang, J. Xiao, Z. Nie, X. S. Li, W. D. Bennett, C. C. Bonham, J.-G. Zhang, An approach to make macroporous metal sheets as current collectors for lithium-ion batteries, *Journal of The Electrochemical Society* 157 (2010) A765-A769.

[152] K. Wang, S. Luo, Y. Wu, X. He, F. Zhao, J. Wang, K. Jiang, S. Fan, Super-aligned carbon nanotube films as current collectors for lightweight and flexible lithium ion batteries, *Advanced Functional Materials* 23 (2013) 846-853.

[153] J. Luo, J. Liu, Z. Zeng, C. F. Ng, L. Ma, H. Zhang, J. Lin, Z. Shen, H. J. Fan, Three-dimensional graphene foam supported Fe_3O_4 lithium battery anodes with long cycle life and high rate capability, *Nano Letters* 13 (2013) 6136-6143.

[154] Y. Liu, K. Huang, Y. Fan, Q. Zhang, F. Sun, T. Gao, L. Yang, J. Zhong, Three-dimensional network current collectors supported Si nanowires for lithium-ion battery applications, *Electrochimica Acta* 88 (2013) 766-771.

[155] F.-F. Cao, J.-W. Deng, S. Xin, H.-X. Ji, O. G. Schmidt, L.-J. Wan, Y.-G. Guo, Cu-Si nanocable arrays as high-rate anode materials for lithium-ion batteries, *Advanced Materials* 23 (2011) 4415-4420.

[156] J. Qu, H. Li, J. J. Henry Jr, S. K. Martha, N. J. Dudney, H. Xu, M. Chi, M. J. Lance, S. M. Mahurin, T. M. Besmann, S. Dai, Self-aligned Cu–Si core–shell nanowire array as a high-performance anode for Li-ion batteries, *Journal of Power Sources* 198 (2012) 312-317.

[157] G. Kim, S. Jeong, J.-H. Shin, J. Cho, H. Lee, 3D amorphous silicon on nanopillar copper electrodes as anodes for high-rate lithium-ion batteries, *ACS Nano* 8 (2014) 1907-1912.

[158] L. Sun, X. Wang, R. A. Susantyoko, Q. Zhang, Copper-silicon core-shell nanotube arrays for free-standing lithium ion battery anodes, *Journal of Materials Chemistry A* 2 (2014) 15294-15297.

[159] N. Wang, T. Hang, H. Ling, A. Hu, M. Li, High-performance Si-based 3D Cu nanostructured electrode assembly for rechargeable lithium batteries, *Journal of Materials Chemistry A* 3 (2015) 11912-11919.

[160] N. Wang, T. Hang, W. Zhang, M. Li, Highly conductive Cu nanoneedle-array supported silicon film for high-performance lithium ion battery anodes, *Journal of The Electrochemical Society* 163 (2016) A380-A384.

[161] B. Hertzberg, J. Benson, G. Yushin, Ex-situ depth-sensing indentation measurements of electrochemically produced Si–Li alloy films, *Electrochemistry Communications* 13 (2011) 818-821.

[162] A. Kushima, J. Y. Huang, J. Li, Quantitative fracture strength and plasticity measurements of lithiated silicon nanowires by *in situ* TEM tensile experiments, *ACS Nano* 6 (2012) 9425-9432.

[163] S. T. Boles, C. V. Thompson, O. Kraft, R. Mönig, In situ tensile and creep testing of lithiated silicon nanowires, *Applied Physics Letters* 103 (2013) 263906.

[164] H. Lee, W. Shin, J. W. Choi, J. Y. Park, Nanomechanical properties of lithiated Si nanowires probed with atomic force microscopy, *Journal of Physics D: Applied Physics* 45 (2012) 275301.

[165] V. A. Sethuraman, M. J. Chon, M. Shimshak, N. Van Winkle, P. R. Guduru, In situ measurement of biaxial modulus of Si anode for Li-ion batteries, *Electrochemistry Communications* 12 (2010) 1614-1617.

[166] V. B. Shenoy, P. Johari, Y. Qi, Elastic softening of amorphous and crystalline Li–Si phases with increasing Li concentration: A first-principles study, *Journal of Power Sources* 195 (2010) 6825-6830.

[167] P. Johari, Y. Qi, V. B. Shenoy, The mixing mechanism during lithiation of Si negative electrode in Li-ion batteries: An ab initio molecular dynamics study, *Nano Letters* 11 (2011) 5494-5500.

[168] M. E. Stournara, P. R. Guduru, V. B. Shenoy, Elastic behavior of crystalline Li–Sn phases with increasing Li concentration, *Journal of Power Sources* 208 (2012) 165-169.

[169] T. K. Bhandakkar, H. Gao, Cohesive modeling of crack nucleation under diffusion induced stresses in a thin strip: Implications on the critical size for flaw tolerant battery electrodes, *International Journal of Solids and Structures* 47 (2010) 1424-1434.

[170] H. Haftbaradaran, X. Xiao, M. W. Verbrugge, H. Gao, Method to deduce the critical size for interfacial delamination of patterned electrode structures and application to lithiation of thin-film silicon islands, *Journal of Power Sources* 206 (2012) 357-366.

[171] J. Li, A. K. Dozier, Y. Li, F. Yang, Y.-T. Cheng, Crack pattern formation in thin film lithium-ion battery electrodes, *Journal of The Electrochemical Society* 158 (2011) A689-A694.

[172] M. J. Chon, V. A. Sethuraman, A. McCormick, V. Srinivasan, P. R. Guduru, Real-time measurement of stress and damage evolution during initial lithiation of crystalline silicon, *Physical Review Letters* 107 (2011) 045503.

[173] H. B. Chew, B. Hou, X. Wang, S. Xia, Cracking mechanisms in lithiated silicon thin film electrodes, *International Journal of Solids and Structures* 51 (2014) 4176-4187.

[174] M. Pharr, Z. Suo, J. J. Vlassak, Measurements of the fracture energy of lithiated silicon electrodes of Li-ion batteries, *Nano Letters* 13 (2013) 5570-5577.

[175] Z. Liu, Y. Chen, J. Hu, Y. Zheng, Synthesis and growth mechanism of Cu nanowires in the presence of different linear alkyl diamines, *Science of Advanced Materials* 6 (2014) 327-335.

[176] Y. Fan, Q. Zhang, Q. Xiao, X. Wang, K. Huang, High performance lithium ion battery anodes based on carbon nanotube–silicon core–shell nanowires with controlled morphology, *Carbon* 59 (2013) 264-269.

[177] P. Shewmon, Diffusion in solids, second ed., *The Minerals, Metals & Materials Society*, United States of America, 1989.

[178] H. S. Carslaw, J. C. Jaeger, Conduction of heat in solids, second ed., *Oxford University Press*, New York, 1959.

[179] O. D. Kellogg, Foundations of potential theory, first ed., *Springer-Verlag*, New York, 1967.

[180] M. A. Meyers, K. K. Chawla, Mechanical behavior of materials, second ed., *Cambridge University Press*, New York, 2009.

[181] T. L. Anderson, Fracture mechanics: fundamentals and applications, third ed., *CRC Press*, Boca Raton, 2005.

[182] G. R. Irwin, Plastic zone near a crack and fracture toughness, *Sagamore Research Conference Proceedings* 4 (1961) 63-78.

[183] F. M. Burdekin, D. E. W. Stone, The crack opening displacement approach to fracture mechanics in yielding materials, *Journal of Strain Analysis* 1 (1966) 145-153.

[184] J. R. Rice, A path independent integral and the approximate analysis of strain concentration by notches and cracks, *Journal of Applied Mechanics* 35 (1968) 379-386.

[185] J. R. Rice, G. F. Rosengren, Plane strain deformation near a crack tip in a power-law hardening material, *Journal of the Mechanics and Physics of Solids* 16 (1968) 1-12.

[186] J. W. Hutchinson, Singular behavior at the end of a tensile crack tip in a hardening material, *Journal of the Mechanics and Physics of Solids* 16 (1968) 13-31.

[187] O. C. Zienkiewicz, R. L. Taylor, J. Z. Zhu, The finite element method: its basis and fundamentals, six ed., *Butterworth-Heinemann*, 2005.

[188] L. Lapidus, G. F. Pinder, Numerical solution of partial differential equations in science and engineering, first ed., *Wiley-Interscience*, New York, 1982.

[189] F. J. Rizzo, An integral equation approach to boundary value problems of classical elastostatics, *Quarterly of Applied Mathematics* 25 (1967) 83-95.

[190] C. F. Shih, B. Moran, T. Nakamura, Energy release rate along a three-dimensional crack front in a thermally stressed body, *International Journal of Fracture* 30 (1986) 79-102.

[191] B. Moran, C. F. Shih, A general treatment of crack tip contour integrals, *International Journal of Fracture* 35 (1987) 295-310.

[192] B. Budiansky, J. R. Rice, Conservation laws and energy-release rates, *Journal of Applied Mechanics* 40 (1973) 201-203.

[193] W. C. Carpenter, D. T. Read, R. H. Dodds, Comparison of several path independent integrals including plasticity effects, *International Journal of Fracture* 31 (1986) 303-323.

[194] H. Li, Z. Wang, L. Chen, X. Huang, Research on advanced materials for Li-ion batteries, *Advanced Materials* 21 (2009) 4593-4607.

[195] H. Kim, J. Cho, Hard templating synthesis of mesoporous and nanowire SnO_2 lithium battery anode materials, *Journal of Materials Chemistry* 18 (2008) 771-775.

[196] X. W. Lou, J. S. Chen, P. Chen, L. A. Archer, One-pot synthesis of carbon-coated SnO_2 nanocolloids with improved reversible lithium storage properties, *Chemistry of Materials* 21 (2009) 2868-2874.

[197] N. H. Zhao, L. C. Yang, P. Zhang, G. J. Wang, B. Wang, B. D. Yao, Y. P. Wu, Polycrystalline SnO_2 nanowires coated with amorphous carbon nanotube as anode material for lithium ion batteries, *Materials Letters* 64 (2010) 972-975.

[198] X. Ji, X. Huang, J. Liu, J. Jiang, X. Li, R. Ding, Y. Hu, F. Wu, Q. Li, Carbon-coated SnO_2 nanorod array for lithium-ion battery anode material, *Nanoscale Research Letters* 5 (2010) 649-653.

[199] L. Q. Zhang, X. H. Liu, Y. Liu, S. Huang, T. Zhu, L. Gui, S. X. Mao, Z. Z. Ye, C. M. Wang, J. P. Sullivan, J. Y. Huang, Controlling the lithiation-induced strain and charging rate in nanowire electrodes by coating, *ACS Nano* 5 (2011) 4800-4809.

[200] J. W. Suk, S. Murali, J. An, R. S. Ruoff, Mechanical measurements of ultra-thin amorphous carbon membranes using scanning atomic force microscopy, *Carbon* 50 (2012) 2220-2225.

[201] I. N. Remediakis, M. G. Fyta, C. Mathioudakis, G. Kopidakis, P. C. Kelires, Structure, elastic properties and strength of amorphous and nanocomposite carbon, *Diamond and Related Materials* 16 (2007) 1835-1840.

[202] W.-J. Zhang, A review of the electrochemical performance of alloy anodes for lithium-ion batteries, *Journal of Power Sources* 196 (2011) 13-24.

[203] E. Jacques, M. H. Kjell, D. Zenkert, G. Lindbergh, M. Behm, M. Willgert, Impact of electrochemical cycling on the tensile properties of carbon fibres for structural lithium-ion composite batteries, *Composites Science and Technology* 72 (2012) 792-798.

[204] E. Jacques, M. H. Kjell, D. Zenkert, G. Lindbergh, The effect of lithium-intercalation on the mechanical properties of carbon fibres, *Carbon* 68 (2014) 725-733.

[205] P. Goel, N. Choudhury, S. L. Chaplot, Superionic behavior of lithium oxide Li_2O: A lattice dynamics and molecular dynamics study, *Physical Review B* 70 (2004) 174307.

[206] M. G. Fyta, I. N. Remediakis, P. C. Kelires, D. A. Papaconstantopoulos, Insights into the fracture mechanisms and strength of amorphous and nanocomposite carbon, *Physical Review Letters* 96 (2006) 185503.

[207] W. A. Brantley, Calculated elastic constants for stress problems associated with semiconductor devices, *Journal of Applied Physics* 44 (1973) 534-535.

[208] K. E. Petersen, Silicon as a mechanical material, *Proceedings of the IEEE* 70 (1982) 420-457.

[209] S. K. Soni, B. W. Sheldon, X. Xiao, M. W. Verbrugge, D. Ahn, H. Haftbaradaran, H. Gao, Stress mitigation during the lithiation of patterned amorphous Si islands, *Journal of The Electrochemical Society* 159 (2012) A38-A43.

[210] S. Cho, I. Chasiotis, T. A. Friedmann, J. P. Sullivan, Young's modulus, Poisson's ratio and failure properties of tetrahedral amorphous diamond-like carbon for MEMS devices, *Journal of Micromechanics and Microengineering* 15 (2005) 728-735.

[211] K. Zhao, M. Pharr, Q. Wan, W. L. Wang, E. Kaxiras, J. J. Vlassak, Z. Suo, Concurrent reaction and plasticity during initial lithiation of crystalline silicon in lithium-ion batteries, *Journal of The Electrochemical Society* 159 (2012) A238-A243.

[212] N. K. Simha, F. D. Fischer, O. Kolednik, C. R. Chen, Inhomogeneity effects on the crack driving force in elastic and elastic-plastic materials, *Journal of the Mechanics and Physics of Solids* 51 (2003) 209-240.

[213] Z.-L. Xu, K. Cao, S. Abouali, M. A. Garakani, J. Huang, J.-Q. Huang, E. K. Heidari, H. Wang, J.-K. Kim, Study of lithiation mechanisms of high performance carbon-coated Si anodes by *in-situ* microscopy, *Energy Storage Materials* 3 (2016) 45-54.

[214] W. Stöber, A. Fink, E. Bohn, Controlled growth of monodisperse silica spheres in the micron size range, *Journal of Colloid and Interface Science* 26 (1968) 62-69.

[215] X. Fang, S. Liu, J. Zang, C. Xu, M.-S. Zheng, Q.-F. Dong, D. Sun, N. Zheng, Precisely controlled resorcinol-formaldehyde resin coating for fabricating core-shell, hollow, and yolk-shell carbon nanostructures, *Nanoscale* 5 (2013) 6908-6916.

[216] Y. Huang, R. J. Young, Effect of fibre microstructure upon the modulus of PAN- and pitch-based carbon fibres, *Carbon* 33 (1995) 97-107.

[217] M. Arakawa, S.-i. Tobishima, Y. Nemoto, M. Ichimura, J.-i. Yamaki, Lithium electrode cycleability and morphology dependence on current density, *Journal of Power Sources* 43 (1993) 27-35.

[218] Z.-i. Takehara, Z. Ogumi, Y. Uchimoto, K. Yasuda, H. Yoshida, Modification of lithium/electrolyte interface by plasma polymerization of 1,1-difluoroethene, *Journal of Power Sources* 44 (1993) 377-383.

[219] F. Orsini, A. D. Pasquier, B. Beaudoin, J. M. Tarascon, M. Trentin, N. Langenhuizen, E. D. Beer, P. Notten, In situ scanning electron microscopy (SEM) observation of interfaces within plastic lithium batteries, *Journal of Power Sources* 76 (1998) 19-29.

[220] C. Brissot, M. Rosso, J. N. Chazalviel, S. Lascaud, Dendritic growth mechanisms in lithium/polymer cells, *Journal of Power Sources* 81–82 (1999) 925-929.

[221] M. Dollé, L. Sannier, B. Beaudoin, M. Trentin, J.-M. Tarascon, Live scanning electron microscope observations of dendritic growth in lithium/polymer cells, *Electrochemical and Solid-State Letters* 5 (2002) A286-A289.

[222] L. Gireaud, S. Grugeon, S. Laruelle, B. Yrieix, J. M. Tarascon, Lithium metal stripping/plating mechanisms studies: A metallurgical approach, *Electrochemistry Communications* 8 (2006) 1639-1649.

[223] R. Bhattacharyya, B. Key, H. Chen, A. S. Best, A. F. Hollenkamp, C. P. Grey, In situ NMR observation of the formation of metallic lithium microstructures in lithium batteries, *Nature Materials* 9 (2010) 504-510.

[224] J. N. Chazalviel, Electrochemical aspects of the generation of ramified metallic electrodeposits, *Physical Review A* 42 (1990) 7355-7367.

[225] J.-i. Yamaki, S.-i. Tobishima, K. Hayashi, S. Keiichi, Y. Nemoto, M. Arakawa, A consideration of the morphology of electrochemically deposited lithium in an organic electrolyte, *Journal of Power Sources* 74 (1998) 219-227.

[226] C. Monroe, J. Newman, Dendrite growth in lithium/polymer systems: a propagation model for liquid electrolytes under galvanostatic conditions, *Journal of The Electrochemical Society* 150 (2003) A1377-A1384.